Alma Mater Studiorum — Università di Bologna

SCUOLA DI SCIENZE
Corso di Laurea Magistrale in Astrofisica e Cosmologia
Dipartimento di Fisica e Astronomia

Interstellar Ammonia Emission: Unveiling the Dynamics of a Star-Forming Core

Tesi di Laurea Magistrale

Candidata:
Elena Redaelli

Relatore:
Chiar.mo Prof.
Andrea Cimatti

Co-relatori:
Prof.ssa Paola Caselli
Dott. Felipe de Oliveira Alves

Sessione II - II seduta
Anno Accademico 2015-2016

To my *annus mirabilis*
and to all those took part in it

Sommario

Nonostante il gran numero di campagne osservative e lo sviluppo di modelli teorici, il processo di formazione stellare presenta tutt'oggi diversi punti non ancora chiariti, che riguardano soprattutto le prime fasi di collasso delle strutture. Questo lavoro di Tesi si occupa dello studio della regione di recente formazione stellare nota come Barnard 59. Appartenente alla ben più estesa nebulosa Pipa, una nube molecolare nelle vicinanze del sistema solare, questo *dense core* è l'unico dove si siano individuati diversi oggetti stellari giovani (YSOs) che formano un vero e proprio protocluster. Relativamente a tale sorgente, uno degli importanti interrogativi a cui dare risposta è perché nonostante la grande riserva di gas e l'abbondante numero di dense cores presenti nella Pipa solo Barnard 59 sia stato interessato dalla nascita di nuovi oggetti stellari. Un'altra interessante area di ricerca riguarda invece le conseguenze dell'attività *star forming*, allo scopo di comprendere quale sia l'impatto del *feedback* stellare del protocluster sulla nube da cui esso si è formato.

Il presente lavoro si basa principalmente sullo studio dell'emissione molecolare di ammoniaca: i dati sono stati raccolti dal radiotelescopio di Green Bank GBT e sono costituiti da due mappe delle prime due transizioni di inversione di NH_3 . L'analisi di queste ultime consente di determinare numerose proprietà della sorgente emittente, quali la temperatura, la densità molecolare di colonna e la struttura cinematica. L'approccio matematico consiste nell'eseguire una regressione non lineare degli spettri a disposizione volto ad individuare i valori di best-fit per i parametri liberi.

Accanto a questi dati, con l'obiettivo di costruire una visione quanto più completa di Barnard 59, sono stati utilizzati i dati di archivio del telescopio spaziale Herschel per caratterizzare l'emissione della polvere fredda presente nel gas molecolare. L'analisi di quest'ultima consente infatti di determinare in maniera indipendente la temperatura dei grani di polvere, assunti in equilibrio termico col mezzo interstellare, e la densità di colonna di idrogeno molecolare, la più abbondante molecola del cosmo.

I risultati ottenuti elaborando i dati spettroscopici e fotometrici appena descritti mostrano come Barnard 59 presenti un core molto denso e freddo, coerente dal punto di vista cinematico e contraddistinto da valori nella dispersione di velocità inferiori alla velocità sonica del mezzo interstellare. In prossimità di alcuni YSOs, però, ed in particolare del più giovane tra di essi (denominato B11), le temperature sono più elevate e la dispersione di velocità aumenta. L'analisi delle mappe di queste due variabili ha consentito di investigare gli effetti di feedback dovuti all'attività di formazione stellare. Da esse è stato possibile determinare la

natura subsonica oppure supersonica dei moti nel gas costituente la sorgente. I risultati ottenuti indicano che la parte più densa e fredda di Barnard 59 è caratterizzata da bassi livelli di turbolenza e da moti esclusivamente subsonici, in accordo con l'opinione generale secondo cui i dense cores si formano per dissipazione della turbolenza supersonica che contraddistingue invece le nubi molecolari. Attorno a B11, invece, l'entità della turbolenza aumenta, come probabile conseguenza degli *outflows* di cui tale oggetto è sorgente.

Barnard 59 appare interessato, in conclusione, da attività di formazione stellare che iniettando turbolenza ed energia disturba il gas nel mezzo interstellare. D'altra parte, lo studio dello stato dinamico della sorgente rivela che il dense core è comunque gravitazionalmente legato: gli effetti di feedback sono più che altro locali, e non ne alterano lo stato globale.

Lo studio condotto, grazie ai dati inediti a disposizione, ha consentito di caratterizzare in maniera più approfondita che in precedenza lo stato chimico-fisico della sorgente. Numerosi quesiti rimangono però ancora aperti, in particolare riguardo al comportamento delle variabili analizzate su più larga scala ed al ruolo del campo magnetico in relazione al passato collasso del core ed alla sua futura evoluzione. Nuove e più profonde mappe di ammoniaca ed i dati polarimetrici in banda infrarossa attesi dall'osservatorio stratosferico SOFIA consentiranno di far chiarezza anche su questi punti, nell'ottica di una compressione sempre più completa di uno dei fenomeni più studiati ed ancora misteriosi dell'astrofisica: la formazione stellare.

Contents

List of Figures

List of Tables

Introduction

Molecular clouds and star formation

Star formation occurs by gravitational contraction and collapse of gas and dust that constitute the interstellar medium (ISM). The ISM, which in a spiral galaxy like the Milky Way makes the $0.5-1\%$ of the total mass, exists in different phases. A few examples are the *hot ionized medium* ($n \approx 10^{-3}\,\mathrm{cm}^{-3}$, $T \approx 10^5\,K$) and the *cold neutral medium* ($n \approx 1.0\,\mathrm{cm}^{-3}$, $T \approx 80\,K$), which consists mainly of neutral hydrogen HI. Star "nurseries" are represented by the coldest and densest form of ISM: the *giant molecular clouds*, made of molecular gas such as carbon monoxide (CO) and H_2, like the Orion complex shown in Figure 1.

Figure 1: The Orion Nebula, a part of the Orion giant cloud, in a composite image taken from the Very Large Telescope with infrared filters J (blue), H (green) and K_S (red). [Credit: ESO/H. Drass et al.]

This phase is characterized by density higher than $100\,\mathrm{cm}^{-3}$ and temperature of about $10-15\,K$. While other gas phases, such as the warm and hot ionized medium and the neutral one, are in pressure equilibrium with each other, molecular clouds are not. The dominant force that regulates these structures is self-gravity. They usually have irregular shapes and sizes of tens of parsecs, with a total mass of $\approx 10^5\,M_\odot$. Their gaseous content is mainly found in molecular form. The most abundant component is H_2, which is difficult to observe since it requires great energy (and therefore temperature) to be excited due to the lack of a permanent electric dipole. Molecular gas is then usually traced with the second most abundant molecule, CO.

An alternative method to study the cold interstellar medium is observing another of its components: dust, which accounts for $\approx 1\%$ of the total gas mass. Dust grains consist of a solid silicate core and usually icy mantles. Interstellar grains play an important role in many processes in the ISM. Their surface is capable of accreting atoms and molecules from the gas phase in a process known as *adsorption*. Chemical reactions can occur on grain surface, producing new compounds that later can be released again in the gas (*desorption*). This is thought to be the preferential mechanism for H_2 formation. The depletion of some molecular species due to *freeze-out* onto the grain surface can mistakenly lead to the conclusion that they are not present in the medium.

Interstellar dust is also involved in radiative processes. It absorbs and scatters the radiation coming from background sources, causing the *extinction* of their emission and at the same time its *reddening*. These processes are quantitatively described by the *total-to-selective extinction* R_V, which is the ratio between extinction in visual magnitudes A_V and the color excess $E(B-V)$. This ratio depends on dust grains size: the bigger the grains, the larger the ratio. The expected average value for the Milky Way is $R_V = 3.1$, while in star forming regions higher values are expected. Functions describing how the extinction varies at different wavelengths are called *extinction curves*: some examples are plotted in Figure 2. On the other hand, dust grains reprocess the absorbed radiation to longer wavelengths, giving rise to an emission typically in the far infrared band.

Star formation in giant molecular clouds is preceded by the formation of substructures called *dense cores*, which reach higher volume density ($n \approx 10^{4-5}\,\mathrm{cm}^{-3}$) and lower temperature ($T \lesssim 10\,K$). Dense cores have linear sizes of about $0.1\,\mathrm{pc}$ and contain $\approx 1-10\,M_\odot$ of gas. One of their main features is that they are very quiescent: thermal linewidths are close to the medium sound speed, meaning that turbulent motions are heavily dissipated into the core. Dense cores are gravitationally dominated structures. If other forces, such as magnetic pressure, do not halt the contraction, the subsequent collapse causes an enhancement of temperature and density in the very central part, where a protostar starts to form. The Jeans

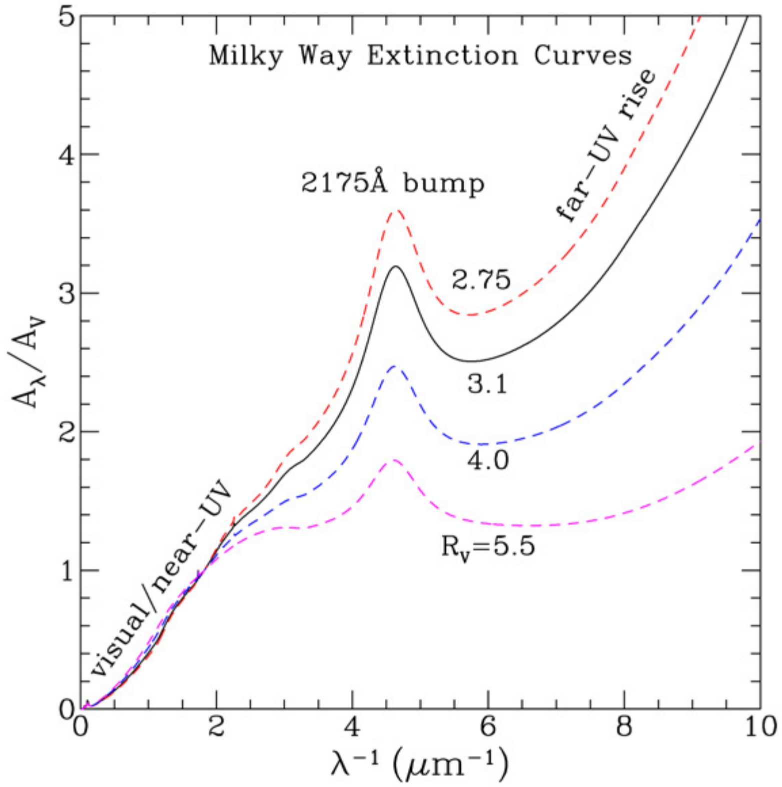

Figure 2: Dust extinction curves in the Milky Way for different values of the parameter R_V. The value $R_V = 3.1$ is the expected average for the galaxy. It is clear that extinction has a differential effect, affecting more heavily short wavelengths. [Ref: Li (2008)].

theory describes the gravitational collapse in a simple but effective way. According to it, an isothermal sphere at the temperature T and with a volume density n_{H_2} is stable if its size does not exceed the Jeans length, defined as:

$$\lambda_J = 0.19 \left(\frac{T}{10\,K}\right)^{\frac{1}{2}} \left(\frac{n_{\mathrm{H}_2}}{10^4\,\mathrm{cm}^{-3}}\right)^{-\frac{1}{2}}\ \mathrm{pc} \tag{1}$$

If the structure radius $R > \lambda_J$, the gravitational pressure overtakes the internal thermal pressure and the body starts to collapse. The Jeans length corresponds to a critical mass value, above which the structure is gravitationally unstable. This critical mass is known as *Jeans mass* and defined by:

$$M_J \approx \rho_0 \lambda_J^3 = 1.0 \left(\frac{T}{10\,K}\right)^{\frac{3}{2}} \left(\frac{n_{\mathrm{H}_2}}{10^4\,\mathrm{cm}^{-3}}\right)^{-\frac{1}{2}}\ M_\odot \tag{2}$$

A brief description of the star formation process will be given in Ch. 5.

Figure 3 shows two images of the dense core L1014 in the direction of the Cygnus. The left one is taken from the Digitized Sky Survey (DSS) and shows the core in absorption: its dense content of gas and dust extinguishes background radiation. The right panel, instead, is a composite infrared image from the Spitzer telescope and reveals the presence of an embedded object, probably a protostar (Young et al., 2004).[1]

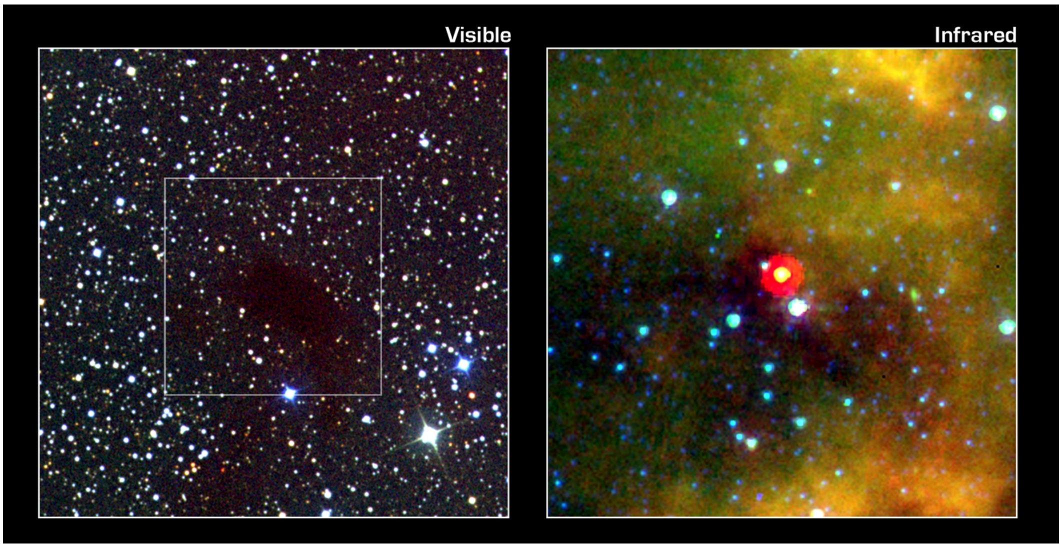

Figure 3: The dense core L1014 seen in visible light, in the left panel, and at infrared wavelengths 3.6 μm (blue), 8.0 μm (green) and 24.0 μm (red) with the Spitzer IRAC camera, in the right panel. [Credit: NASA/JPL-Caltech/N. Evans (Univ. of Texas at Austin)/DSS].

Molecular spectroscopy

All the information that we receive from space comes in the form of electromagnetic radiation. Therefore, our capability to discover and understand the universe is based on how much information we are able to extract from emitted light, not just visible wavelengths but the entire spectrum, from radio frequencies to gamma rays.

Radiative emission is divided in continuum and line emission. The latter is present every time the atomic or molecular components of the analysed source are excited to higher levels of energy and emit radiation according to their energetic

---

[1] Most of this section is based on Stahler & Palla (2005).

structure. Different environmental conditions stimulate and induce distinct radiative processes. Since we are interested in colder phases of the interstellar medium, such as dark cores embedded in molecular clouds, we will focus on molecular line emission. Molecules in space are present in many different environments, from comets to cool envelopes of giant stars, from planetary atmospheres to star forming regions. At the moment, almost 200 of different species have been detected in the space[2].

Molecular emission are produced by different kind of transitions, the main ones being electronic, vibrational and rotational. Electronic excitation requires energies of about $1\,eV$ and the resulting lines fall in the UV-optical range. Rotational transitions, instead, need lower energy and excitation temperature to occur: $E \approx 0.1\,eV$. Their spectra is characteristic of microwave wavelengths. Finally, vibrational excitations involve $E \approx 10^{-3}\,eV$ and are therefore detectable in the far infrared range. Figure 4 shows an example of the molecular energetic structure, indicating the transitions just introduced. The typical temperature of dense cores,

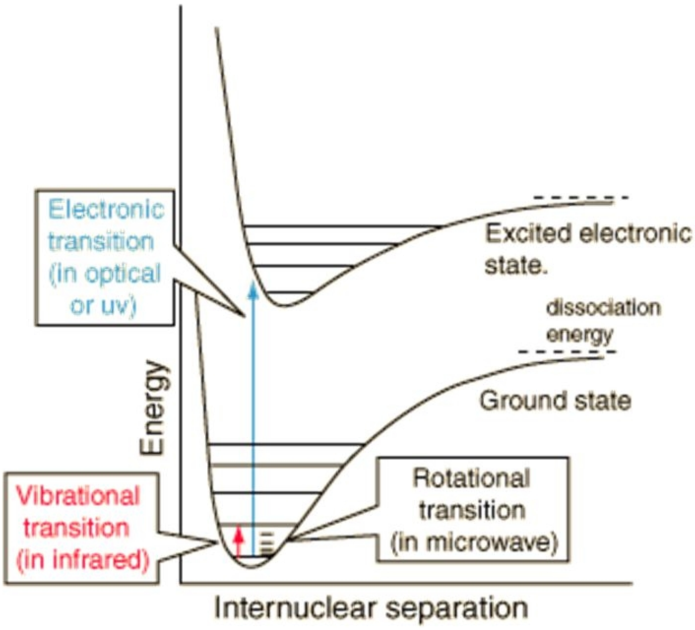

Figure 4: The typical energetic structure of a diatomic molecule, highlighting the different kind of transitions and their wavelength range [Credit.: `http://hyperphysics.phy-astr.gsu.edu/hbase/molecule/molec.html`].

$T \approx 15\,K$, corresponds to an energy $E \approx 10^{-3}\,eV$. Molecules existent in these cores emit mainly due to rotational and vibrational transitions.

---

[2] The updated list can be consulted at `http://www.astro.uni-koeln.de/cdms/molecules`.

In the last decades, molecular spectroscopy in the microwave-radio wavelength range, from approximately 1 GHz to 1 THz, has proved to be an important diagnostic tool of the ISM and, in particular, of star forming regions. The immediate information one can obtain is the composition of the source, which in turn unveils other important details, such as the evolutionary stage of a core. For example, C-bearing molecules are thought to trace early phases of the core evolution and they are soon to be depleted due to the freeze-out onto dust grains, as previously described. On the other hand, deuterated species like N_2D^+ requires longer time to be formed and are usually called late-time molecules (Taylor et al., 1998).

The analysis of rotational spectra can provide also information on the molecular column density. There are a number of approaches that one can follow (Mangum & Shirley, 2015): one of the most commonly used, which will be applied also in the present work, consists of analysing the hyperfine structure in the spectrum of molecules such as NH_3 or N_2H^+.

Since the temperature and the density of the surrounding medium heavily affect the emission, spectroscopic analysis can give information on these quantities as well, by studying the molecular excitation conditions. In addition, multi-line observations of the same molecule allow to derive the number density of the specie.

Finally, molecular spectroscopy is also used to investigate the gas kinematics. The Doppler shift from the theoretical rest frequency of the transition is proportional to the source relative velocity, which is usually expressed in terms of the *local standard of rest*, the reference frame that follows the galactic motions around the Solar System. A map of this velocity across the cloud can reveal internal motions and the overall dynamics. The linewidth shows the medium velocity dispersion that comprises both thermal motions, due to gas thermal agitation, and non-thermal ones, caused by turbulence and protostellar outflows for example.

The NH_3 molecule

The ammonia molecule is the first polyatomic molecule detected in interstellar space. Its discovery, made by Cheung at the Hat Creek Radio Observatory[3], dates back to 1968 and, since then, it has represented a unique diagnostic tool. Due to its large number of transitions and to relatively low critical density, ammonia can be detected in a wide range of environment conditions and allow to determine many physical properties from the emitting region.

Due to the aims of this work, we are mainly interested in the rotational spectrum. NH_3 is an oblate symmetric top molecule, as one can see in Figure 5, i.e. two out of the three principal inertial axes are equal and the moments of inertia

---

[3] A brief description of this discovery can be found in Townes (2006).

are related according to $I_A = I_B < I_C$. Under the rigid-rotator assumption, its rotational energetic levels are determined by the two quantum numbers J, the angular momentum in h unit, and K, its projection along the z-axis, according to:

$$E_{rot} = h\left[B\,J(J+1) + (C-B)K^2\right], \tag{3}$$

where B and C are the rotational constant associated with the two independent principal axes:

$$B = \frac{h}{8\pi c I_B} = 298117\,\mathrm{MHz}, \tag{4}$$

$$C = \frac{h}{8\pi c I_C} = 186726\,\mathrm{MHz}. \tag{5}$$

(Values are taken from Pickett et al. 1998). Due to its structure, in absence of vibrational or collisional excitation, the electric dipole moment lies along the molecular axis of symmetry. Therefore transitions between the different (J-K) levels must fulfil the following selection rules: $\Delta J = 0, \pm 1$ and $\Delta K = 0$. These conditions state that the K-ladders are independent. Actually, weak interactions between rotational and vibrational motions give rise to extremely slow $\Delta K = \pm 3$ transitions ($\tau \approx 10^9\,s$). States with $J = K$ are called metastable, while those with $J > K$ decay rapidly ($10 - 100\,s$) and are called non-metastable.

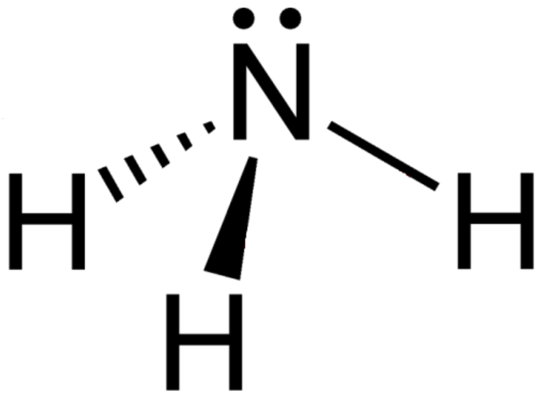

Figure 5: The ammonia trigonal pyramid structure. The dashed bond points above the plane, while the bold one is a below-the-plane one.

Since the nitrogen atom is capable of quantum tunnelling through the hydrogen energetic barrier, each metastable level (except for $K = 0$) is split in a so-called inversion doublet. Inversion transitions, which are allowed since for them $\Delta J = 0$ and $\Delta K = 0$, are characterized by $\nu \approx 23\,GHz$. Now on we will refer to them with the notation (J, K). The critical density n_{cr} for this kind of transitions is $\approx 10^{3-4}\,\mathrm{cm}^{-3}$. Since n_{cr} represents the minimum environment density above which a particular line can be collisionally excited, one can understand that these transitions are suitable for the investigation of cold cores.

Each inversion line shows a further splitting due to hyperfine interactions, which are determined mainly by:

- Interactions between the electric quadrupole moment of N nucleus and the electric field of electrons; this splits each inversion line into a main line, which contains approximately half of the total intensity, and two pairs of fainter satellite lines with a separation of $\approx 1\,\text{MHz}$;

- Magnetic interactions between the total angular momentum of the molecule and the nitrogen and hydrogen spins, which produce a splitting of $\approx 40\,\text{kHz}$;

- N-H and H-H spins coupling that as well introduce new levels separated by $\approx 40\,\text{kHz}$.

As a result, for example, the (1,1) state is split in 18 levels, as visible in Figure 6.

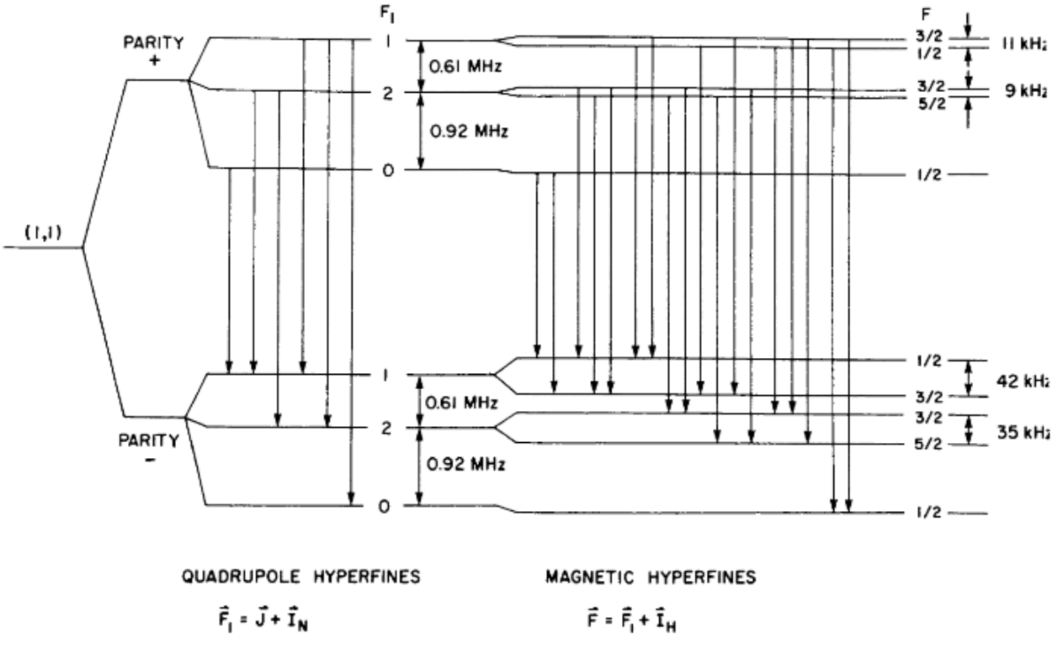

Figure 6: Hyperfine structure for the (1,1) inversion transition. I_N and I_H are respectively the nitrogen and the total hydrogen spins [Ref: Ho & Townes (1983)].

Ammonia formation can occur both through gas phase reactions and grain chemistry (Hasegawa et al. 1992 and Scott et al. 1997). The first route consists of a sequence of ion-molecular reactions:

$$\begin{aligned}
\mathrm{N^+} + \mathrm{H_2} &\rightarrow \mathrm{NH^+} + \mathrm{H},\\
\mathrm{NH^+} + \mathrm{H_2} &\rightarrow \mathrm{NH_2^+} + \mathrm{H},\\
\mathrm{NH_2^+} + \mathrm{H_2} &\rightarrow \mathrm{NH_3^+} + \mathrm{H},\\
\mathrm{NH_3^+} + \mathrm{H_2} &\rightarrow \mathrm{NH_4^+} + \mathrm{H},\\
\mathrm{NH_4^+} + \mathrm{e^-} &\rightarrow \mathrm{NH_3} + \mathrm{H}.
\end{aligned}$$

On the other hand, the formation of NH_3 on grain surface occurs via successive hydrogenation of N atoms, following:

$$\begin{aligned}
\mathrm{N} + \mathrm{H} &\rightarrow \mathrm{NH},\\
\mathrm{NH} + \mathrm{H} &\rightarrow \mathrm{NH_2},\\
\mathrm{NH_2} + \mathrm{H} &\rightarrow \mathrm{NH_3}.
\end{aligned}$$

According to the orientation of hydrogen I_H spins, we distinguish two ammonia species: ortho-NH_3 , for which $I_H^{tot} = \frac{3}{2}$ and $K = 3n$, being n an integer, and para-NH_3 , which has $I_H^{tot} = \frac{1}{2}$ and $K \neq 3n$. The ortho-to-para ratio (OPR) is an indicator of the temperature at the moment of the NH_3 formation. The lowest energy states of para and ortho species are separated by $\Delta E_{ortho}^{para} \approx 23\,K$. If ammonia is formed in gas phase, since the involved chemical reactions release more energy than ΔE_{ortho}^{para}, we expect the OPR to be close to the unit. On the other hand, if the molecules are formed on dust grains, where $T \lesssim 30\,K$, and then desorbed in the gas phase we predict OPR > 1, since the desorption energy is higher for para- NH_3 than for ortho-NH_3 (Faure et al., 2013). It is important to notice that neither collisional interaction nor roto-vibrational ones can alter the ortho-to-para (OPR) ratio, since for them $\Delta K = 0, \pm 3$.

The importance of the NH_3 molecule in probing the ISM lies in the diagnostic power of its spectroscopic analysis: from the detection of at least two states (usually (1,1) and (2,2)) one can infer not only the kinematics of the source, deriving local standard of rest velocity V_{lsr} and velocity dispersion σ_V maps, but also other physical properties, such as the NH_3 excitation temperature T_{ex} , molecular column density N(NH_3) and the gas kinetic temperature T_K . This justifies the name usually given to this molecule: the *gas thermometer* (Walmsley & Ungerechts, 1983). We will now summarize our approach of this analysis, including the main equations and results.

First of all, we must specify that there are three different kind of temperatures involved:

- Excitation temperature T_{ex} , which regulates the population of the upper (u) with respect to the lower (l) level in the same (J, J) state according to the

Boltzmann law:

$$\frac{n_u}{n_l} = \frac{g_u}{g_l} e^{-\frac{\Delta E_{ul}}{k_b T_{ex}}} \ , \tag{6}$$

where ΔE_{ul} is the energy difference between the two states and g are the statistical weights;

- Rotational temperature T_R, according to which two different inversion states (J, J) and (J', J') are populated, again through the Boltzmann equation:

  $$\frac{n_{J'J'}}{n_{JJ}} = \frac{g_{J'J'}}{g_{JJ}} e^{-\frac{\Delta E_{JJ'}}{k_b T_R}} \ , \tag{7}$$

  where $\Delta E_{JJ'}$ is the energy gap between them. Notice that the term "rotational" is erroneous in this context, because we are not dealing with purely rotational transitions;

- Kinetic temperature T_K : this is the "true" gas temperature, which describes the thermal agitation of the medium.

The main assumption (Ho & Townes 1983, Ungerechts et al. 1986, Friesen et al. 2009) is the Local Thermal Equilibrium (LTE), according to which T_{ex} is the same for all of the states and just one temperature T_K is needed to describe the entire medium.

Suppose now that we observe the ammonia emission with a radiotelescope: the main-beam brightness temperature T_{MB}[4] for the state (J, K) can be written as:

$$T_{MB}^{JK} = A_{JK} \left(1 - e^{-\tau(v)}\right) \ , \tag{8}$$

where the amplitude $A_{JK} = \eta_f \left(J_\nu(T_{ex}) - J_\nu(T_b)\right)$. T_b is the background temperature (equal to $2.73\,K$ if no other background source is present), function $J_\nu(T)$ is given by $(h\nu/k)\left(\exp(h\nu/kT) - 1\right)^{-1}$ and η_f the filling factor, which is the ratio between the source and the beam angular sizes ($\eta_f = \Omega_S/\Omega_{beam}$). The optical depth τ at the velocity v can be expressed as:

$$\tau_{JK}(v) = \tau_{JK}^{tot} f_{JK} = \tau_{JK}^{tot} \sum_{i=1}^{N} s_i \exp\left(-4\ln(2)\left(\frac{v - V_{lsr} - v_i}{\Delta v_{int}}\right)^2\right) \ . \tag{9}$$

The sum is computed over the N hyperfine levels, each with velocity v_i and relative intensity s_i. Δv_{int} is the line intrinsic width and V_{lsr} is the source velocity in the local standard of rest.

---

[4] A description of telescopes and observations in the radio wavelengths range will be given in Ch. 2.

The general approach is to obtain V_{lsr} , Δv_{int}, A_{JK}, and τ_{JK}^{tot} from spectral fit and then to infer N(NH$_3$) , T_K and T_{ex} . With this aim, several relations are used:

$$\tau_{JK}^{tot} = \frac{8\pi^3 2\sqrt{\ln 2}}{3\sqrt{\pi}h}|\mu|^2 \frac{K^2}{J(J+1)} \frac{N_{JK}X_{JK}}{\Delta v_{int}} \ , \tag{10}$$

$$X_{JK} = \frac{1-\exp\left(-h\nu/kT_{ex}\right)}{1+\exp\left(-h\nu/kT_{ex}\right)} = \frac{\eta_f h\nu}{2k} \frac{1}{\left(A_{JK} + \eta_f \left(J_\nu(T_b) + \frac{h\nu}{2k}\right)\right)} \ . \tag{11}$$

In these equations, μ are the elements of the dipole matrix, N_{JK} the (J,K) state column density and X_{JK} is a function of excitation temperature only. In LTE, all the different energy levels are populated according to Boltzmann statistic, as seen in Eq. (7). In particular, the states (1,1) and (2,2) are separated by ΔE_{12}, corresponding to a temperature $T_{12} \approx 41.5K$. Assuming homogeneity along the line of sight, it holds:

$$\frac{n_{22}}{n_{11}} = \frac{N_{22}}{N_{11}} = \frac{g_{22}}{g_{11}} e^{-\frac{41.5\,K}{T_R}} \ . \tag{12}$$

Inserting Eq. (10) in Eq. (12) and using $g_{11} = 9$, $g_{22} = 20$, one obtains:

$$T_R = -41.5K \left[\ln\left(\frac{9}{20}\frac{\tau_{22}^{tot}}{\tau_{11}^{tot}}\frac{\Delta v_{int}(22)}{\Delta v_{int}(11)}\frac{X_{11}}{X_{22}}\right)\right]^{-1} \ . \tag{13}$$

If the excitation temperature is the same for all states, it holds $X_{11} = X_{22}$. Besides, if the two emissions trace the same volume of gas, $\Delta v_{int}(11) = \Delta v_{int}(22)$. Eq. (13) thus simplifies as:

$$T_R = -41.5K \left[\ln\left(\frac{9}{20}\frac{\tau_{22}^{tot}}{\tau_{11}^{tot}}\right)\right]^{-1} \ . \tag{14}$$

As far as the column density is concerned, one can again use eq. (10) and (11) to obtain:

$$N_{JK} \cdot \eta_f = \kappa(J,K)\, \Delta v_{int}(J,K) \left(A_{JK} + \eta_f \left(J_\nu(T_b) + \frac{h\nu}{2k}\right)\right) \ , \tag{15}$$

where κ is a multiplicative constant which depends on the (J,K) state: for (1,1) its value is $\approx 1.3773\,10^{13}\mathrm{cm}^{-2}$ (Ungerechts et al., 1986). It is important to note that some assumptions has to be made on the beam filling factor, if the source angular size is smaller than the beam. The total column density should be computed summing up column densities for all states. If only N_{11} is known, though, one can use the approximation (Ungerechts et al., 1986):

$$\mathrm{N(NH_3)} \approx N_{11} \left[\frac{1}{3}e^{\frac{23.2K}{T_R}} + 1 + \frac{5}{3}e^{-\frac{41.5K}{T_R}} + \frac{14}{3}e^{-\frac{100K}{T_R}} + ...\right] \ , \tag{16}$$

which again holds under the assumption that ortho- and para-NH_3 states are populated according to thermal equilibrium. More precisely, one should take into account the rotational partition function Z_{tot} obtained summing through all states (see Friesen et al. 2009):

$$Z_{tot} = \sum_J Z_J = \sum_J S(J)\,(2J+1) exp\left[-\frac{h\,(BJ(J+1)+(C-B)J^2)}{k_B T_R}\right]\,. \tag{17}$$

$S(J)$ is a two-value function that equals 2 for ortho-states and 1 for para-ones. The total column density is then derived through:

$$\mathrm{N(NH_3)} = N_{11}\,\frac{Z_{tot}}{Z_{11}}. \tag{18}$$

Since the transitions between inversion doublets are usually much faster than other rotational transitions, one can approximate them as a two-state system. In this way, from the knowledge of the A Einstein coefficient and the collisional coefficient C, the H_2 volume density can be calculated as:

$$n(\mathrm{H_2}) = \frac{A}{C}\frac{J_\nu(T_{ex}) - J_\nu(T_b)}{J_\nu(T_K) - J_\nu(T_{ex})}\left[1 + \frac{J_\nu(T_K)}{h\nu/k_B}\right]\,. \tag{19}$$

The underlying hypothesis here is that the upper state is populated only through collisions with H_2 molecules.

This theory and equations allow us to determine the rotational temperature, while what we are actually interested in is kinetic temperature. A way to determine it, which is implemented in the code that will be described later on, is to consider a three states system composed by (1,1), (2,2) and (2,1) levels. The transition between different K-ladders, as previously said, is allowed only thorough collisions. Once the level (2,1) is populated, it immediately decays radiatively to the (1,1). Thus, solving the detailed balance taking into account spontaneous emission and collisional rates leads to the following equation (Swift et al., 2005):

$$T_R = T_K\left\{1 + \frac{T_K}{T_{12}}\,\ln\left[1 + 0.6\exp\left(-15.7/T_K\right)\right]\right\}^{-1}\,, \tag{20}$$

which gives the kinetic temperature.

Dust emission properties

Dust grains radiate thermal emission as a consequence of the absorption of the background radiation field. The analysis of dust spectral energy distribution can provide important information about the source, such as the dust temperature T_{dust} and the gas column density $\mathrm{N(H_2)}$.

In order to determine how dust grains interact with interstellar radiation, one can consider the transfer equation:

$$\frac{dI_\nu}{ds} = -\rho\kappa_\nu I_\nu + j_\nu \ . \tag{21}$$

This equation states that the specific intensity emitted I_ν along the propagation path s is formed by two terms: the first one is related with the attenuation of the incoming radiation by matter, which depends on the source mass density ρ and the opacity κ_ν. The second part contains the source emissivity j_ν. κ_ν represents the dust absorption cross-section per unit mass of gas. Its units are $\mathrm{cm^2\ g^{-1}}$. We can define the quantity *optical depth* through:

$$\tau_\nu = \int_{los} \kappa_\nu \rho \, ds \ . \tag{22}$$

Given this, integrating Eq. (21) for a body at the temperature T, assuming that the absence of any external source of radiation, one obtains:

$$I_\nu = B_\nu(T)\left(1 - e^{-\tau_\nu}\right) \ , \tag{23}$$

where $B_\nu(T)$ is the Planck function for the perfect black-body emissivity:

$$B_\nu(T) = \frac{2h\nu^3}{c^2}\frac{1}{e^{\frac{h\nu}{kT}} - 1} \ . \tag{24}$$

Eq. (23) describes a kind of emission close to the black-body one, but modified by a factor $(1 - e^{-\tau_\nu})$. It is usually referred to as *gray-body* radiation or *modified black-body*, due to its dependency on the quantity κ_ν that in turn depends on frequency. It is important to notice that T is the temperature of the dust grains, which can differ from the gas one. This is the reason why we distinguish between T_{dust} and T_{gas}.

The definition of gas column density reads:

$$\mathrm{N_{H_2}} = \int_{los} n_{\mathrm{H_2}} \, ds = \int_{los} \frac{\rho}{\mu_{\mathrm{H_2}} m_{\mathrm{H}}} \, ds \ . \tag{25}$$

Here m_{H} is the hydrogen atom mass and $\mu_{\mathrm{H_2}}$ is the mean molecular weight per hydrogen molecule which can be calculated from the cosmic abundance ratios. For typical values of hydrogen mass fraction ($X \approx 0.71$), $\mu_{\mathrm{H_2}} \approx 2.8$[5]. Combining Eq.

---

[5] $\mu_{\mathrm{H_2}}$ is defined through: $\mu_{\mathrm{H_2}}\, m_{\mathrm{H}}\, \mathrm{N(H_2)} = M_{tot}$; since the number of hydrogen molecules $\mathrm{N(H_2)}$ is half that of H-atoms $\mathrm{N(H)}$ and $M(\mathrm{H}) = X\, M_{tot} = 0.71\, M_{tot}$, one can calculate the value for the mean molecular weight.

(22) and (25) one obtains the following equation:

$$\mathrm{N}_{\mathrm{H}_2} = \frac{\tau_\nu}{\mu_{\mathrm{H}_2} m_{\mathrm{H}} \kappa_\nu} \ . \tag{26}$$

Therefore, if the optical depth at a given frequency is known the column density can be inferred. A power-law expression is usually adopted for κ_ν:

$$\kappa_\nu = \kappa_0 \left(\frac{\nu}{\nu_0} \right)^\beta \ . \tag{27}$$

β must be a positive number, since the absorption cross-section increases with frequency: normally it is found $\beta \approx 1 - 2$, depending on dust properties. ν_0 is the reference frequency that corresponds to the wavelength λ_0, at which the dust opacity is κ_0. Gray-body emission thus differs from a pure black-body in the frequency dependency: in the Rayleigh-Jeans approximation, while the planckian function depends on frequency as $B_\nu \propto \nu^3$, for a gray-body $I_\nu \propto \nu^{3+\beta}$. An important and interesting case is when the medium is optically thin ($\tau << 1$), then Eq. (23) simplifies through Taylor series expansion to:

$$I_\nu \approx B_\nu(T)\, \tau_\nu \qquad \rightarrow \qquad \tau_\nu \approx \frac{I_\nu}{B_\nu(T)} \ . \tag{28}$$

In order to have an idea of which spectral ranges are typical of dust thermal emission, one can resort to Wien's displacement law $\lambda_{peak} T = 2.910^{-3}\ \mathrm{m}\, K$ that relates the wavelength of the emission peak to the emitting body temperature, even though this is strictly valid only for a pure black-body. In a molecular cloud, where $T \approx 15\, K$, $\lambda_{peak} \approx 200\, \mu\mathrm{m}$ and the radiation occurs at the far-infrared wavelengths. The analysis of photometric data of dust SED allows to determine temperature maps. From the latter, one can infer an optical depth map using Eq. (28). Eventually, one calculates the gas column density by means of Eq. (26). Given this, dust emission turns out to be a powerful probe of the physical conditions in the ISM, at least in the cold phase where grains are not destroyed and sputtered ($T \lesssim 100\, K$). We will apply this technique in Ch. 4

Chapter 1

Barnard 59

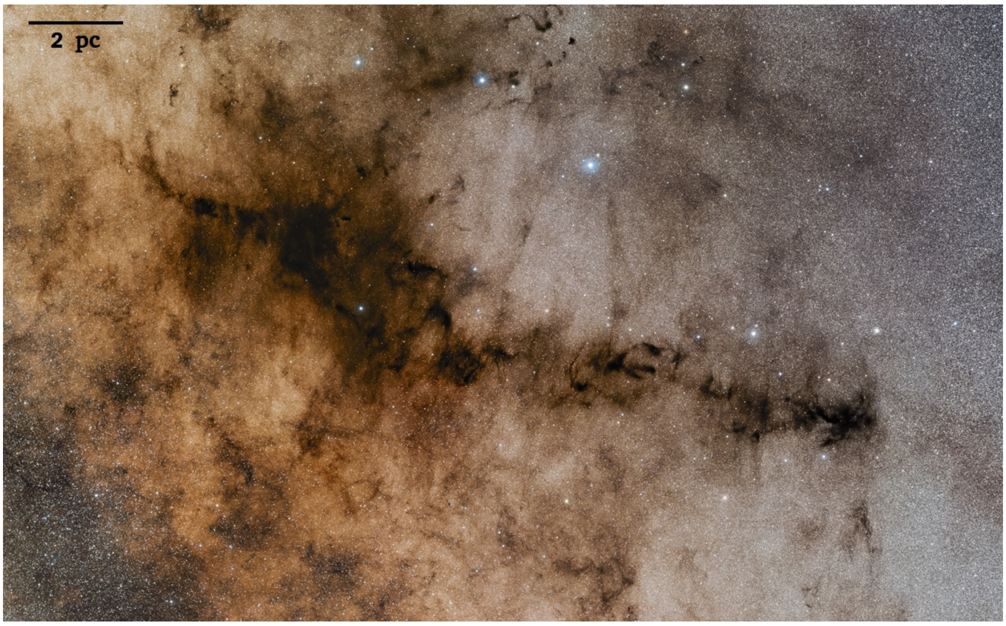

Figure 1.1: The Pipe Nebula as seen in visible light from the Atacama desert with the Very Large Telescope: its dust content extinguishes heavily the light from background stars [Credit: ESO/S. Guisard].

The Pipe Nebula, presented in Figure 1.1, is a nearby, elongated dark cloud located at a distance $d \approx 145\,\mathrm{pc}$ (Alves & Franco, 2007) against the Galactic bulge in projection (galactic coordinates: $l \approx 0^\circ$, $b \approx 5^\circ$). It owes its name due to its peculiar shape, which resembles a pipe. It is usually divided in two substructures: the *stem*, a filamentary, long ($l \approx 10\,\mathrm{pc}$) structure, and the *bowl*, at its east end. While the stem seems to be a coherent structure from the kinematic point of view, with just one velocity component ($V_{lsr} \approx 3.5\,\mathrm{km\,s^{-1}}$), at least a second component at higher velocity ($V_{lsr} \approx 5.0\,\mathrm{km\,s^{-1}}$) is present in the bowl (Muench et al., 2007). From extinction measurements (Lombardi et al., 2006), the entire cloud has a mass content of about $M_{tot} \approx 10^4\,M_\odot$, consistent with mass estimation from molecular line emission (Onishi et al., 1999). Onishi et al. (1999) investigated the region with ^{12}CO, ^{13}CO and C^{18}O, and found that, despite its huge cold gas content, star formation is active only in a very small part of it, the extreme north-west end of the stem, also known as Barnard 59 (B59). The star formation efficiency is extremely low (SFE $\approx$ 0.06% according to Forbrich et al. 2009). As a consequence, this source remained basically unstudied until 2006, when the lack of star formation activity and its proximity made it the perfect target to investigate the first phases of core collapse in great detail.

Using extinction peaks as tracers, many authors investigated the population of dark cores in the cloud. About 159 cold and mainly prestellar cores have been detected (Lada et al., 2008). They appear generally quiescent, with subsonic non thermal motion, and thermally dominated. The lack of relation between their size or mass and internal velocity dispersion suggests that they are not self-gravitating structures, kept in equilibrium by the balance between internal thermal pressure and external one, probably due to the weight of the Pipe itself (Lada et al., 2008). Chemical studies confirm this general picture: the cores are all in a very early phase, even though their chemistry appears rich and differentiated probably due to different evolutionary stages (Frau et al. 2010, Frau et al. 2012a, Frau et al. 2012b). Further studies on the core mass function (CMF) (Alves et al. 2007, Rathborne et al. 2009) led to the important conclusion that CMF resembles in shape the stellar initial mass function (IMF), shifted of a factor $\approx 3-4$. This supports the idea that the IMF is a direct consequence of the CMF, given a star formation efficiency, and moves the problem of understanding initial protostellar phase to the comprehension of cores formation and collapse.

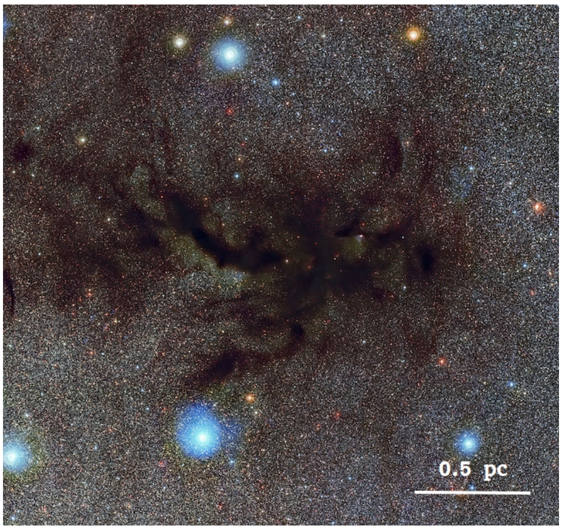

Figure 1.2: Barnard 59 in optical observation [Credit: MPG/ESO 2.2 metre telescope].

Barnard 59 is shown in Figure 1.2. It is an irregularly shaped dark cloud, firstly catalogued by Barnard in 1927 [1]. Its size is about $30' \times 45'$, and it represents the most massive core found in the region ($M \approx 20 - 30\,M_\odot$) and appears gravitationally bound. The presence of ongoing star formation activity, first discovered by Onishi et al. (1999) due to the detection of CO outflows, has been further investigated within the Core to Disks (c2d) Legacy Science program, a survey observed with *Spitzer Space Telescope*. Figure 1.3 shows the Spitzer image of B59 at the wavelength $\lambda = 24\,\mu$m. Brooke et al. (2007) found at least 20 candidate young stellar objects associated to the core, leading to the conclusion that B59 hosts a young, low-mass protocluster, with an estimated median age of $\tau \approx 2.6\,Myr$ (Covey et al., 2010). At least three objects are driving outflows on large scale, which locally affect the gas with higher temperatures and velocity dispersions, but don't seem to be disturbing the core as a whole. Their energy injection, derived from ^{12}CO maps, is enough to sustain the turbulence level of the gas at sub-pc scales, and can probably slow down the collapse of the region (Duarte-Cabral et al., 2012). Concerning this, the core shows no sign of further fragmentation (Román-Zúñiga et al., 2012).

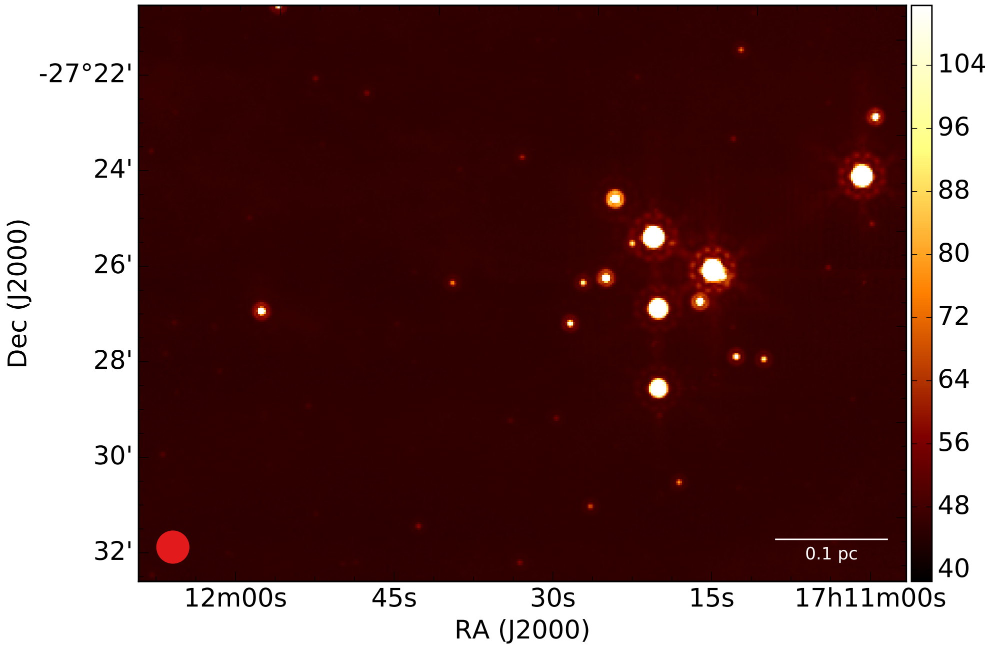

Figure 1.3: Barnard 59 with the Spitzer MIPS camera at $\lambda = 24\,\mu m$; many luminous infrared sources, candidate to be young stars, are visible.

---

[1] The famous *Barnard Catalogue of Dark Markings in the Sky*, composed by astronomer Edward Emerson Barnard, contains 369 dark nebulae.

The variety of studies performed so far indicates that the Pipe Nebula is one of the best place to analyse very early stages in star formation. Its properties naturally lead to a question: why only B59 among hundreds of cores is active? Some authors have suggested that magnetic field is taking a leading role: in fact, the bowl is threaded by the strongest magnetic fields, while Barnard 59 is characterized by the weakest (Alves et al. 2008, Franco et al. 2010). According to these authors, the three regions of the Pipe stand for three different evolutionary stages: the bowl is just at the beginning of a contraction phase, since it is more supported by magnetic field, and B59 on the contrary has already collapsed. The stem is in an intermediate situation between the two. It is not however clear which is the physical origin of this morphology. Peretto et al. (2012) suggests that a large-scale external compression, maybe due to stellar winds coming from the close Sco OB2 association[2], can determine at least the initial formation of filaments. A better understanding of the nature and the physical properties of this source will possibly enlighten the comprehension of what triggers and drives star formation in molecular clouds. Besides, we will also be able to investigate the importance of protostellar feedback and its role in the further evolution of the cloud.

---

[2] The Scorpio-Centaurus OB association, known as Sco OB2, is the closest region of recent massive star formation. It lies at 145 pc from the Sun (de Zeeuw et al., 1999) and at ≈ 30 pc from the Pipe.

Chapter 2

Ammonia observations

In this chapter I will first give a brief theoretical introduction to the main concepts involved in single dish observations, based mainly on Wilson et al. (2009). Then I will describe the facility used to collect ammonia data, the Green Bank Telescope, highlighting the features that make it suitable for this investigation. I will therefore describe how the observations were carried out as far as instruments and calibration technique are concerned. In the last section, an overview of the collected data will be presented.

2.1 Introduction to single dish observation

A radio telescope consists of a main dish that collects the incoming wavefront and drives it to the primary focus, where the detectors can be placed. It is a common choice, however, to use a secondary mirror or subreflector which focuses the signal to the secondary focus. The receivers are usually sensitive to the electric field of the radio waves, and are able to transform it in an electric signal that needs to be converted in scientifically usable data. Most of modern receivers lower the input frequency from sky emission to a lower frequency, called Intermediate Frequency (IF), before further processing: this solution allows in fact great flexibility in the radiation analysis. The processing chain is divided in two parts: the *frontend*, which operates at sky frequency, and the *backend*, working at lower frequencies. Frontends are mainly amplifiers and mixers that actually operates the frequency shift. Backends, instead, are devices able to amplify and analyse signal features such as the level of polarization and the spectral energy distribution of the radiation.

The emission of a radio telescope is described by the *Power Pattern* $P(\theta, \phi)$ function, also known as *beam* or *point spread function*, which depends on the two polar coordinates θ and ϕ. Normally the normalized power pattern is used:

$$P_n(\theta,\phi) = \frac{P(\theta,\phi)}{P_{max}} \; . \tag{2.1}$$

Let P be the total power emitted per solid angle by an isotropic antenna. This is an ideal case: more realistically, the antenna radiates differently in different directions. We can call *directive gain* the factor that relates P to the power pattern:

$$G(\theta,\phi) = \frac{P(\theta,\phi)}{P} = \frac{4\pi P(\theta,\phi)}{\int P(\theta,\phi)\, d\Omega} \; . \tag{2.2}$$

Due to the reciprocity theorem, the parameters of an antenna are the same whether it is used to emit or receive radiation. It is therefore possible to use $P_n(\theta,\phi)$ to fully describe the telescope performance. From this function one can derive many important quantities, such as the antenna *beam solid angle* Ω_A[1]:

$$\Omega_A = \int_{4\pi} P_n \, d\Omega = \int_0^{\pi} \int_0^{2\pi} P_n(\theta,\phi) \sin\theta \, d\theta \, d\phi \; . \tag{2.3}$$

Confronting Eq. (2.2) and (2.3), one can see that the maximum gain, or *directivity* D, is related to Ω_A through:

$$G_{max} = D = \frac{4\pi}{\Omega_A} \; . \tag{2.4}$$

As seen in Figure 2.1, usually the beam is made up of a *main lobe*, which at the operative wavelengths should contain most of the power, and many *side lobes.* It is useful to define the *main beam solid angle* as:

$$\Omega_{MB} = \int_{main\, lobe} P_n \, d\Omega \; . \tag{2.5}$$

In order to assess the quality of a telescope, one important parameter is the *beam efficiency*:

$$\eta_B = \frac{\Omega_{MB}}{\Omega_A} \leq 1 \; . \tag{2.6}$$

This gives an idea on the fraction of power concentrated in the main lobe: the lower η_B, the more power is entering from side lobes, impeding the correct localization of the emitting source. The beam efficiency does not involve the beam angular size, another essential parameter since it describes a telescope angular resolution. Concerning this, the most widely used quantity is the *half power beam*

---

[1] Solid angles are measured in steradians (sr).

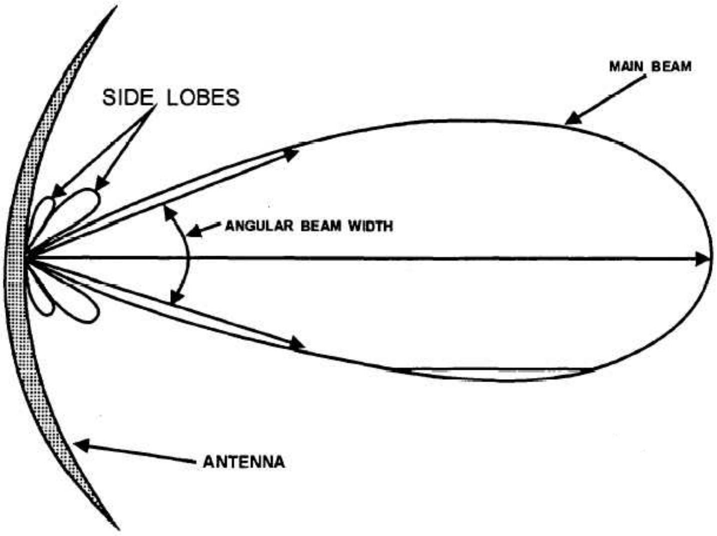

Figure 2.1: A schematic example of an antenna beam, where both main and side lobes are visible [Credit `http://meteorologytraining.tpub.com/14271/css/14271_61.htm`].

width (HPBW), also known as *full width half power* (FWHP), which is the angle between points of the main beam where $P_n = 0.5$. It is useful to define also the *equivalent width of the main beam* as:

$$\mathrm{EWMB} = \sqrt{\frac{12}{\pi}\Omega_{MB}} \; . \tag{2.7}$$

Let a wavefront be intercepted by an antenna, which in turn will register a power density that is only a fraction of the incoming one. This difference is referred to as the *aperture efficiency* η_A, which links the *geometric aperture* (the parabola area) to the *effective* one:

$$A_{eff} = \eta_A A_{geom} < A_{geom} \; . \tag{2.8}$$

Many factors contribute to limit the effective aperture, such as deformations in the mirror or the presence of blocking obstacles. The secondary mirror, for example, often shades the primary one. Effective aperture and directivity are related through:

$$D = \frac{4\pi A_{eff}}{\lambda^2} \; , \tag{2.9}$$

which, using Eq. (2.4), leads to the fundamental relation:

$$A_{eff}\Omega_A = \lambda^2 \; . \tag{2.10}$$

The data coming from a radio telescope are often expressed in units of *antenna temperature*, defined as follows: let $B_\nu(\theta,\phi)$ be the brightness distribution observed in the sky with an antenna characterized by $P_n(\theta,\phi)$. The power detected by the receiver is:

$$P_\nu = \frac{1}{2}A_{eff}\int B_\nu(\theta,\phi)P_n(\theta,\phi)\,d\Omega\ . \tag{2.11}$$

The antenna temperature is then defined by:

$$P_\nu = kT_A\ , \tag{2.12}$$

which is the temperature that a resistor would have to emit the same power P_ν. Due to the relation (2.10), and using the Rayleigh-Jeans approximation $B_\nu = 2kT_b/\lambda^2$, one can link antenna temperature to brightness temperature T_b obtaining:

$$T_A(\theta_0,\phi_0) = \frac{\int_0^\pi\int_0^{2\pi} P_n(\theta-\theta_0,\phi-\phi_0)T_b(\theta,\phi)\sin\theta\,d\theta\,d\phi}{\int P_n(\theta,\phi)\,d\Omega}\ . \tag{2.13}$$

Observations carried out with ground based facilities have always to take into account atmosphere influences on measurements, first of all the attenuation of incoming signal due to atmospheric absorption. T_A must be therefore corrected for total opacity along the line of sight τ_ν:

$$T'_A = T_A e^{\tau_\nu}\ . \tag{2.14}$$

Moreover, we are interested only in the radiation coming from the front of the telescope and not from the 4π solid angle; the relation between the two is described by the *forward efficiency* factor F_{eff}, defined as:

$$F_{eff} = \frac{\int_{2\pi} P_n\,d\Omega}{\int_{4\pi} P_n\,d\Omega}\ . \tag{2.15}$$

This introduces a new temperature scale $T^*_A = F_{eff}T'_A$, which however still concerns the entire beam. On the contrary we would like to restrict its definition to the main lobe only, which is usually well known and in many cases can be approximated with a Gaussian shape. It is therefore natural the introduction of *main beam temperature*, T_{MB}:

$$T_{MB} = \frac{T^*_A}{\eta_B} = \frac{F_{eff}}{\eta_B}T'_A\ . \tag{2.16}$$

The main problem is to know how all these quantities are related to the one of our interest: the source brightness temperature. The answer is relatively easy in some limiting cases, depending on the source size in solid angle Ω_S:

1. Sources smaller than the beam ($\Omega_S << \Omega_{MB}$): one must take into account the beam filling factor η_f. The relation to use is $T_{MB} = \eta_f T_b$;
2. Sources filling exactly the beam ($\Omega_S = \Omega_{MB}$): $T_{MB} = T_b$;
3. Sources larger than the beam ($\Omega_S >> \Omega_{MB}$): $T_A^* \approx T_b$.

Data coming from backends are simple counts that have to be converted to flux scale. This operation is called flux calibration, and at cm-wavelengths it is usually done with noise diodes that can add to the incoming signal a known amount of noise. The calibration procedure consists in making an observation with the diode on and one with the diode off: the difference between the two contains only the noisy signal, for which the absolute value is known. From this, one can infer the absolute scale either in K or in Jy.

The noise level in an observation is described by the *system temperature* T_{sys}, which includes all the expected signal contributions from the sky down to the backends. The associated noise is:

$$\sigma = \kappa \frac{T_{sys}}{\sqrt{N_{pol} \tau \Delta\nu}} \tag{2.17}$$

where κ is a constant depending on observing mode (see next section), N_{pol} is the number of independent polarization channels to be averaged, τ is the effective integration time, $\Delta\nu$ the frequency bandwidth. For spectral line observations, $\Delta\nu$ is the width of a single channel and the noise is usually higher than in the continuum case.

2.2 The Green Bank Telescope

The Robert C. Byrd Green Bank Telescope (GBT), shown in Figure 2.2 is a single dish antenna located at Green Bank, West Virginia (USA) and is part of the National Radio Astronomy Observatory (NRAO). It is the largest fully steerable telescope in the world. Its mounting is alt-azimuthal: the antenna is turned about two axes, the azimuthal one, perpendicular to the ground, and the elevation one, which is horizontal. This configuration allows a sky coverage of about 85%. The dish has a 100 m by 110 m surface, achieving an angular resolution at Gregorian focus of ≈ 12.60 arcmin/ν_{GHz}. Another feature is its unblocked surface: the arm supporting primary feeds and optics is cantilevered from below the main dish, which is therefore an offset paraboloid segment in order to allow a side position for the primary focus. This solution, avoiding blocking or scattering the incoming wavefront, improve the telescope performances because it reduces the sidelobes, spectral standing waves and also artificial radio frequency interference. The NRAO facility at Green Bank is built in a radio quiet zone, which helps reducing artificial radiation towards the telescope. The antenna is composed by 2004 panels moved by over 2200 actuators, which can correct distortions from the ideal shape of the parabola due to gravity changes at different elevation angles.

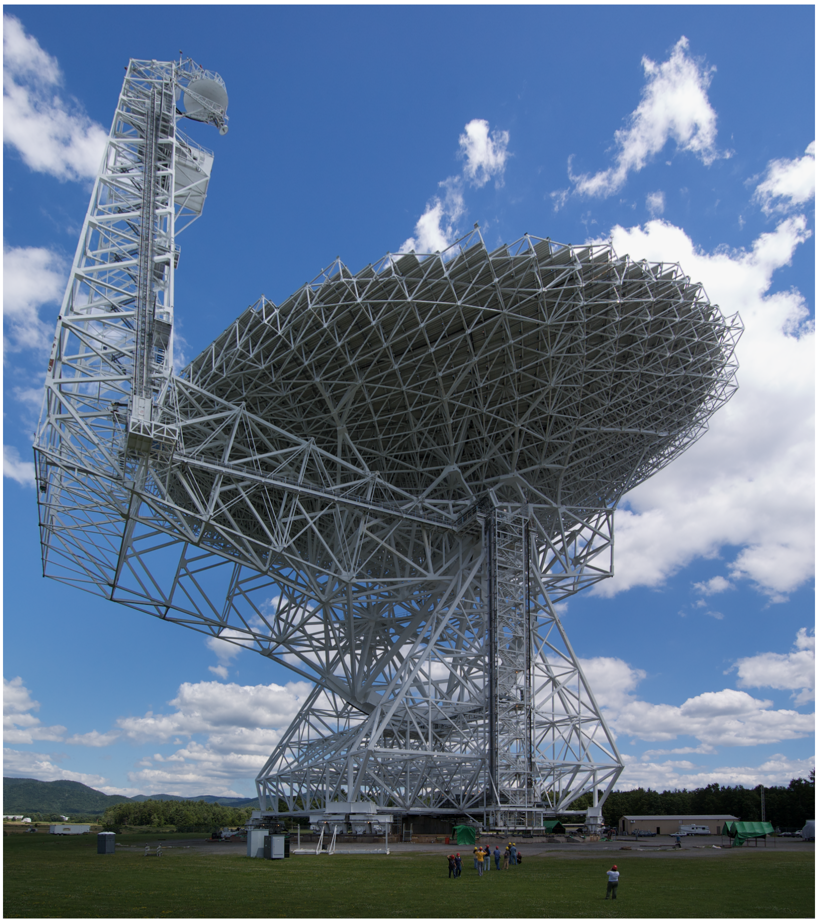

Figure 2.2: The GBT antenna, 148 m in height, has an arm supporting the primary focus that is cantilevered from behind the dish. In this way, the subreflector does not shade the primary mirror.

The operative frequency range extends from 290 MHz to 115.3 GHz, which means that GBT can be used for multiple scientific targets, from molecular emissions at mm wavelength range to the important HI line at 21 cm. To cover almost three orders of magnitude in frequency, several receivers are mounted, both at the primary focus and at the Gregorian one. An innovative one is the K-Band Focal Plane Array (KFPA), located at secondary focus, which has a total of seven beams with a spectral coverage of $[18.0 - 27.5]$ GHz. The seven feeds, organized in an hexagonal structure, have each a polarizer for circular polarization and a noise diode for calibration. Table 2.1 summarizes its main features.

Table 2.1: KFPA main parameters (Ref.: GBT Observing Guide and GBT Proposer's Guide).

Range (GHz)	Focus	Polariz.	n. beams	Gain (K/Jy)	Aperture eff. [1]
[18.0 – 27.5] GHz	Greg.	Circular	7	1.9	68%

[1] The beam efficiency is 1.37 times aperture efficiency

The signal coming from the frontend enters one of the backends available at GBT, designed for different purposes: continuum and line observations, as well as pulsar ones, are available. The instrument for spectroscopic investigations is VEGAS (VErsatil GBT Astronomical Spectrometer), which consists of 8 spectrometers, also called banks, that can work simultaneously. Furthermore, their bandwidth and spectral resolutions can be set independently: as a consequence, VEGAS is an extremely versatile and efficient instrument, especially if used with the KFPA frontend. Within certain limits, the observers can choose among a large number of possible beam-bank configurations. For example, one can use just one KFPA beam routed to all VEGAS spectrometers, maximizing the bandwidth, or use at the same time all the seven beams and the eight banks, a useful configuration for mapping. In the latter case, one can add the signal from the 7 beams for the same line and improve signal-to-noise ratio, losing though angular resolution, since the beams are at different locations.

As far as observing modes are concerned, we must distinguish between utility modes, which are used to characterize the telescope pointing, focus, efficiency, and observing techniques, for which a number of solutions are available. GBT allows both single pointing observations and mapping, the latter achieved through a technique called *On-the-Fly* (OTF): in a rectangular region of the sky the telescope slews along the R.A. or Dec axis according to observer's choice. Usually, radio observations are made with the so called ON-OFF method: the signal coming from observing the source (ON) is compared to an observation sourceless (OFF), which ideally contains only noise. This technique can be done in different ways: in *position switching*, after or before on-source observation the telescope is pointed to a sky region thought to contain no signal for the same time. A *frequency switching*, instead, consists in periodically changing the observation center frequency between two values. The resultant spectrum, if the frequency shift is small enough, will contain the line twice: they can be folded, obtaining a $\sqrt{2}$ increase of the signal-to-noise ratio. In addition, this method maximizes the on-source time. GBT provides both options, as well as beam and polarization switching.

2.3 Observations

2.3.1 Instrument setup

The B59 ammonia data were observed between 2015 and 2016 as part of a large legacy survey at GBT, the Green Bank Ammonia Survey (GAS - Pineda, Friesen et al. (in prep.)), aiming to map the ammonia emission from the nearby ($d < 500\,\mathrm{pc}$) star forming regions of the Gould Belt such as the Pipe Nebula. The survey investigates about a dozen molecular clouds with the following molecular lines: ammonia transitions (1,1), (2,2) and (3,3), HC_5N (9-8 line) and HC_7N (21-20 and 22-21 lines), as well as CCS 2_1 - 1_0 transition.

Table 2.2: Main GBT setup parameters.

Parameter	Setup	Comments
Frontend	KFPA	*7 beams used*
Backend	VEGAS	
Backend Mode	20	
n. Banks	7	
Spectral windows per bank	8	
Bandwidth	23.44 MHz	
n. Channels	4096	*n. chans per spectral windows*
Spectral resolution	5.72 KHz	$0.07\,km\,s^{-1}$ *at* 23 *GHz*
Switching mode	Frequency	*in-band freq. switch.*
Mapping mode	OTF	
Beam FWHM	$31.8''$	*Corresponding to* 0.02 *pc*
Beam efficiency	0.89	*At ammonia (1,1) rest freq.*

GAS used the KFPA receiver with VEGAS, set in configuration Mode 20, which allows to have in each bank 8 spectral windows with 23.44 MHz bandwidth and 4096 channels. This translates in a spectral resolution, i.e. the FWHM of a single channel, of 5.72 KHz, corresponding to $\approx 0.07\,\mathrm{km\,s^{-1}}$ at $\nu = 23\,\mathrm{GHz}$. Two spectral windows are centred in ammonia (1,1) and (2,2) rest frequencies, which are respectively $\nu_{11} = 23694.4955\,\mathrm{MHz}$ and $\nu_{22} = 23722.6336\,\mathrm{MHz}$. This setup allows to use an in-band frequency switching as observing mode, with a frequency switch of 4.11 MHz. At 23.7 GHz, KFPA beam has FWHM[2] $\approx 31.8''$, which at a distance of 145 pc is equivalent to ≈ 0.02 pc of spatial resolution.

---

[2] FWHM is a synonymous for FWHP.

The maps were obtained using the OTF mode, scanning the sky in $10' \times 10'$ boxes along Right Ascension, in rows spaced by $13''$ in Declination. When needed, i.e. for large sources such as the Pipe, several boxes were joined together. Table 2.2 summarizes the most important specification of the instrumental setup.

2.3.2 Data Reduction

Each KFPA beam has a noise diode to determine the absolute flux scale for the observations. The injected noise level has been verified in the laboratory, and its tabulated value can differ from the actual one once the diode is mounted on the telescope. In order to correct this problem, astronomical sources with a known modelled emission are used as primary calibrators. GAS used the Moon and the planets Jupiter and Venus as flux calibrators. The Moon in particular, due to its angular size large enough to cover all the KFPA footprint, was used to determine relative calibration between the seven beams. Data reduction and calibration to T_{MB} scale was performed using the standard KFPA pipeline. Background contributions have been removed through baseline subtraction, fitting to it a polynomial function of first order for (1,1) transition and third order for (2,2).

The gridding of the On-The-Fly observations was made according to Mangum et al. (2007) prescriptions. The pixel size was set to be 1/3 of the beam size, in order to avoid undersampling. To determine the final spectrum in each pixel, all the different observations within a beam distance from it were averaged. Each integration has been given a weight depending on its noise level, measured by the recorded T_{sys}.

The resulting data for B59 contain two spectral cubes, consisting each of two spatial axis and a spectral one. Spatial coordinates range from $17^h10^m51.8^s$ to $17^h11^m55.5^s$ in Right Ascension and from $-27°32'27.6''$ to $-27°18'29.2''$ in Declination. Each spectral plane contains 81×80 pixels. The (1,1) cube is made of 763 channels in the $[-24.95 - +30.22]\,\mathrm{km\,s^{-1}}$ velocity range, while the (2,2) contains only 350 channel in the range $[-9.23 - +16.01]\,\mathrm{km\,s^{-1}}$, half size of the former since this transition is too weak to detect satellite lines.

2.4 Results

Figures 2.3 and 2.4 show the integrated intensity maps (moment 0) obtained respectively integrating emission over channel ranges $[340 - 400]$ for the (1,1) line and $[150 - 200]$ for the (2,2). The latter appears less extended and fainter than the (1,1), with a peak value of less then $1.0\,K\,\mathrm{km\,s^{-1}}$.

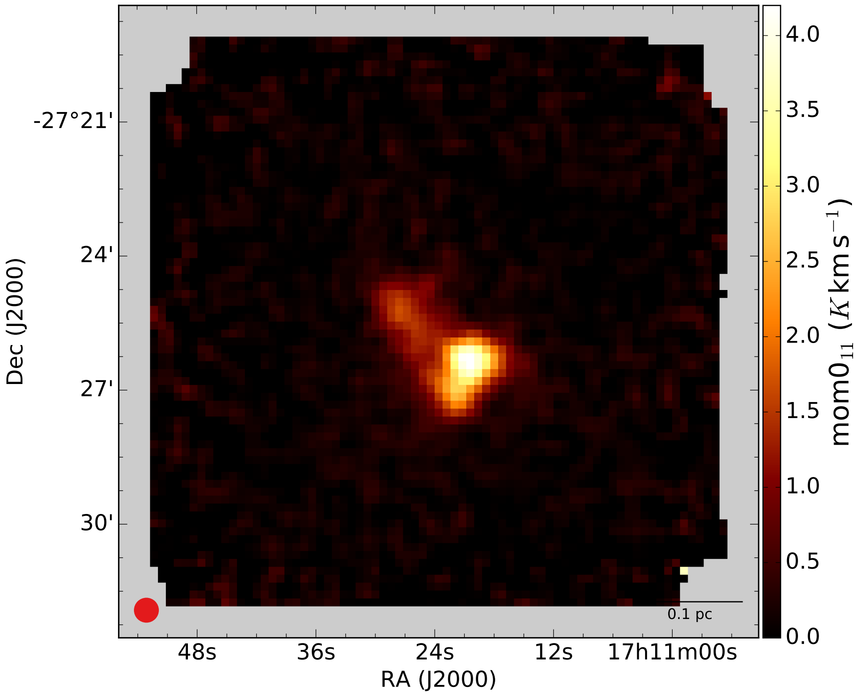

Figure 2.3: Integrated intensity map for the NH_3 (1,1) transition.

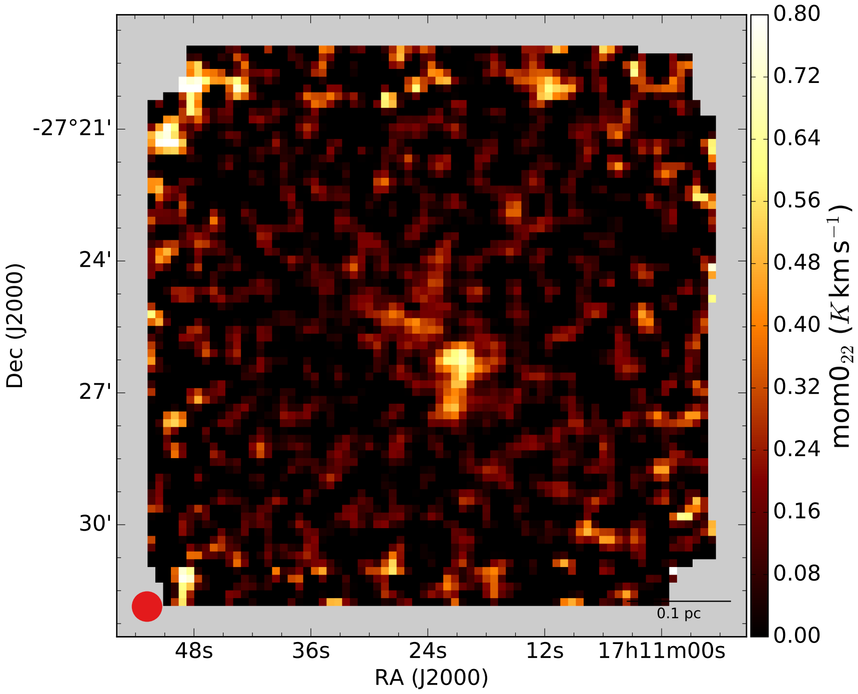

Figure 2.4: Integrated intensity map for the NH_3 (2,2) transition.

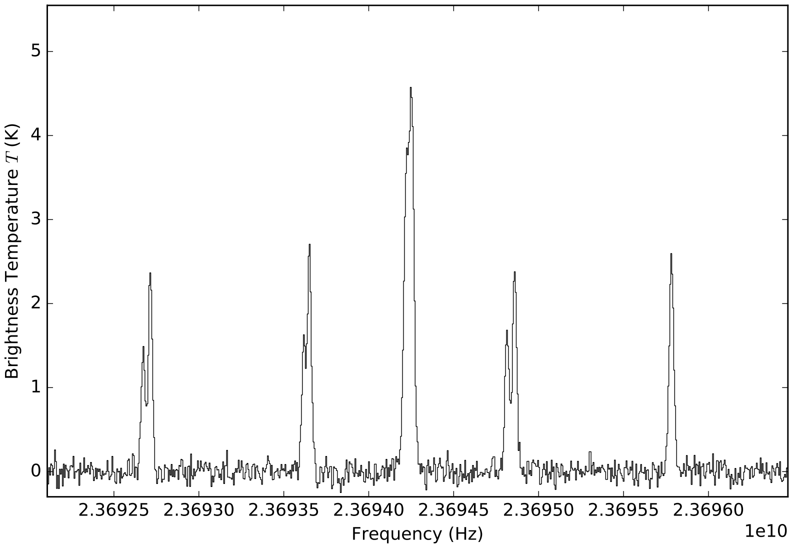

Figure 2.5: Averaged spectrum from the NH_3 (1,1) data cube obtained from a circular region centred in pixel [45,35] and with a 3 pixel size diameter.

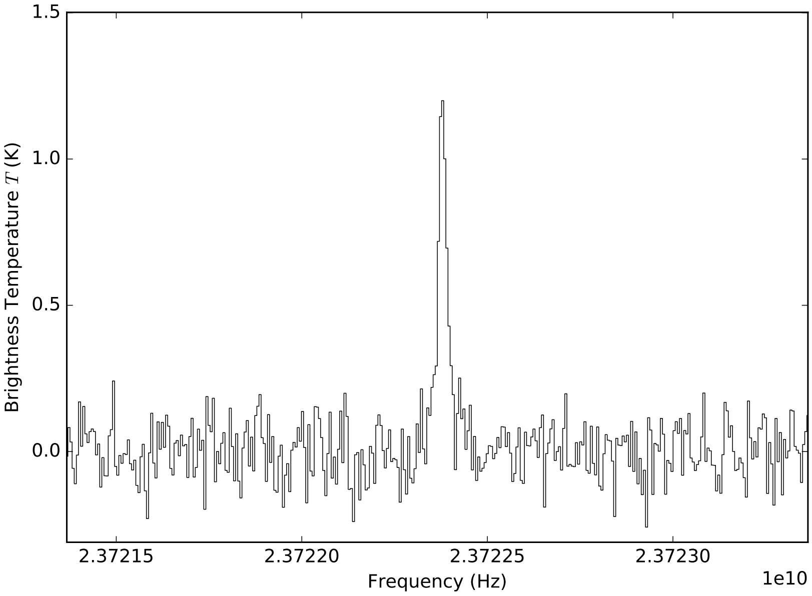

Figure 2.6: Averaged spectrum from the NH_3 (2,2) data cube obtained from a circular region centred in pixel [45,35] and with a 3 pixel size diameter.

In Figure 2.5 we present the averaged spectrum for (1,1) transition taken from a circular region containing the brightest emission. The main central line is visible as well as the two pairs of satellites. Due to the good spectral resolution, one can also appreciate the hyperfine components of the line. Figure 2.6 shows same analysis on (2,2) cube.

To estimate the rms of our map, we have computed at each pixel the standard deviation along spectral axis for all line-free channels, which are $[0-70; 135-245; 290-340; 400-440; 500-620; 660-740]$ for (1,1) transition and $[10-149; 205-305]$ for (2,2). Results are shown as histogram in Figure 2.7. Data have been binned with a spacing of $0.015\,K$. For both lines a double peak shape is visible: a first global maximum is found at rms $\approx 0.13\,K$. The second peak, instead, is located at rms $\approx 0.28\,K$ and its mainly due to pixels at the edges of the map, which are noisier but do not contain any emission from the source. Averaged value from rms maps, excluding the noisy edges, is $0.15\,K$ for both lines. This value is slightly higher than the target level that the GAS survey wanted to achieve (rms $\approx 0.1\,K$), due to the fact that Barnard 59 does not reach high elevation at the Green Bank latitude. As a consequence, the airmass is higher than for other sources, and spectra result noisier.

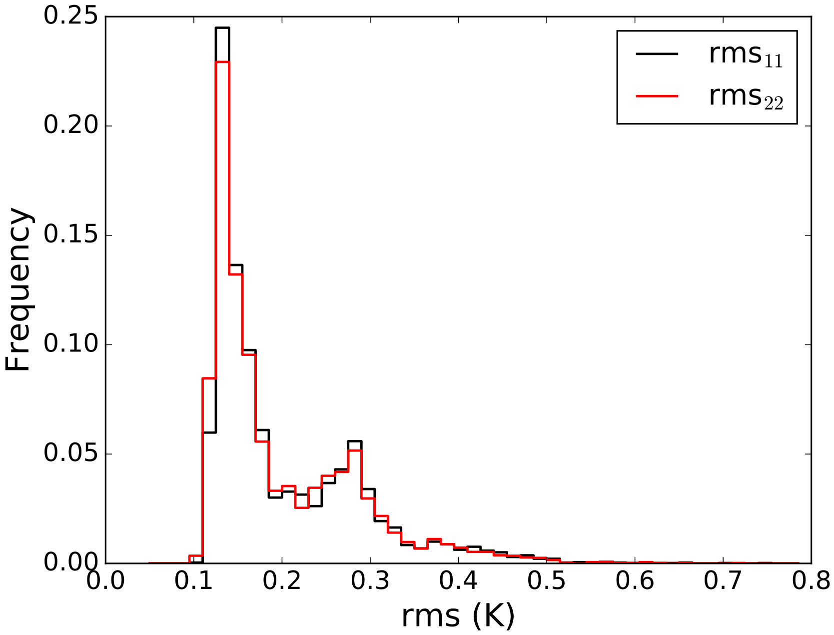

Figure 2.7: Frequency histogram for rms in both transitions.

Chapter 3

Ammonia analysis

In this Chapter I will describe the technique used to perform the spectral fitting on ammonia emission. In particular, I will explain why it has been necessary to improve the signal-to-noise ratio of the data, and which methods we have applied for this aim. The resulting maps of the physical parameters will be presented in the last Section.

3.1 Spectral fitting

The theoretical approach in ammonia spectroscopic analysis described in the Introduction is numerically achieved through a non-linear gradient descent regression. The method aims to find best-fit values for the free parameters, which in our case are N(NH_3) , T_K , T_{ex} , V_{lsr} , σ_V and the OPR. To perform this spectral fitting at each pixel of the cubes we use the Python library PYSPECKIT[1], which has been developed specifically to analyse spectroscopic data coming from single-pointing and mapping observations. This package already contains model spectra of many different species, including the NH_3 hyperfine structure, and is therefore a perfect tool for our study. The result of the entire procedure is a cube containing both the maps for each parameter and their uncertainties, evaluated using covariant-matrix approach.

Before starting the fitting, some preliminary information from the data are needed: rms, moment 1 and moment 2 maps, especially on the (1,1) transition. The last two variables have an important physical meaning: for a single Gaussian line, the first moment gives the velocity field, while the second one describes velocity dispersion in the source. While their definition and calculation are straightforward for lines with a simple profile, for ammonia-like spectra the situation is more

---

[1] PYSPECKIT is available at `https://github.com/pyspeckit/pyspeckit.git`

complex due to hyperfine splitting that can lead for example to wrong V_{lsr} values if not carefully taken into account.

Rms maps are evaluated as described in Sec 2.4. As far as the moments are concerned, since at this point we need only a rough estimation for them, the code proceed as follows: first it takes a slice of the (1,1) cube in the spectral window $[2-4]\,\mathrm{km\,s^{-1}}$, corresponding approximately to the channel range $[362-390]$, which contains the main line. Then it computes the searched variables according to their definition:

$$mom_1 = \frac{\int_{slab} V \cdot T_{MB}\, dV}{\int_{slab} T_{MB}\, dV}\ , \tag{3.1}$$

$$mom_2 = \sqrt{\frac{\int_{slab}(V - mom_1)^2 \cdot T_{MB}\, dV}{\int_{slab} T_{MB}\, dV}}\ . \tag{3.2}$$

The script is now ready to fit each pixel after stacking the two cubes together, which means that the (1,1) and (2,2) lines are analysed at the same time. In order to work properly the user must introduce initial guesses on parameter values, which after some tests have been set as shown in Table 3.1. Furthermore, for some of them their possible values have been limited to a specific range, avoiding non-physical solutions. Table 3.1 contains also these choices.

Table 3.1: Initial guesses for the fit

Parameter	Initial guess	Value range
$\log_{10}[\mathrm{N(NH_3)}]$ ($\mathrm{cm^{-2}}$)	14.5	$[12.0; 17.0]$
T_K (K)	12.0	$[5.0; -]$
T_{ex} (K)	8.0	$[2.8; -]$
V_{lsr} ($\mathrm{km\,s^{-1}}$)	3.37	$[2.0; 4.0]$
σ_V ($\mathrm{km\,s^{-1}}$)	0.11	$[0.04; -]$
OPR	1.0	fixed

The OPR has been kept fixed through all this work, since we have data only about two para-states. As far as the guesses for centroid velocity and velocity dispersion are concerned, instead, they are estimated from the moment 1 and moment 2 maps at the peak position. These initial guesses are actually used only for the brightest pixel, which is the first one to be fit. For the rest of the map we use the so-called *use neighbour as guess* approach, which allows to spread the solution across the source using the best values from already fitted points as guesses for the near ones. In order to avoid useless computing time on pixels which clearly contains no signal, we set a threshold in signal-to-noise ratio (hereafter SNR) based on a T_{peak} map, which contains the maximum signal for each pixel. We therefore mask all those points that do not fulfil the request:

$$\mathrm{SNR}_{peak} = \frac{T_{peak}}{\mathrm{rms}} > 3.0\ . \tag{3.3}$$

This procedure ends in selecting 661 pixels out of the original 6480.

Once the fitting is completed, one can access not only the parameter space and its uncertainties, but also the model fitted to each spectrum: Figure 3.1 shows the (1,1) transition for the brightest pixel in the map (position: R.A. $= 17^h 11^m 19.62^s$, Dec $= 27^\circ 26' 16.4''$), presenting both the observed data and the best-fit model. The fit appears to adjust well to the entire spectral range. Values found for the physical quantities are similar to the initial guesses.

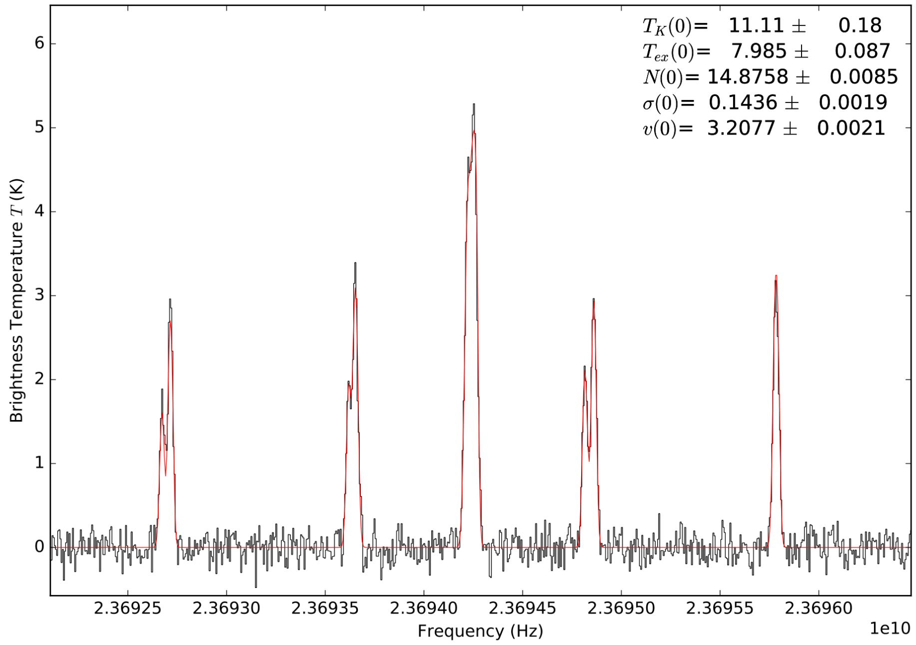

Figure 3.1: Original NH_3 (1,1) spectrum from brightest pixel (black line) with the best fit model computed by PYSPECKIT (red line); best-fit values of free parameters are shown in top-right corner.

3.1.1 New integrated intensity map evaluation

Once the fit is performed, we can proceed to evaluate new integrated intensity (i.e. moment 0) maps. In fact, the approach previously described makes use of a fixed spectral window containing the main line and therefore is not the best one, due to two main factors:

- For the (1,1) transition not only the main line, but also satellite ones should be involved in the integration;
- If velocity gradients are present in the source, a fixed channel range can lead to losing part of the signal and/or integrating over emission free channels.

Therefore, a more refined method in selecting the correct channel window is required. The chosen approach consists in using the best fit spectra just obtained to improve this selection. First of all we select pixels in each channel using the model signal taken from the best fit spectrum. Fluxes lower than $0.0125\,K$ are masked[2]. Pixels with velocity dispersion lower than three times its uncertainty ϵ_{σ_V} are considered poorly constrained. For them we use the mean $\overline{V}_{lsr}$ and $\overline{\sigma}_V$ on the whole field to select a spectral window according to $|\overline{V}_{lsr} - V_{ch}| < 3\overline{\sigma}_V$, where V_{ch} is the velocity of a generic channel. For (1,1) transition, $\overline{\sigma}_V$ is increased of $0.15\,\mathrm{km\,s^{-1}}$. Table 3.2 summarizes the results of this procedure.

Table 3.2: Spectral range selection for pixels with poorly constrained fit.

Line	$\overline{V}_{lsr}$ ($\mathrm{km\,s^{-1}}$)	$\overline{\sigma}_V$ ($\mathrm{km\,s^{-1}}$)	Range width	Central ch.
(1,1)	$3.44\,\mathrm{km\,s^{-1}}$	$0.36\,\mathrm{km\,s^{-1}}$	30 ch.	370
(2,2)	$3.44\,\mathrm{km\,s^{-1}}$	$0.21\,\mathrm{km\,s^{-1}}$	17 ch.	174

All channels selected are involved in the computation of the integrated intensity. The excluded ones, in addition, provide an estimation of the rms of the cube, computed as standard deviation. This noise level is used to associate uncertainties ϵ at each pixel to the integrated intensity through the following equation:

$$\epsilon = \mathrm{rms} \cdot \Delta V \cdot \sqrt{N_{chans}}\ , \tag{3.4}$$

where ΔV is channel width (in $\mathrm{km\,s^{-1}}$) and N_{chans} the number of channels involved in the integration. The obtained maps are shown in Figure 3.2a and 3.2b respectively for the (1,1) and (2,2) transitions. As previously mentioned, the latter is characterized by lower values than the former.

Figure 3.3 shows the final spectral window selection for a bright pixel and a low-signal one: in 3.3a there is a well defined spectrum, which allows to correctly select and use for the integration both the main line and its satellites. 3.3b, on the contrary, presents a noisy pixel, for which only a window centred in the main emission is found, according to the described criteria.

---

[2] This is an empirical value, selected after a few tests.

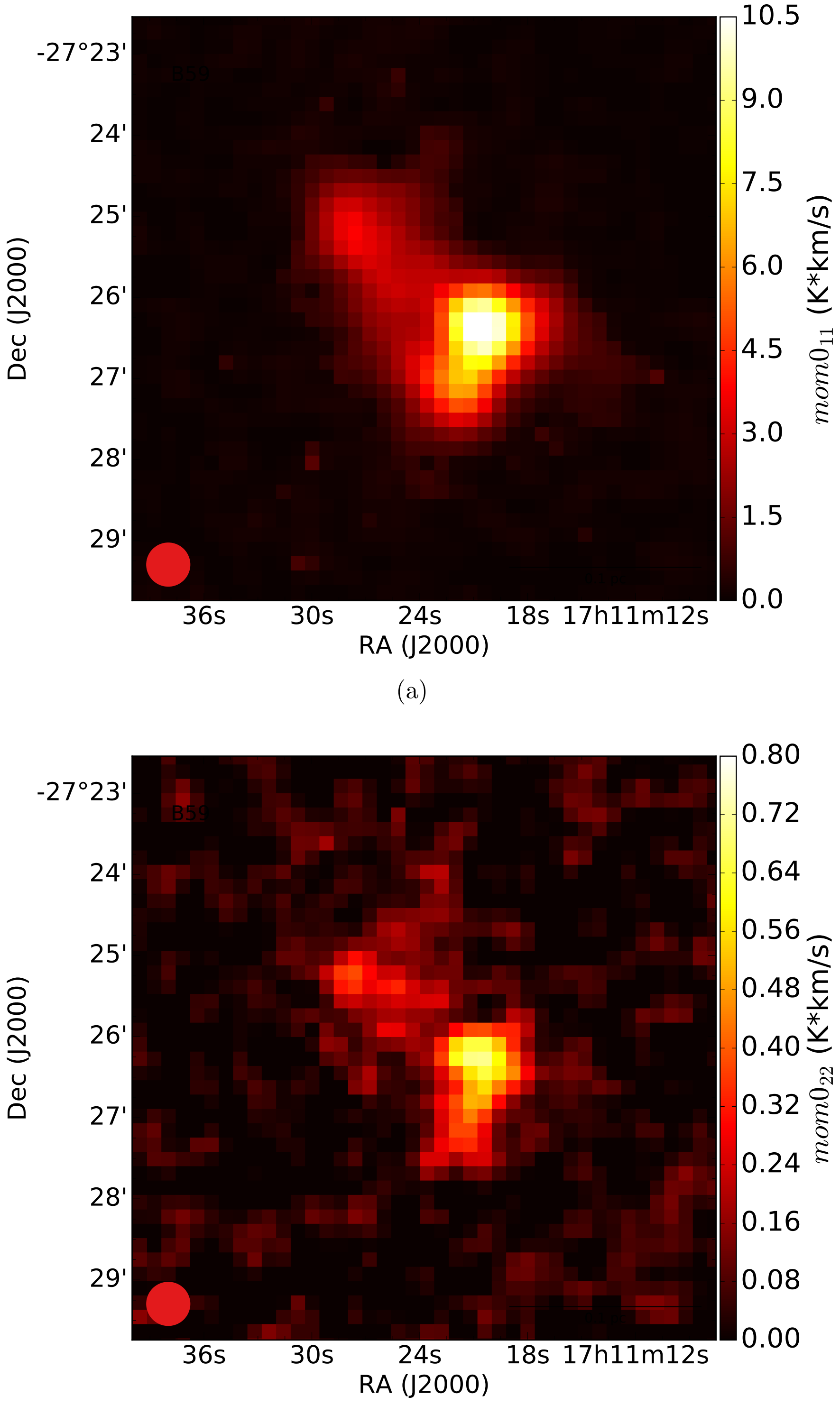

Figure 3.2: Resulting integrated intensity maps for NH_3 (1,1) (a) and (2,2) (b) transitions.

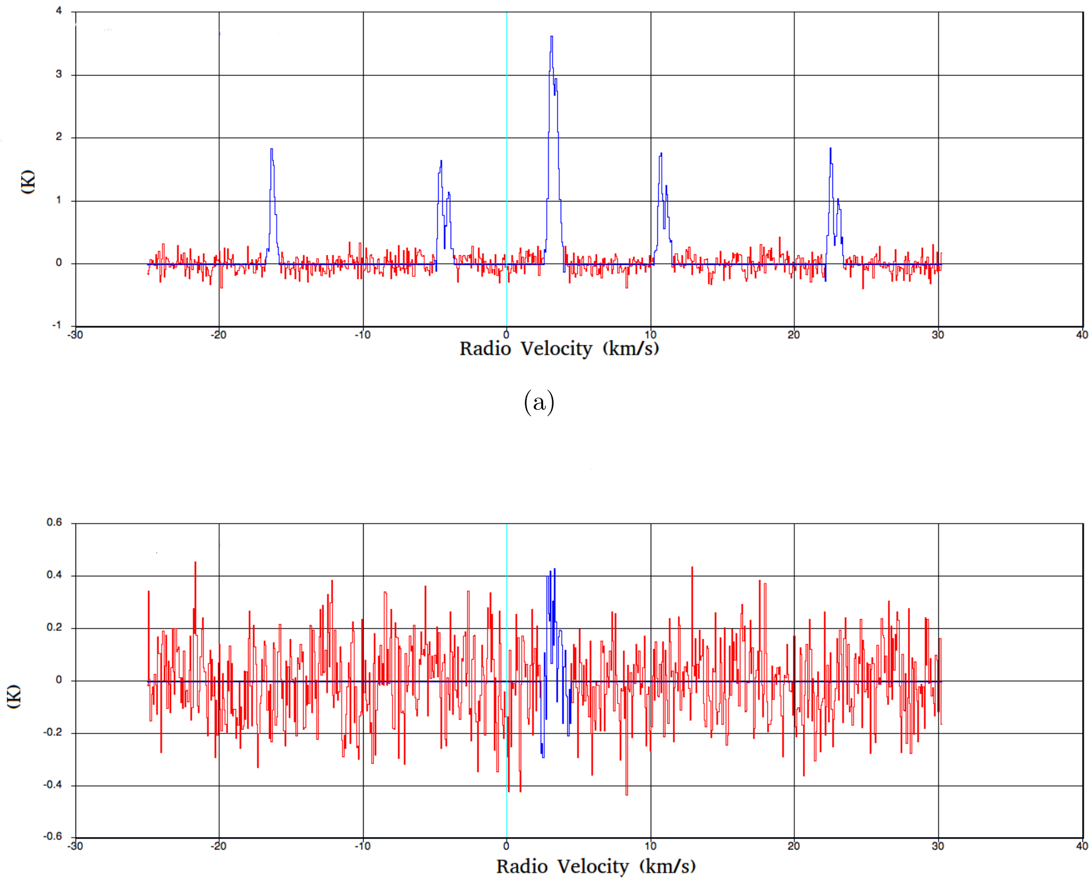

(a)

(b)

Figure 3.3: Channel range selection in two different cases for NH_3 (1,1) line: the upper panel shows an high SNR spectrum, the bottom one a low SNR one. Blue lines show which channels are involved in the integration.

3.2 Data flagging procedure

The parameter maps resulting from the fit needs a further flagging procedure, since that the initial threshold imposed to SNR_{peak} is not robust enough and it does not mask all pixels that should be excluded. This is a consequence of the fact that this method is sensitive to the presence of spikes in the spectra: since T_{peak} is simply the signal of the brightest channel for each pixel, it can happen that the threshold SNR_{peak} is satisfied even though the pixel contains only noise. Figure 3.4 shows in the upper panel the obtained $N(NH_3)$ map and in the lower one its uncertainties: the latter, especially in the outskirts of the source, tend to get high, indicating that at those positions the fit is poorly constrained.

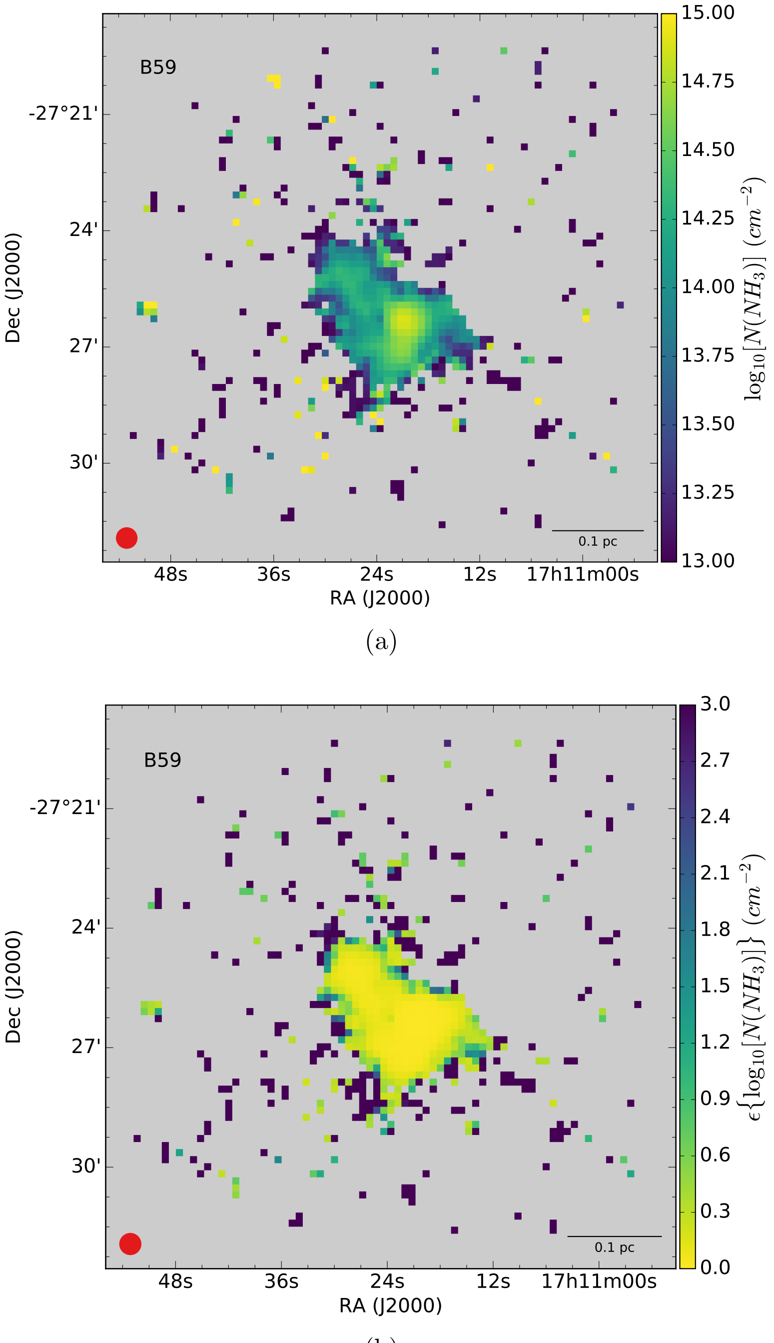

(a)

(b)

Figure 3.4: Best fit values for N(NH_3) (a) and its uncertainties (b): it is clear that for many points results are not reliable.

As a consequence, a new method is needed to exclude those points for which we do not have reliable values. This selection is achieved taking into account both the uncertainties for each parameter and the SNR in the integrated intensity map. This latter is defined at each pixel for the (J,J) transition as:

$$\mathrm{SNR}_{JJ} = \frac{mom0_{JJ}}{\epsilon_{JJ}} \ , \tag{3.5}$$

where ϵ is the uncertainty in the integrated intensity as defined in Eq. (3.4). Table 3.3 summarizes the criteria chosen for this selection. It is important to notice that, while for V_{lsr} , σ_V and T_{ex} a detection above the 3σ level in the (1,1) integrated intensity is sufficient, for N(NH_3) and T_K we need a SNR high enough also in the (2,2), because the determination of these parameters depends basically on the ratio between the two lines (see the Introduction). Therefore, the constrain $\mathrm{SNR}_{22} > 3.0$ is required.

Table 3.3: Pixels selection criteria for different variables.

T_K	$\mathrm{SNR}_{22} > 3.0$ $T_K > 5.0\,K$ $\epsilon_{T_K} < 3.0\,K$
T_{ex}	$\mathrm{SNR}_{11} > 3.0$ $T_{ex} > 2.8\,K$ $\epsilon_{T_{ex}} < 3.0\,K$
N(NH_3)	$\mathrm{SNR}_{22} > 3.0$ $T_K > 5.0\,K$ $\epsilon_{T_K} < 3.0\,K$ $T_{ex} > 2.8\,K$
σ_V	$\mathrm{SNR}_{11} > 3.0$ $\epsilon_{\sigma_V} < 0.1\,km/s$
V_{lsr}	$\mathrm{SNR}_{11} > 3.0$ $\epsilon_{V_{LSR}} < 0.1\,km/s$

This approach rises an issue: the (2,2) transition is faint, as one can already see from the moment 0 maps in Figure 3.2b. This problem is illustrated also in Figure 3.5, where points that satisfy $\mathrm{SNR} > 3.0$ for both lines are coloured green, while those for which only $\mathrm{SNR}_{11} > 3.0$ are shown in red: the analysis of column density and gas temperature is restricted to a very small subsection of the original map.

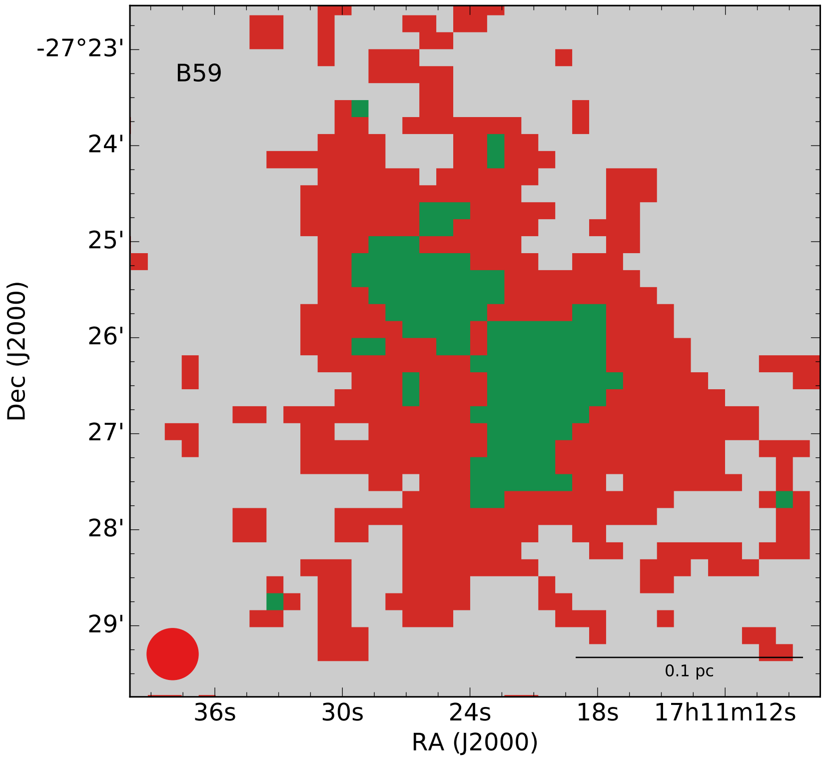

Figure 3.5: Different extension for integrated intensity detection in the two transitions: points detected above 3σ level for both NH_3 (1,1) and (2,2) lines are shown in green, those only for (1,1) line in red.

To recover part of the emission, and thus to investigate as much of the source as possible, we decided to apply some methods aiming to increase the SNR. This kind of procedures is divided in two main categories:

- *Smoothing methods*, which consist in a convolution of the image with a kernel, usually Gaussian. The final angular resolution decreases, but the total number of points is preserved, even though the number of independent one is lower;

- *Binning methods*, in which the signal from different pixels is averaged. The resulting map has lower resolution and also a lower total number of points.

We have tested both approaches on our data: procedures and results are described in the next sections.

3.2.1 Gaussian smoothing

Gaussian smoothing belongs to the more general class of resolution downgrading consisting in convolving the original image with a kernel. In this particular case, the latter is Gaussian in shape. This approach is widely used in astronomy not only for the purpose described in this section, i.e. increasing the SNR of a map, but also because it allows to combine images from different cameras or at different wavelengths that therefore have different point spread functions (PSF).

Let's suppose that the emission $S(x,y)$ from a source has been measured with an instrument characterized by a PSF $P_1(x,y)$: the observed image I_1 is the convolution of these two functions:

$$I_1(x,y) = P_1(x,y) \otimes S(x,y) = \iint P_1(x-x', y-y') \cdot S(x',y')\, dx'\, dy' \; . \tag{3.6}$$

We now would like to know the response of a second instrument about the same source:

$$I_2(x,y) = P_2(x,y) \otimes S(x,y) \; . \tag{3.7}$$

In order to know the relation between I_1 and I_2, it is convenient to apply Fourier transform FT to both Eq. (3.6) and (3.7). Since the original intensity distribution $S(x,y)$ is the same, with some little algebra one obtains [3]:

$$\left.\begin{aligned} FT\,(I_1) = FT\,(P_1) \cdot FT\,(S) \\ FT\,(I_2) = FT\,(P_2) \cdot FT\,(S) \end{aligned}\right\} \qquad FT\,(I_2) = FT\,(I_1)\,\frac{FT\,(P_2)}{FT\,(P_1)} \; . \tag{3.8}$$

Performing the inverse Fourier transform FT^{-1}, the final equation reads:

$$I_2 = FT^{-1}\left(\frac{FT\,(P_2)}{FT\,(P_1)}\right) \otimes I_1 \; . \tag{3.9}$$

This means that the new image can be obtained convolving the previous one with the function $FT^{-1}\left[FT\,(P_2)\,/FT\,(P_1)\right]$, which represents the *kernel* $K(1 \to 2)$. To apply this procedure to our data, suppose that both PSF have a Gaussian shape, such as:

$$P_i(x,y) \propto e^{-\frac{x^2+y^2}{\theta_i^2}} \qquad \rightarrow \qquad FT\,(P_i)\,(w,z) \propto e^{-\frac{\theta_i^2(w^2+z^2)}{4}} \; . \tag{3.10}$$

It is easy then to compute that

$$\frac{FT\,(P_2)}{FT\,(P_1)}(w,z) \propto e^{-\frac{(\theta_2^2-\theta_1^2)(w^2+z^2)}{4}} \; . \tag{3.11}$$

---

[3] We're applying the *convolution theorem*, according to which the FT of a convolution of two function equals the product between the FT of each function.

The inverse-transform of this last equation is the function $K(1 \to 2)$ we are looking for, which has again a Gaussian shape:

$$K(1 \to 2) \propto e^{-\frac{x^2+y^2}{\theta_2^2-\theta_1^2}} \, . \tag{3.12}$$

In conclusion, if we have a map with a resolution θ_1 and we want to downgrade it to $\theta_2 > \theta_1$, the original image must be convolved with a Gaussian kernel with standard deviation $\theta_K = \sqrt{\theta_2^2 - \theta_1^2}$.

In this work we have used the dedicated task *imsmooth* of the software CASA (McMullin et al., 2007) to perform this operation. We have set the final beam size on the value $FWHM = 40''$, which correspond to a loss of 25% in angular resolution. The procedure is structured in the following steps:

- First, the (1,1) and (2,2) cubes are smoothed;
- A new rms map is computed from the (1,1) transition;
- The cubes are then fitted again as explained in sec. 3.1;
- New moment 0 maps are evaluated and used to flag data, in order to obtain final parameter maps, which will be described in the following section (3.3).

3.2.2 Voronoi binning

Binning techniques, as previously mentioned, increase the SNR of a map by averaging the signal across several pixels. The Voronoi method is an example of this typology, which moreover has the characteristic of being *adaptive*: the bins are formed only where needed, i.e. in those parts of the map with low signal-to-noise ratio. Furthermore, it satisfies all requirements that a good binning scheme should have, which are:

1. Topological requirement: bins selected must cover the entire region of sky under study, without leaving holes or overlapping;
2. Morphological requirement: bins should be as round as possible, and contain only adjacent pixels;
3. Uniformity requirement: the SNR scatter between different bins should be small.

The theoretical formulation and code implementation have been developed by Cappellari & Copin (2003) to be applied to integral-field spectroscopic data (IFS), and have been widely used in that field as well as for high energy data from X-ray space telescopes. On the other hand, this work is the first example of its application to molecular spectra in the radio wavelengths range.

Before describing the theory, a brief introduction about SNR algebra is needed. Given a map, each pixel has a signal S_i and a noise N_i that define a signal-to-noise ratio S_i/N_i. If two pixels are coadded, the total SNR will be:

$$\mathrm{SNR}_{12} = \frac{S_1 + S_2}{\sqrt{N_1^2 + N_2^2}} \, . \tag{3.13}$$

Equation (3.13) can be simplified in two cases: whether the noise affecting the data is Poissonian ($N_i \approx \sqrt{S_i}$), or if one associates to each pixel the weight $w_i = S_i/N_i^2$ during the binning procedure. In these situations, the formula becomes:

$$\mathrm{SNR}_{12} = \sqrt{\left(\frac{S_1}{N_1}\right)^2 + \left(\frac{S_2}{N_2}\right)^2} \, , \tag{3.14}$$

which means that the squared power of SNR is an additive quantity. A generalization of the algorithm, releasing the hypothesis of poissonian noise or optimal weighting, has been introduced by Diehl & Statler (2006).

The Voronoi binning method (VB) is based on the concept of *Voronoi tessellation* (VT): a VT of a region Ω according to a collection of N points $\{q_i\}_{i=1}^N$, called *generators*, is a partition of Ω in N regions V_i, each of which contains the points closer to the generator q_i than any other. One can see that a VT immediately satisfy requirement n.1. As far as requirement n.2 is concerned, even though the bins created are at least convex, they still can be extremely elongated and therefore some controls on their shape are needed.

The most interesting and difficult part, though, regards how to achieve a constant SNR among the bins. Usually the problem is tackled as follows: suppose to be in the situation described by Eq. (3.14). We can assign an artificial density distribution to the map according to $\rho(r) = (\mathrm{SNR})^2\,(r)$, where r is a coordinate describing positions in the map. Requirement n.3 translates then in looking for bins of constant "mass" $M = \rho A_{bin}$, where A_{bin} is the bin area. It is useful in this situation to define a peculiar type of VT, called *centroidal voronoi tessellation* (CVT), in which the generators coincide with the mass centroids:

$$q_{i,C} = \frac{\int_{V_i} \rho(r) r \, dr}{\int_{V_i} \rho(r) \, dr} \, . \tag{3.15}$$

CVT bins are not naturally equal in mass. Nevertheless, we can take into account Gersho conjecture (Gersho, 1979), according to which, if l is the typical linear size of a bin, the product $\rho\, l^4$ is roughly constant (which mean that tends to be asymptotically constant in the limit of large number of bins). Furthermore, since the mass is proportional to bin area, and this latter depends on l as $A_{bin} \propto l^2$, one can see that $M \propto \rho\, l^2$. Therefore, if we calculate a CVT using the modified density $\widetilde{\rho} = \rho^2$, as a consequence of the previous relations we have:

$$M \propto \rho\, l^2 \propto \widetilde{\rho}^{\frac{1}{2}}\, l^2 \propto l^{-2}\, l^2 \approx \text{const} . \tag{3.16}$$

This CVT produces bins with equal mass according to the density ρ, and is consequently called *equimass-CVT*.

To implement this theory, a code must consist of these steps:

1. Make an initial choice of generators $\{q_i\}_{i=1}^{N}$ and compute a VT;
2. Compute mass centroids for all V_i according to $\widetilde{\rho}(r) = (\mathrm{SNR})^4\,(r)$;
3. Use these last to generate a new tessellation;
4. Iterate steps 2 and 3 until mass centroids do not change position any more.

The most delicate point in the list is 1: the initial set of generators, in fact, must be good enough to let the code converge. A specific algorithm has been developed, and will be now described.

Bin accretion algorithm

The underlying philosophy assumed to create the first VT of the map is to accrete bins adding at each iteration the closest unbinned pixel, and to check which is its influence on the shape and SNR of the resulting new bin. In order to do so, the code starts the first bin from the point with highest SNR and then it selects the unbinned pixel closest to the present bin mass centroid. In order to decide if this pixel can be added or not, three checks are performed:

- The new pixel must be adjacent to the bin (in respect of the topological requirement);
- Defining the bin maximum radius R_{max} as the maximum distance between the centroid and any of the bin pixels and its effective radius R_{eff} so that $\pi R_{eff}^2 = A_{bin}$ (R_{eff} is the radius of a disc of the same area of the bin) , the code verifies if

  $$\frac{R_{max}}{R_{eff}} - 1 < 0.3 . \tag{3.17}$$

  This allows to maintain the bins “roundish” enough, in agreement with the morphological requirement;

- The SNR of the bin, adding this pixel, must get closer to the target value previously decided (SNR_T).

If all these criteria are correctly fulfilled, the pixel under analysis is definitely added to the bin. Its mass centroid is re-evaluated, and the unbinned pixel closest to it is selected, starting a new cycle. A bin is accreted until either one of the tests fails or if its total SNR reaches a given fraction of the target SNR (in our code, the 80%): in the first case, the resulting bin is marked as "unsuccessful". Once one bin is completed, a new one is started, until the entire map has been scanned. Pixels unsuccessfully binned are then assigned to the closest mass centroid of a "successful" bin. This procedure allows to determine the first Voronoi Tessellation, which is used to create an equimass-CVT as described in the previous section.

Diehl & Statler modification

As already pointed out, the Voronoi binning method is suitable for data for which the quantity $(\mathrm{SNR})^2$ is additive. In many cases, like ours, this is not necessarily true. Diehl & Statler (2006) have introduced a modification to the original algorithm which allows to use it in a wider range of situations.

The new approach introduced by this change is to alter the metric system inside each bin introducing a scale length factor:

$$\delta_i = \sqrt{\frac{A_i \cdot \mathrm{SNR}_T}{k \cdot \mathrm{SNR}_i}} \,, \tag{3.18}$$

where A_i is the bin area, SNR_i is its signal-to-noise ratio, k a dimensionless constant (depending on bin shape) and SNR_T is the target value the code aims to reach. In a standard VT, each pixel x_k is assigned to the $i-$bin whose centroid q_i minimizes the distance $|x_k - q_i|$. The new version of the algorithm, instead, minimizes the quantity:

$$\frac{|x_k - q_i|}{\delta_i} \,. \tag{3.19}$$

Since the binning depends on the ratio between the scale lengths δ_i/δ_j of two different bins and given that both SNR_T and k are constants, in the code Eq. (3.18) is substituted by:

$$\delta_i = \sqrt{\frac{N_i}{\mathrm{SNR}_i}} \,, \tag{3.20}$$

where N_i is the number of pixels belonging to the bin, which is a good proxy of its area. The method, called *weighted-VT* (WVT), is independent from Gersho conjecture. The goal of equi-SNR bins is naturally achieved, and therefore the procedure is structured in the following step:

1. An initial VT is set with the bin accretion algorithm already explained;
2. For each bin the quantities N_i, SNR_i, δ_i and q_i are evaluated;
3. Pixels are reassigned, following equation (3.19);
4. Steps 2 and 3 are iterated until the bins do not change any more.

Application to ammonia data

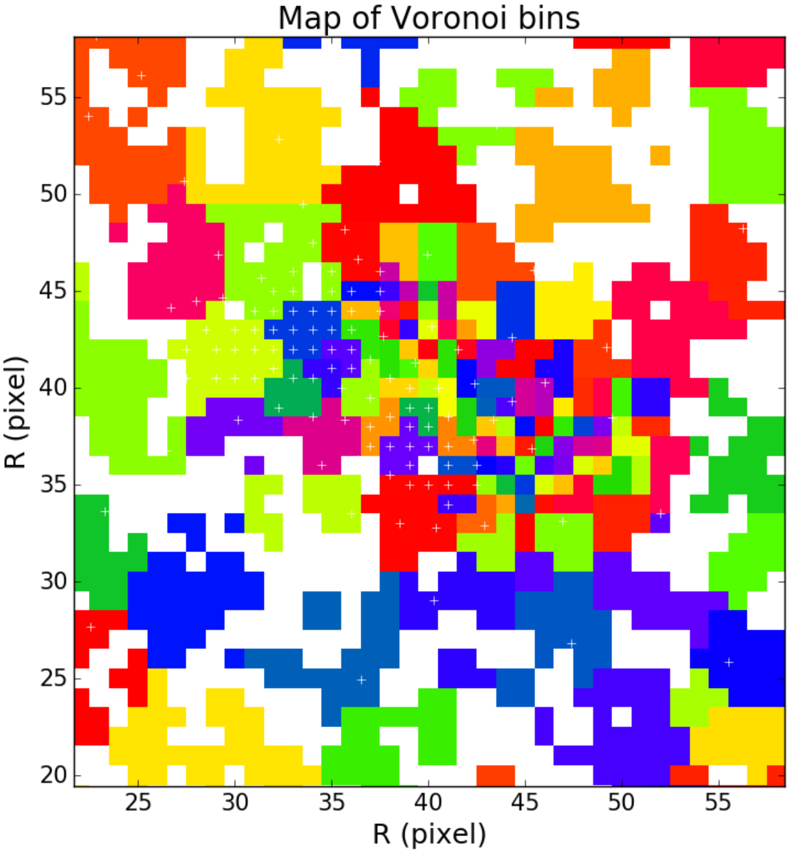

Figure 3.6: Bins identified by VB procedure. Colours are randomly chosen and different for different bins. White crosses show centroid positions, while white pixels are those excluded from calculation. Figure is shown in pixel coordinates.

To apply the Voronoi approach to our data, we have used a python version of the code contained in the GAS scripts libraries. Since the problem is a too faint NH_3 (2,2) line, the binning is set according to SNR_{22} in integrated intensity.

After a few tests, the optimal target value turns out to be $\mathrm{SNR}_T = 5$. This value allows to obtain a good number of bins with a final SNR_{22} higher than 3.0, despite the scatter in signal-to-noise ratio that the code intrinsically permits. Since it can happen that, for pixels with extremely faint signal, the integration results in a negative intensity, we exclude these points masking them. The code finds 184 successful bins, which are shown in Figure 3.6: different colours represent distinct bins, and white crosses mark their mass centroids. The adaptive nature of this method is clear: bins tend to get larger while moving away from peak emission, located at the image center.

The script performing the WVT returns a map of labels, since an integer number is assigned to each different bin. This is used as an input for the function that actually bins the cubes, computing the average signal of pixels with the same index. As a result, each $i-$bin contains N_i identical points. In order to further improve this method, since we know that velocity gradient are present in the source and this could compromise the average calculation, we align the spectra to a common centroid, shifting them according to the V_{lsr} map already computed. Where values are missing, we use the mean $\overline{V}_{lsr}$ of the source.

Once the (1,1) and (2,2) cubes are binned, we proceed in the same way used for smoothing data: a new rms map for the (1,1) line is computed in order to exclude from the fitting procedure too noisy pixels. The condition $\mathrm{SNR}_{peak} > 3.0$ selects 1238 pixels for the fitting. The cubes are then fitted. Then new moment 0 maps can be evaluated and used to flag the data. Final maps for each free parameter are presented in the following section.

3.3 Results

In this section I will show and describe the resulting maps for each of the free parameters obtained with both the methods just introduced. We will also try to make a comparison between them, and draw some conclusions about which method is more suitable for our specific application.

3.3.1 Ammonia column density

Figure 3.7 shows results for ammonia column density. The two methods appear in agreement as far as both values and structure are concerned, even though some features visible in the VB map should be carefully examined. In fact, if bins grow very large we do not expect results to be reliable.

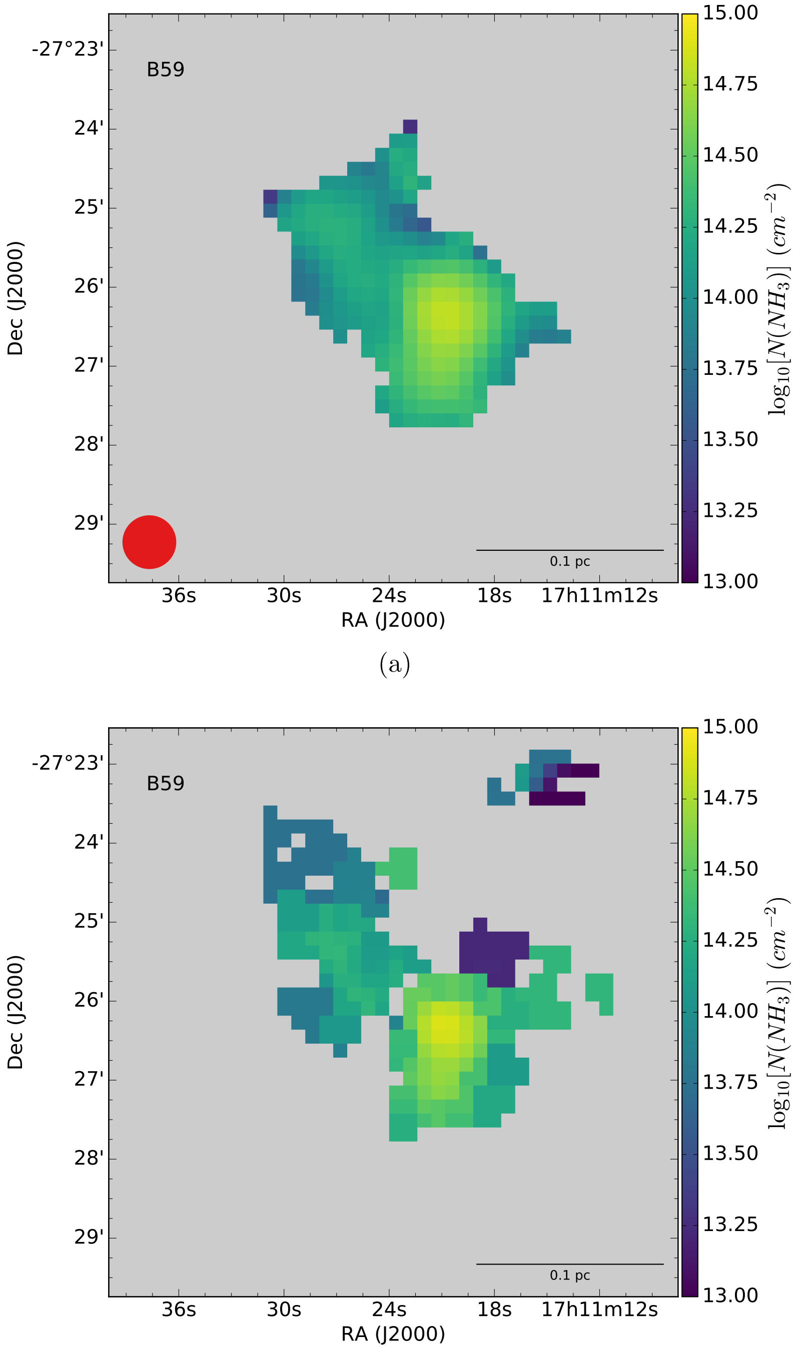

(a)

(b)

Figure 3.7: N(NH_3) map obtained with (a) smoothing and (b) Voronoi binning methods. The colour scale is the same for both images.

We can see a dense clump located in the south-western part of the source, where the ammonia emission peaks. The highest value is found at position R.A. = $17^h11^m21.25^s$, Dec = $-27°26'16.1''$ and is $\log_{10}(\mathrm{N(NH_3)}) = 14.81 \pm 0.01$ for the smoothed map and $\log_{10}(\mathrm{N(NH_3)}) = 14.89 \pm 0.01$ for the binned one. Hereafter, we will refer to this densest part of the cloud as the *coherent core*[4]. Another density enhancement, even if less dense that the previous one, can be found in the north-eastern part of the source. Here the maximum value found is $\log_{10}(\mathrm{N(NH_3)}) \approx 14.3$ in both maps. Finally, a third peak in column density is seen in the northern part of the cloud, peaking around position R.A. = $17^h11^m22.80^s$, Dec = $-27°24'40.9''$. The densest pixel has $\log_{10}(\mathrm{N(NH_3)}) = 14.30 \pm 0.15$ for smoothed data and $\log_{10}(\mathrm{N(NH_3)}) = 14.40 \pm 0.15$ for binned ones. Table 3.4 summarizes some properties of the map.

Table 3.4: Summary of $\mathrm{N(NH_3)}$ properties.

Parameter	Value ($\mathrm{cm^{-2}}$)	Uncert. ($\mathrm{cm^{-2}}$)	Position [1]
		Smoothing method	
Mean density	14.24	-	-
Peak density	14.81	0.01	($17^h11^m21.25^s$, $-27°26'16.1''$)
		VB method	
Mean density	14.10	-	-
Peak density	14.89	0.01	($17^h11^m21.25^s$,$-27°26'16.1''$)

[1] Right Ascension and Declination in J2000.0

3.3.2 Excitation temperature

The maps for the excitation temperature, which determine the population in the lower and the upper level in each inversion doublet, are presented in Figure 3.8. As expected, highest value are found in the densest regions, as a consequence of an higher rate of collisions between molecules. Averaged values for this quantity are $\overline{T}_{ex} = 4.32\,K$ in the smoothed image and $\overline{T}_{ex} = 4.43\,K$ in the binned one, but if we restrict only to the regions where $\log_{10}(\mathrm{N(NH_3)}) > 14.2$, we obtain respectively $\overline{T}_{ex} = 5.59\,K$ and $\overline{T}_{ex} = 5.25\,K$. It is interesting to see that at the position of the third peak found in the previous section, the excitation temperature is extremely low ($T_{ex} < 3.5\,K$ in both figures).

---

[4] The term coherent core was firstly introduced by Goodman et al. (1998) to describe regions with almost constant line-widths and subsonic non thermal motions. Further analysis will justify our choice of using this term here.

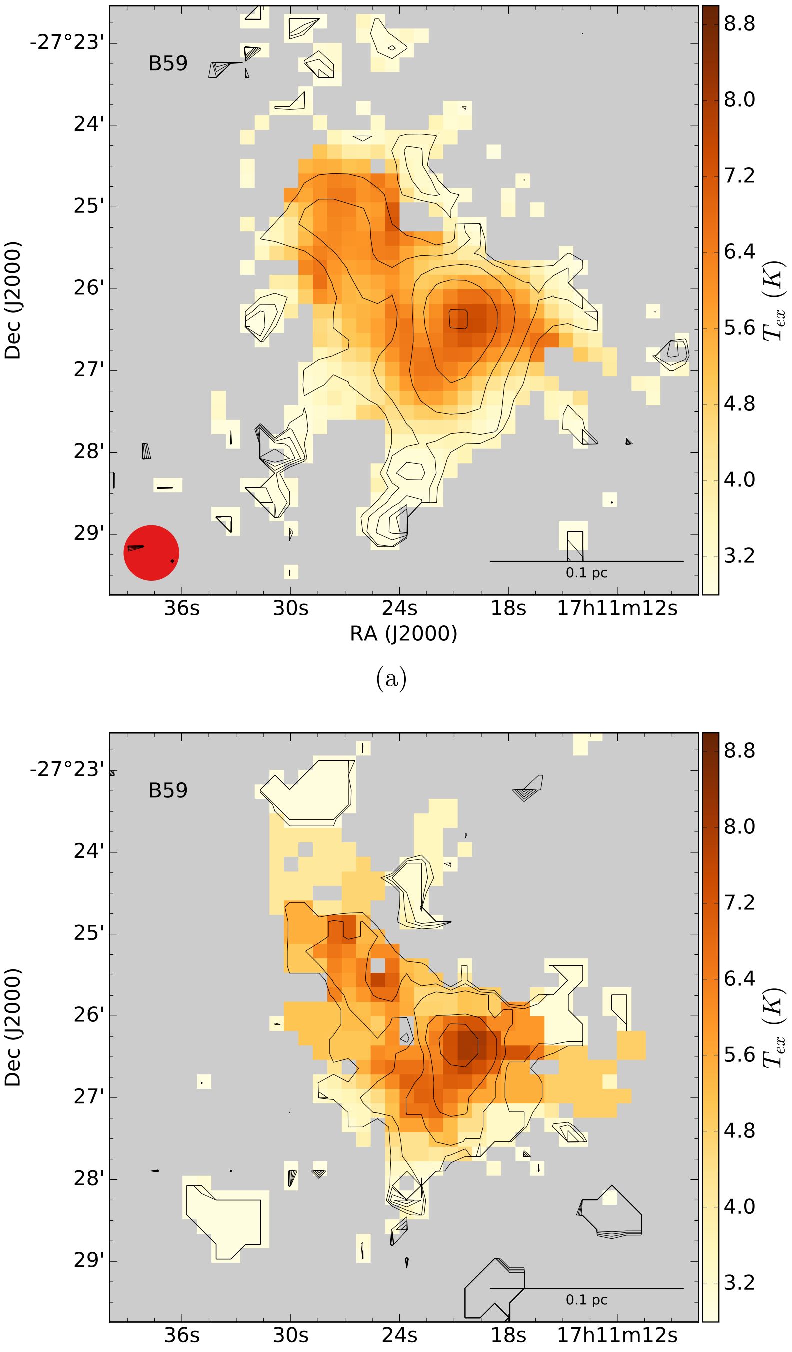

(a)

(b)

Figure 3.8: T_{ex} map obtained with (a) smoothing and (b) Voronoi binning methods. The colour scale is the same for both images. Contours are plot from $\log_{10}(\mathrm{N(NH_3)})$ at levels [14.0, 14.2, 14.4, 14.6, 14.8].

3.3.3 Kinetic temperature

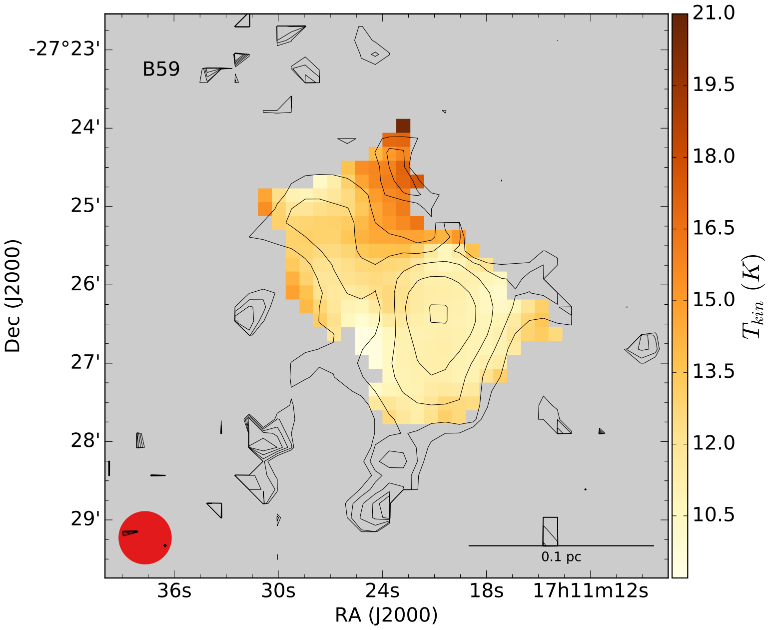

(a)

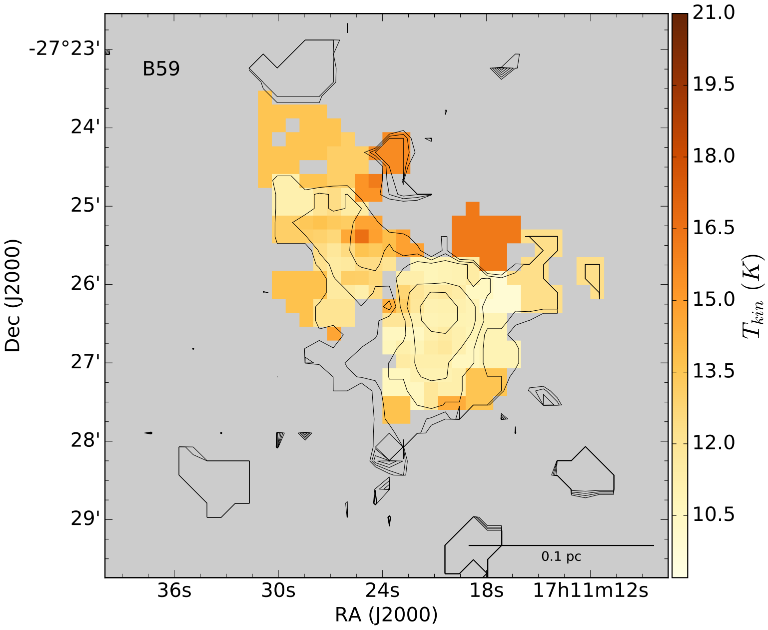

(b)

Figure 3.9: T_K map obtained with (a) smoothing and (b) Voronoi binning methods. The colour scale is the same for both images. Contours are plot from $\log_{10}(\mathrm{N}(\mathrm{NH_3}))$ at levels [14.0, 14.2, 14.4, 14.6, 14.8].

The two panels in Figure 3.9 show gas temperature respectively for smoothed data (3.9a) and Voronoi binned ones (3.9b). Similarly to the parameters already presented, the results of the two methods seem in agreement also for T_K . The coherent core is also the coldest part of the cloud: the mean kinetic temperature in the region where $\log_{10}(\mathrm{N(NH_3)}) > 14.4$ is $\overline{T}_K = 11.21\,K$ (smoothing) and $\overline{T}_K = 11.63\,K$ (VB). These are typical values for dense core heated only by the external radiation field (Caselli & Ceccarelli, 2012). Temperature are slightly higher in the north-eastern clump: we find $T_K \approx 13.3\,K$ in smoothed image, and $T_K \approx 13.7$ for VB one. The highest temperatures are found in the northern part of B59, where they reach $16 - 17\,K$, which means that another source of heating is needed beside standard cosmic ray field or surrounding radiation field. Table 3.5 contains some important properties of the maps.

Table 3.5: Summary of T_K properties.

Parameter	Value (K)	Uncert. (K)	Position [1]
		Smoothing method	
$\overline{T}_K$	12.38	-	-
$\overline{T}_K$ (coherent core)	11.21	-	-
Peak T_K	20.6	3.0	$(17^h11^m22.81^s, -27°23'58.4'')$
		VB method	
$\overline{T}_K$	12.69	-	-
$\overline{T}_K$ (coherent core)	11.63	-	-
Peak T_K	16.6	1.1	$(17^h11^m25.20^s, -27°25'23.3'')$

[1] Right Ascension and Declination in J2000.0

3.3.4 Local standard of rest velocity

Figure 3.10 shows results for the centroid velocity obtained fitting the ammonia spectra. The cloud kinematic structure is similar according to both the used methods. V_{lsr} values range is $\approx [3.0 - 4.0]\,\mathrm{km\,s^{-1}}$, in good agreement with previous estimations of this quantity (Onishi et al. 1999, Duarte-Cabral et al. 2012). Several gradients are visible, even though they are not very strong. The mean value is $\overline{V}_{lsr} = 3.50\,\mathrm{km\,s^{-1}}$ in the upper panel and $\overline{V}_{lsr} = 3.48\,\mathrm{km\,s^{-1}}$ in the lower one. The dense and cold core seems to be a coherent structure also from the kinematic point of view, with an average value of $\overline{V}_{lsr} = 3.29\,\mathrm{km\,s^{-1}}$. The scatter around this value, evaluated by the standard deviation on pixels with $\log_{10}(\mathrm{N(NH_3)}) > 14.4$, is low in both cases: $\sigma = 0.07\,\mathrm{km\,s^{-1}}$ for the smoothed map and $\sigma = 0.08\,\mathrm{km\,s^{-1}}$ in the binned one.

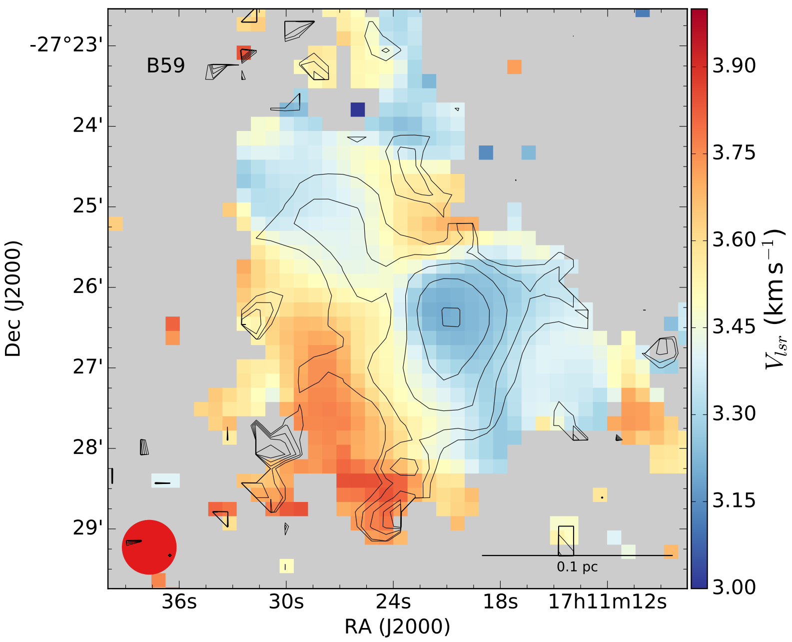

(a)

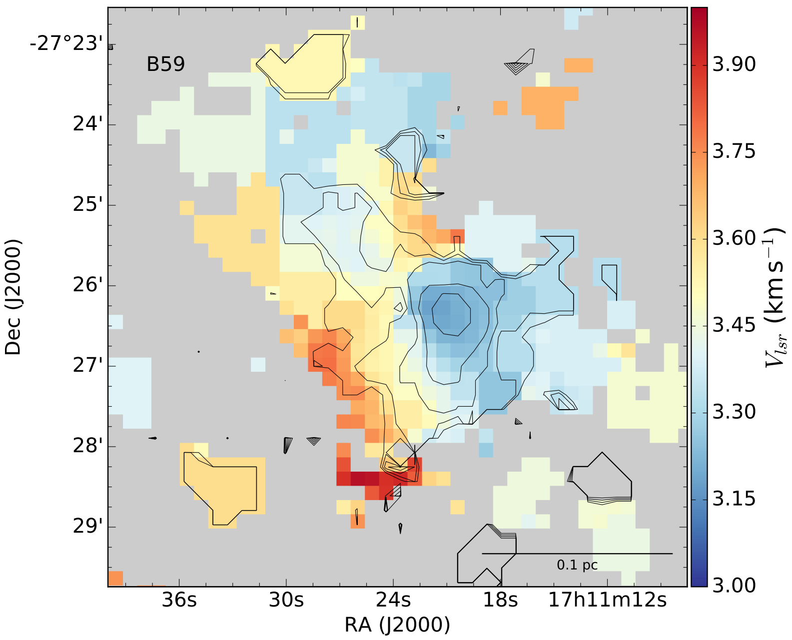

(b)

Figure 3.10: V_{lsr} map obtained with smoothing (a) and Voronoi binning (b) methods. Colour scale is the same for both images. Contours are plot from $\log_{10}(N(NH_3))$ at levels [14.0, 14.2, 14.4, 14.6, 14.8].

3.3.5 Velocity dispersion

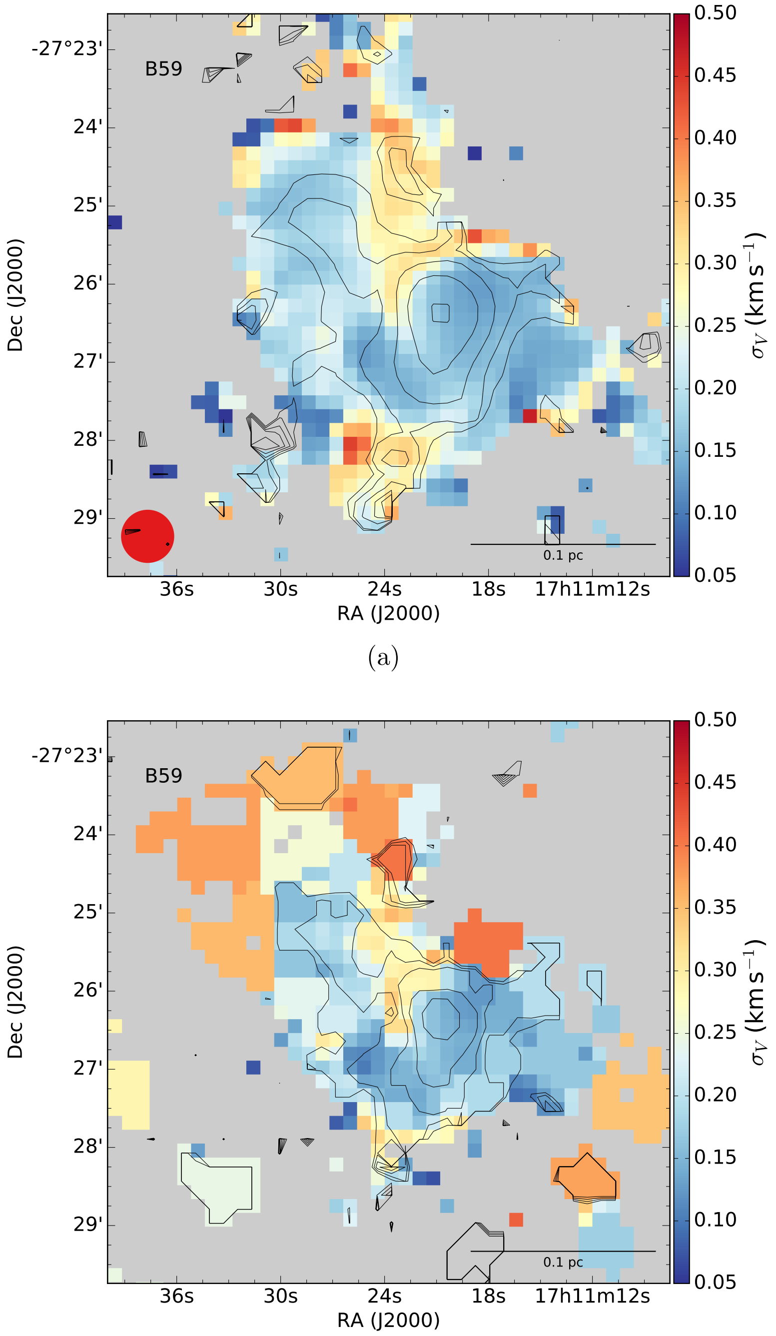

(a)

(b)

Figure 3.11: σ_V map obtained with smoothing (a) and Voronoi binning (b) methods. Colour scale is the same for both images. Contours are plot from $\log_{10}(\mathrm{N}(\mathrm{NH_3}))$ at levels [14.0, 14.2, 14.4, 14.6, 14.8].

Figure 3.11 shows the σ_V maps. Barnard 59 presents low velocity dispersion values in the range $\approx [0.05 - 0.50]\,\mathrm{km\,s^{-1}}$. Our spectral resolution of $FWHM = 0.07\,\mathrm{km\,s^{-1}}$ corresponds to $\sigma_V \approx 0.03\,\mathrm{km\,s^{-1}}$, and therefore obtained results are reliable also in their lower limit. The mean values of this parameter for the entire source are $\overline{\sigma}_V = 0.20\,\mathrm{km\,s^{-1}}$ (smoothing) and $\overline{\sigma}_V = 0.24\,\mathrm{km\,s^{-1}}$ (VB). The sound speed for an isothermal source with $T \approx 12\,K$, which is approximately the value found in B59, can be evaluated through:

$$C_S = \sqrt{\frac{k_B T}{\mu m_{\mathrm{H}}}} \approx 0.20\,km/s\ , \tag{3.21}$$

where μ is the mean molecular weight of the gas, set on the value $\mu = 2.33$, m_{H} the hydrogen mass and k_B the Boltzmann constant. We can therefore assert that motions in the source are mainly subsonic, or at most slightly supersonic. The coherent core, especially, is very quiescent, characterized by $\overline{\sigma}_V \approx 0.17\,\mathrm{km\,s^{-1}}$ for pixels with $\log_{10}(\mathrm{N(NH_3)}) > 14.4$.

3.3.6 Final comparison between the two methods

In all the parameter maps we have presented the two methods seem to produce consistent results as far as both values and structure are concerned. There are though some important differences. The Voronoi binning has the advantage of preserving the original angular resolution in the center of the cloud, where the emission is bright and the SNR high enough. Nevertheless, it produces misleading structures at the edges of the core because it averages up to $30 - 35$ pixels per bin. The smoothing method, on the contrary, allows to control much better the degradation of resolution across the map, with the price though to decrease it even when it would be unnecessary.

Our conclusion is that the Voronoi method is more suitable for a larger source, with an extended faint emission. In addition, especially when VB meta-pixels grow big enough, the resulting signal could in principle average spectra with different V_{lsr} or linewidth values, leading to wrong estimation of the velocity dispersion. In order to better investigate the reliability of this method in our source, we are planning to use deeper observations of $\mathrm{NH_3}$ (1,1) and (2,2) carried out with the GBT telescope. With these we will be able to observe a more extended ammonia emission, and to compare parameter maps derived from them to our binned images. We conclude that for B59 the smoothing method seems to produce more reliable results that will be used for the following analysis.

Chapter 4

Herschel observations and analysis

In this chapter I will present the Herschel Space Observatory. We have used its archive data to characterized the dust emission in Barnard 59. After a brief description of the observations, I will explain the methods used to analysed these data and the obtained results.

4.1 Herschel Space Observatory

Figure 4.1: An artistic impression of Herschel telescope orbiting in space [Credit: ESA].

The Herschel Space Observatory is an orbiting observatory developed by the European Space Agency (ESA) with the partnership of NASA, designed to work in the far infrared-mm waveband. Herschel is a Cassegrain telescope with a hyperbolic primary mirror of 3.5 m in diameter. It has been the largest infrared dedicated facility, with an improvement in angular resolution of about 6 with respect to other instruments such as the Spitzer telescope. It contains three different instruments, two for photometry and low/medium resolution spectroscopy and one for high resolution spectroscopy.

The Photodetector Array Camera and Spectrometer (PACS) works in the $[60 \sim 210]\,\mu$m wavelength range, with two bolometers for imaging photometry and two photoconductor arrays for line spectroscopy. SPIRE (SPectral and Photometric Imaging Receiver) has a three band photometer and a spectrometer with a spectral resolution $\lambda/\Delta\lambda$ of 20 to 1000 at $250\,\mu$m. The HIFI (Hetherodyne Instrument for the Far Infrared) instrument is a high resolution spectrometer with seven bands in the range $[157 \sim 625]\,\mu$m. It comprises two receivers, a wide band spectrometer and an high resolution one. Table 4.1 summarizes the main properties of the SPIRE photometer, which is the instrument used for the present work.

Table 4.1: Main features for the SPIRE photometer.

Band	short (PSW)	medium (PMW)	long (PLW)
Central λ	$250\,\mu$m	$350\,\mu$m	$500\,\mu$m
Ω_{beam}[1](arcsec^2)	467.62	808.10	1666.78
HPBW[1](arcsec)	20.31	26.71	38.35

[1] Beam size and half power beam width at $T = 10\,K$ and dust opacity index $\beta = 1.5$ (Ref. SPIRE Handbook).

Herschel was meant for multiple purposes, from the observation of Solar system bodies to the investigation of the very first phases in galaxy formation at high redshifts. In the context of star formation, besides, its data can unveil the properties of the coldest and darkest clouds in the Milky Way.

Herschel was launched in 2009 and after some months dedicated to tests and calibration procedures, it started to orbit around the second lagrangian point L2 of the Earth-Sun system. At the time of launch, its cryostat contained over 2000 liters of liquid helium, essential for the correct operation of all instruments: in fact, at these wavelengths detectors must be cooled down to very low temperature ($\approx 0.3\,K$), otherwise their thermal emission dominates observations. Due to the exhaustion of coolant supply, Herschel was fully deactivated in April 2013.

4.2 Observations

The data used to analyse the dust emission properties in the Pipe are taken from the Herschel Archive (Observational ID: 1342216013). They were observed during two periods in order to identify and remove transient objects such as asteroids. The instrument used is the SPIRE photometer with three spectral bands in the observing mode called Parallel Mode, which means that the three SPIRE photometers work simultaneously with PACS at the wavelengths 100 and 160 μm (however, we did not use PACS in our analysis since it is more sensitive to point-like sources than to extended emission). Data are collected through scanning, in a similar way to the OTF mode of the GBT (see Sec. 2.2): the telescope slews along parallel lines. Once one line is finished, the spacecraft is turned to the next one, scanned in the opposite direction. Since the Pipe is very extended, many individual scan maps were observed and then joined in a mosaic image. Herschel data products are classified in three levels of processing. We have selected the highest available (level 3) maps, which are already calibrated and mosaiced. All the data were calibrated with the standard Herschel Pipeline (calibration tree version: spire_cal_14_2, released in November 2015). Figure 4.2 shows the Herschel map at SPIRE medium wavelength.

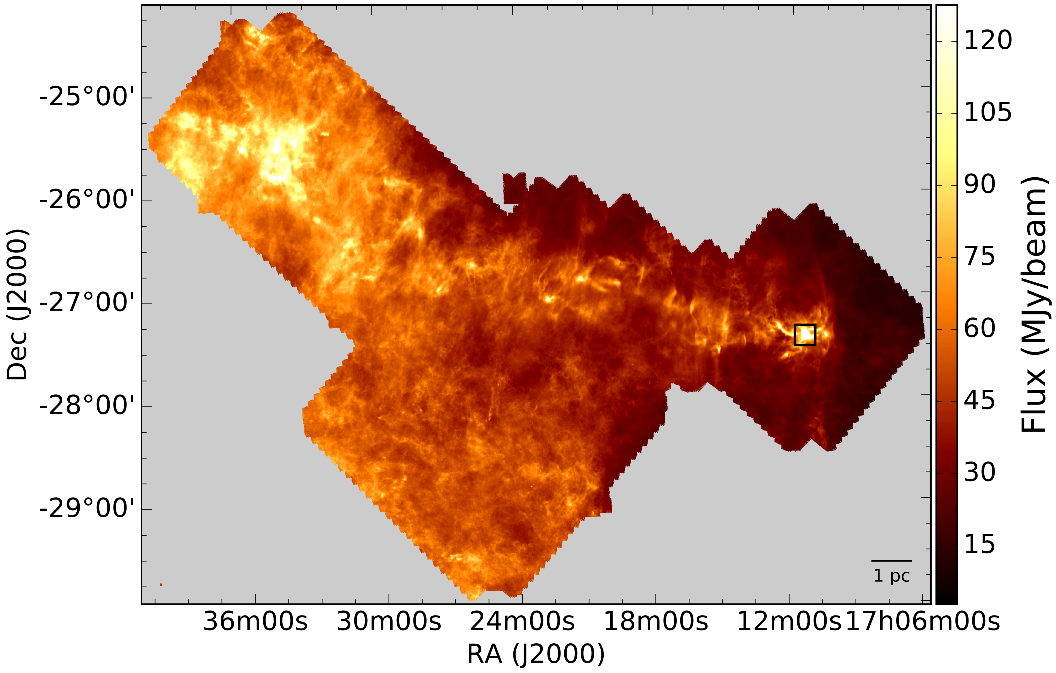

Figure 4.2: The Pipe Nebula as observed with the 350 μm band of SPIRE camera. The black box shows Barnard 59 position.

Since we are interested only in B59, we resize all the maps producing three sub-images centred in the studied core (R.A. $= 17^h11^m24.1^s$ and Dec $= 27°25'28''$ in J2000.0), with a total size of $800'' \times 800''$, which is roughly the same size of the GBT ammonia maps. Figure 4.3 shows the resulting map obtained at 350 μm.

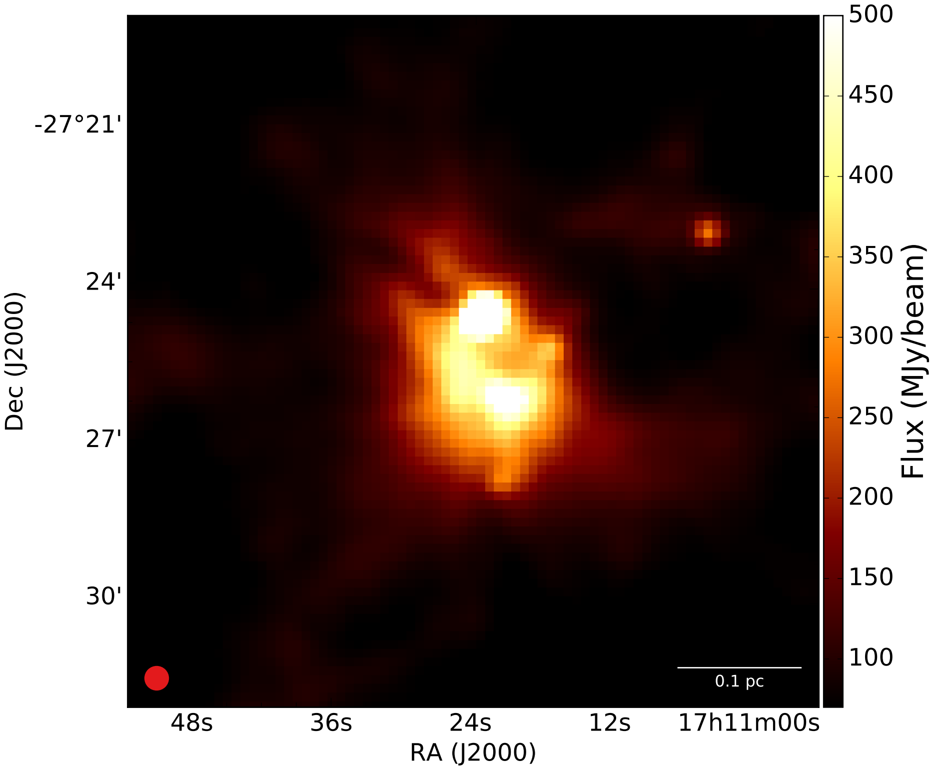

Figure 4.3: Zoom-in of the black box in Figure 4.1, showing Barnard 59 as seen by Herschel SPIRE instrument at 350 μm.

4.3 Dust emission fitting

The theoretical approach for processing infrared data described in the Introduction has been implemented through an IDL code kindly provided by Dr. Jorma Harju[1] (Hardegree-Ullman et al., 2013).

We set the dust opacity index $\beta = 1.5$, which seems suitable for star forming regions (Walker et al. 1990 and Mezger et al. 1990), and the dust opacity $\kappa_0 = 0.1\,\mathrm{cm}^2 g^{-1}$ (Hildebrand 1983, Beckwith et al. 1990). First of all, the script must

---

[1] University of Helsinki, Astronomy department. E-mail address: Jorma.Harju@astro.helsinki.fi.

take into account the different angular resolution of the three bands, and as a consequence the intermediate and short wavelength images are downgraded to the resolution of 500 μm. This procedure is analogous to the one described in 3.2.1: $\lambda = 250\,\mu$m and $\lambda = 350\,\mu$m maps are smoothed through convolution with a gaussian kernel with standard deviation

$$\theta_\lambda = \sqrt{\frac{\mathrm{HPBW}_{500}^2 - \mathrm{HPBW}_\lambda^2}{8\,\ln(2)}}\ , \tag{4.1}$$

which comes from Eq. (3.12) and from the relation between full width half maximum and σ (FWHM$= 2\sqrt{2\,\ln(2)}\,\sigma$).

Once the three sub-images have the same angular resolution of ≈ 38.4 arcsec, which is also similar to the one of the smoothed ammonia cubes, they become aligned with the PSW map as reference.

At this point, the code starts to fit data pixel by pixel. The fitting function is a modified black body emissivity at the three frequency, as previously described in the Introduction. There are two free parameters: dust temperature T_{dust} and the quantity

$$a = I_{250}\left(\frac{h\nu_{250}}{k_B T_{dust}}\right)^{-(3+\beta)}\left(\exp\left\{\frac{h\nu_{250}}{k_B T_{dust}}\right\} - 1\right)\ , \tag{4.2}$$

which is just the inversion of the relation between $B_{250}(T_{dust})$ and I_{250} (see the Introduction). Initially, the temperature is set on the value $T_{dust} = 15\,K$, from which an initial guess for a is derived. Then a non-linear least squares fit is performed recursively until the temperature change is smaller than $0.1\,K$. At each iteration, *colour corrections* are taken into account. These multiplicative factors are determined from the conversion of the broad-band signal collected by Herschel filters into a monochromatic intensity. In order to do this, the standard Herschel pipeline assumes a power-law spectrum for the source, which is not our case. The SPIRE handbook reports correction values at different temperatures (see Table 4.2). After each fitting procedure, colour corrections are evaluated interpolating the tabulated ones at the obtained T_{dust} and are applied to the intensity maps. These corrected data are a required input for the next fit.

Once the temperature map is evaluated,the optical depth at 250 μm is obtained at each pixel through:

$$\tau_{250} = \frac{B_{250}(T_{dust})}{I_{250}}\ , \tag{4.3}$$

where I_{250} is obtained from the best fit value of the parameter a. From this, the determination of a column density map is straightforward.

Table 4.2: Colour corrections for extended source with gray-body emission, at different T; $\beta = 1.5$. Ref. SPIRE Handbook

	K_{Ex}		
T (K)	PSW	PMW	PLW
3.0	0.5244	0.7756	0.8710
4.0	0.7441	0.9177	0.9903
5.0	0.8704	0.9808	1.0339
6.0	0.9414	1.0084	1.0479
7.0	0.9811	1.0196	1.0501
8.0	1.0031	1.0230	1.0475
9.0	1.0150	1.0226	1.0433
10.0	1.0208	1.0204	1.0385
15.0	1.0182	1.0049	1.0188
20.0	1.0064	0.9933	1.0070
25.0	0.9966	0.9856	0.9997
30.0	0.9894	0.9803	0.9948
35.0	0.9840	0.9766	0.9913
40.0	0.9800	0.9738	0.9887

4.3.1 Column density and temperature uncertainties

We evaluate the uncertainties on parameters derived through the fit with a Monte Carlo method, taking into account two main sources: flux calibration uncertainties in the spectral model for Neptune, the primary calibrator, and error maps produced by the Herschel pipeline itself. The latter concerns fluctuations in the detectors response when the same observation is carried out many times.

The fitting procedure is therefore repeated for $N = 1000$ times. From the second iteration on, a random noise ϵ_{rnd} is added to every map, pixel by pixel, according to the equation:

$$\epsilon_{rnd} = \mathrm{rnd}(0,1) \cdot 0.07 \cdot I_\lambda + \mathrm{rnd}(0,1) \cdot \epsilon_\lambda \, , \tag{4.4}$$

where $\mathrm{rnd}(0,1)$ is a random number between 0 and 1 taken from a gaussian distribution with mean value $\overline{x} = 0$ and unitary standard deviation, I_λ is the intensity signal value at the wavelength λ and ϵ_λ is the value from the associated error map just mentioned. Calibration uncertainties are 7% according to the SPIRE Handbook.

For both τ_{250} and T_{dust} the script generates a cube of maps with N layers: at each iteration, a new map is added in the following free layer. At the end of the procedure, the first map gives the searched result, while its uncertainties are obtained taking the standard deviation through all remaining layers. Uncertainties on other parameters are evaluated through standard error propagation. For example, for N(H_2) :

$$\mathrm{N}_{\mathrm{H}_2} = \frac{\tau_{250}}{\mu_{\mathrm{H}_2} m_H \kappa_{250}} \qquad \rightarrow \qquad \epsilon_{\mathrm{N}_{\mathrm{H}_2}} = \frac{\epsilon_{\tau_{250}}}{\mu_{\mathrm{H}_2} m_H \kappa_{250}} \,. \tag{4.5}$$

4.4 Results

We now present results obtained following the described procedure. Figure 4.4 shows the optical depth across the source. The emission is optically thin: this justify the choice of using this approximation mentioned in the Introduction (Eq. (28)). However τ_{250} tends to increase towards B59, indicating an increasing H_2 column density. The south-west part of the cloud, in particular, presents the highest values.

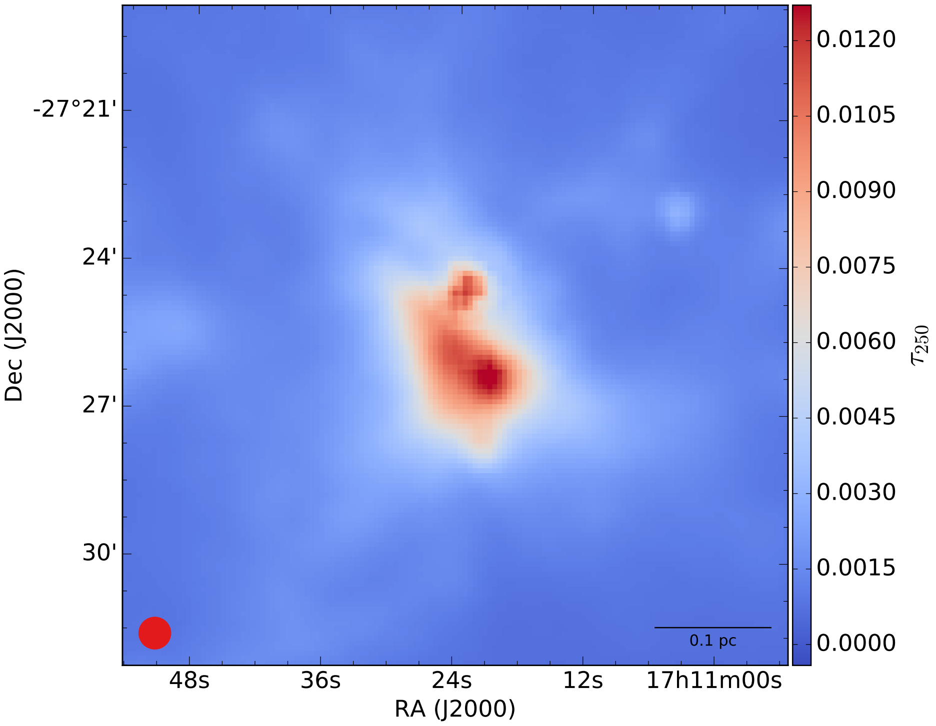

Figure 4.4: Optical depth map in Barnard 59 as obtained from Herschel data.

The obtained map for H_2 column density is shown in Figure 4.5. By definition, its structure is similar to the optical depth map. We can identify at least three different main clumps. The first one is the densest, and it is located in the south-west end of the core. The peak is found at position position R.A. = $17^h11^m20.91^s$, Dec = $-27°26'12.2''$ and has $\log_{10}(N(H_2)) = 22.48$. A second enhancement in column density appears towards north as an almost round condensation of about 30 arcsec in radius. Here the densest pixel, located at R.A. = $17^h11^m23.29^s$ and Dec = $-27°24'36.4''$, has $\log_{10}(N(H_2)) = 22.41$. The third peak is found far from the main cloud, at ≈ 320 arcsec toward the north-west direction. Here the density is generally lower, with a maximum value of $\log_{10}(N(H_2)) = 21.82$ at position R.A. = $17^h11^m04.10^s$ and Dec = $-27°22'55.3''$. Figure 4.5 shows also the condensations positions (black crosses), labelled with ordinal numbers. Table 4.3 summarizes the main features of the map, indicating also uncertainties on reported values as obtained with the Monte Carlo method.

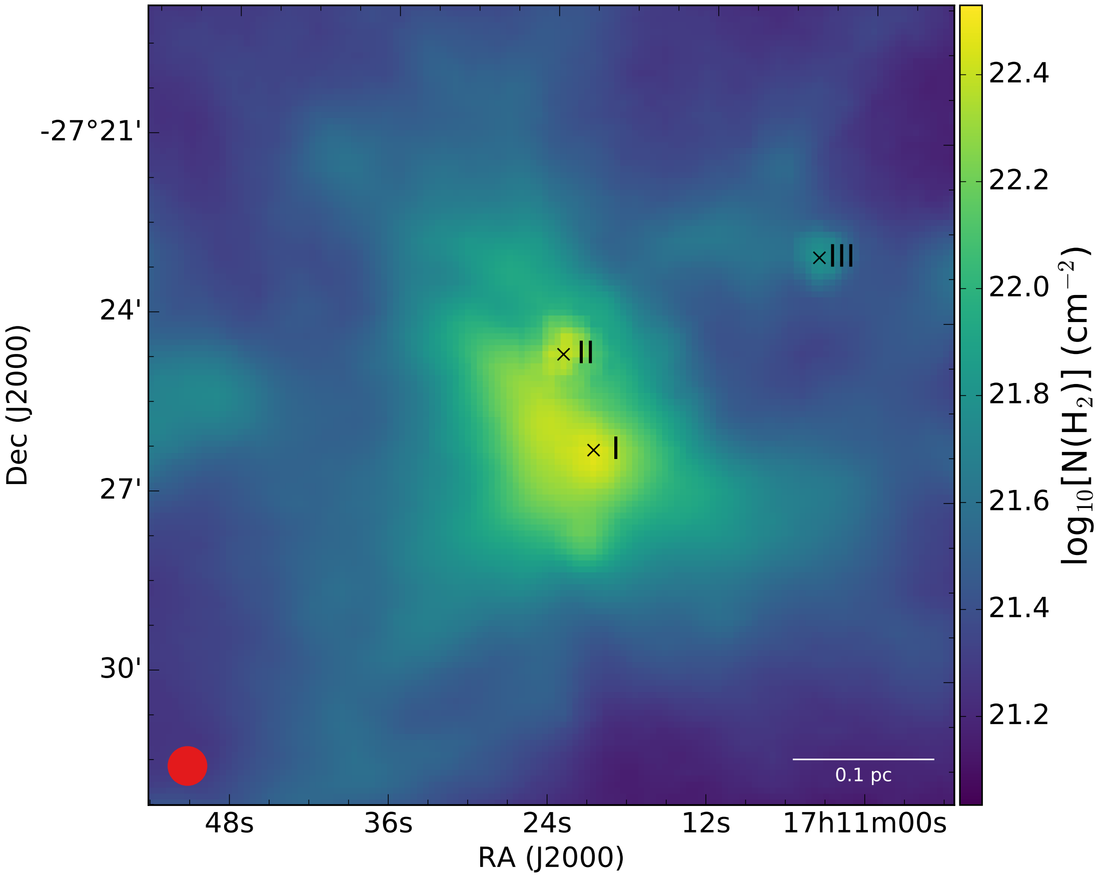

Figure 4.5: $N(H_2)$ map in Barnard 59 resulting from fitting SPIRE data. See text for labels explanation.

Table 4.3: Brief summary of main features found in the $N(H_2)$ map.

Clump N.[1]	Value ($\log_{10}(\mathrm{cm}^{-2})$)	Position [2]
I	22.48 ± 0.06	$17^h11^m20.91^s$, $-27°26'12.2''$
II	22.41 ± 0.07	$17^h11^m23.29^s$, $-27°24'36.4''$
III	21.82 ± 0.07	$17^h11^m04.10^s$, $-27°22'55.3''$

[1] Structure number following the order used in the text and in Figure 4.5.

[2] Right Ascension and Declination in J2000.0

Figure 4.6 shows the distribution of dust temperature. The coldest temperature

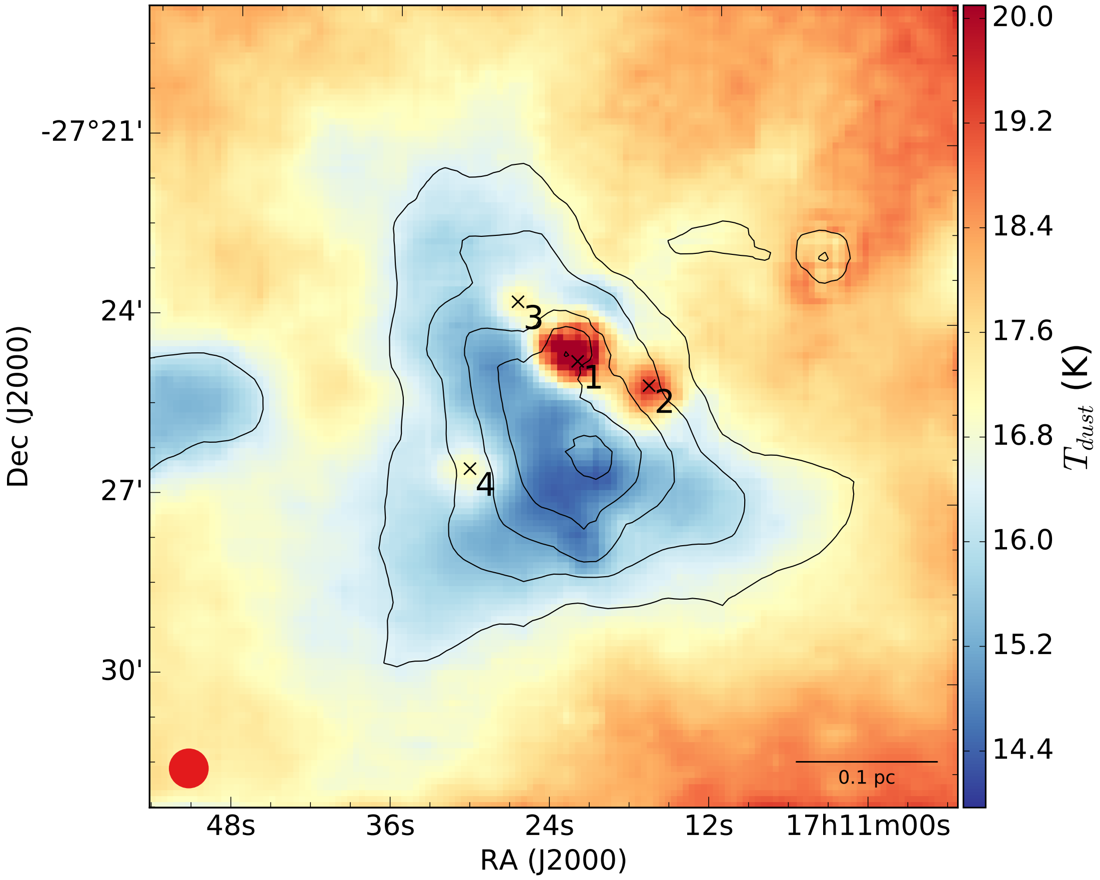

Figure 4.6: T_{dust} map in Barnard 59 resulting from fitting SPIRE data. Crosses show position of the peak temperature for each hot condensation discussed in the text, together with a numerical label (see also Table 4.4). Contours from $N(H_2)$ map at levels [21.6, 21.8, 22.0,22.2, 22.4].

registered is $T_{dust} = (14.3 \pm 0.5)\,K$ at the position R.A. $= 17^h11^m20.93^s$, Dec $= -27°26'41.9''$. This point is at a distance $R \approx 30$ arcsec from the densest pixel, therefore within a beam size: the densest part of the core is also the coldest.

In the image it is possible to identify a number of “hot condensations”, i.e. approximately round regions where temperatures are higher than in the surroundings. This is the case, for example, of the column density peak at the north of the cold core. Here the absolute highest temperature is found, with a value $T_{dust} = 21.8\,K$ at R.A. $= 17^h11^m22.40^s$, Dec $= -27°24'42.0''$. The temperature enhancement is localized in an almost round region of ≈ 30 arcsec of radius, as also the column density data show. At least three other temperature peaks are visible: the first one located at the south-west side, with a maximum temperature $T_{dust} = 19.6\,K$ at R.A. $= 17^h11^m17.00^s$, Dec $= -27°25'05.4''$, and with a radius of about 25 arcsec. Towards the north-east direction another temperature increment is found, peaking at R.A. $= 17^h11^m26.96^s$, Dec $= -27°23'43.4''$ with $T_{dust} = 17.3\,K$. The last structure is located at R.A. $= 17^h11^m30.38^s$, Dec $= -27°26'31.3''$. Temperature is lower than in the other condensations, with a peak value of $T_{dust} = 17.0\,K$, but it still stands out from the colder surrounding core. Table 4.4 presents the main features for the hot condensations. Numerical labels corresponds to the ones shown in Figure 4.6.

Table 4.4: Brief summary of condensation features found in T_{dust} map.

Condensation N.[1]	Peak T_{dust} (K)	Position[2]	$\overline{T}_{dust}{}^{3}(K)$
1	21.8 ± 1.5	$17^h11^m22.40^s$, $-27°24'42.0''$	19.7^4
2	19.5 ± 1.1	$17^h11^m17.00^s$, $-27°25'05.4''$	18.7
3	17.3 ± 0.8	$17^h11^m26.96^s$, $-27°23'43.4''$	16.9
4	17.0 ± 0.8	$17^h11^m30.38^s$, $-27°26'31.3''$	16.7

[1] Condensation ID with reference to Figure 4.6.

[2] Position of the peak in Right Ascension and Declination (J2000.0).

[3] Averaged temperature in a circular region with 25 arcsec radius around the peak, unless otherwise noted.

[4] The average is computed on a circular region with radius of 30 arcsec centred in R.A. $= 17^h11^m22.4^s$, Dec $= -27°24'33.9''$.

Chapter 5

Young stellar object feedback

The formation of stars is one of the most researched fields of observational astrophysics, but still several of its aspects are not well understood, concerning especially its very early stages. However, the general picture is known: in giant molecular clouds, cold and quiescent dense cores are formed by contraction, since thermal pressure is not enough to halt the gravitational collapse of large amounts of mass. Their collapse leads to an increase in temperature and density in the very central part, where a new star is forming. Due to angular momentum conservation, accretion flows towards the protostar tend to flatten and form a circumstellar disk that later on will host new planets. Part of the infalling material is launched in the form of outflows and jets in the direction perpendicular to the disk plane, carrying out energy and mass. As the protostar continues its evolution, the envelope in which it was embedded and the gas and dust present in the disk are cleared out, and eventually a pre-main sequence star is born. On the other hand, many processes involved are yet to be completely understood and several questions still need an answer, such as what actually triggers the initial collapse or what is the exact physics of outflows and the role of other agents such as magnetic fields in the dynamical evolution of clouds and cores. In this chapter we will investigate how the initial phases of star formation affect the ambient gas of the parent core.

5.1 Young stellar objects in B59

Young stellar objects (YSOs) represent the first stages of low mass star formation. The central compact object emits radiation that is reprocessed by the dusty envelope and the disk at longer wavelengths, typically from NIR to mm range. As a result, the spectral energy distribution (SED) presents an infrared excess, which is the main feature used to identify these sources. According to SED shape, YSOs are usually classified in four main spectral classes, reflecting different evolutionary stages. The parameter used is the slope of the distribution at infrared wavelength, defined as:

$$\alpha_{IR} = \frac{d \log(\lambda F_\lambda)}{d \log(\lambda)} \tag{5.1}$$

α_{IR} is usually computed between $2.2\,\mu m$ and $10\,\mu m$ (Stahler & Palla, 2005). The classes are usually defined as follows, even though each author may use different values :

- Class 0: sources so embedded that can be seen only in FIR or mm emission and are not detectable at $\lambda < 20\,\mu$m;
- Class I: $\alpha_{IR} > 0$. These objects are still deeply embedded, and show a disk and often outflows;
- Class II: $-1.5 < \alpha_{IR} < 0$. As time passes by, part of the dusty envelope is dissipated. The SED now peaks at optical wavelengths, and therefore its NIR slope is negative. The disk, though, is still optically thick;
- Class III: $\alpha_{IR} < -1.5$. All the envelope is removed as well as gas and dust in the disk. SEDs almost do not show infrared excess any more.

The change of the SED can be understood taking into account the Wien's law, which relates the peak wavelength of a planckian to the temperature of the emitting black-body:

$$\lambda_{peak} T = 0.029\,\mathrm{m}K \tag{5.2}$$

In the early stages, the emission is dominated by the cold ($T \approx 10\,K$) envelope: $\lambda_{peak} \approx 100\,\mu$m. After the latter is cleared, the SED peak moves to optical wavelengths due to the higher temperature, since the protostar is dominating the emission.

Figure 5.1 shows model SEDs for a low mass object at three evolutionary stages, which are defined according to the envelope accretion rate $\dot{M}_{env}$ and the disk mass M_{disk}, both in unit of the central object mass M_*. Stage I objects have $\dot{M}_{env}/M_* > 10^{-6}\,yr^{-1}$. For stage II, $\dot{M}_{env}/M_* < 10^{-6}\,yr^{-1}$ and $M_{disk}/M_* > 10^{-6}\,yr^{-1}$. Stage III is defined according to $\dot{M}_{env}/M_* < 10^{-6}\,yr^{-1}$ and $M_{disk}/M_* < 10^{-6}\,yr^{-1}$. For each one, ten curves are presented according to ten different inclination angles with respect to the line of sight, from pole-on viewing (upper SED) to edge-on (lower SED). Different colours stand for different energy contribution. One can see that as the protostar evolves, the envelope emission decreases and the influence of viewing angle become negligible.

Brooke et al. (2007) combined SPITZER data from the Legacy Science project "Core to Disks" (c2d) with 2MASS[1] archive data in order to identify YSOs in

---

[1] The 2 Micron All-Sky Survey is a photometric survey lead with base-ground telescopes that observed the whole celestial vault in the bands J ($1.25\,\mu$m), H ($1.65\,\mu$m) and K$_s$ ($2.17\,\mu$m).

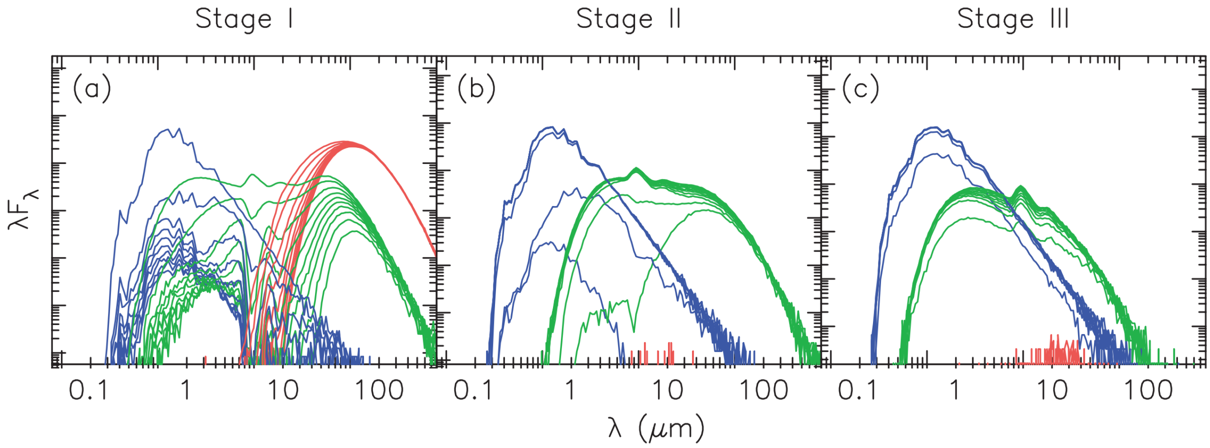

Figure 5.1: Model SEDs for a $0.2\,M_\odot$ object at stage I, II and III and for 10 different viewing angles. The contribution of the star is shown in blue, the one of the envelope in red and green is for the disk [Ref: Robitaille et al. (2006)].

a region of 170 arcmin^2 containing B59. The c2d maps were observed with both IRAC and MIPS camera, obtaining photometric data at 3.6, 4.5, 5.8, 8.0, 24 and 70 μm. YSOs are identified through infrared excess relative to photospheric colours. These authors performed a careful selection in order to exclude external contamination such as galaxies and background stars. Eventually they found 20 sources in the field, classified as follows: $\alpha_{IR} \geq 0.3$ is a class I object; $-0.3 \leq \alpha_{IR} < 0.3$ is a *flat* (I/II) source and $\alpha_{IR} < -0.3$ a class II. Due to their selection criteria, no class III was found in the sample. Class 0 is defined according to prescription of Andre et al. (2000): $T_{bol} < 70\,K$ and $L_{sub-mm}/L_{bol} > 0.5\%$. The selected sources are described in Table 5.1.

In the sample, source B11 has been widely studied (Riaz et al. 2009, Hara et al. 2013). Using both continuum and line observations, these authors proposed that this object is driving probably rotating outflows and is surrounded by a Keplerian disk. Duarte-Cabral et al. (2012) used ^{12}CO to investigate the large scale kinematics and identified B09 and B10 two other outflows-driving sources. Furthermore, they also studied the cloud dynamics with ^{13}CO and C^{18}O, and their V_{lsr} and σ_V maps are very similar to ours.

Figure 5.2 shows our N(NH_3) map with labelled circles showing YSOs positions. Sources that fall in the region covered by ammonia data are B08, B09, B10, B11, B12, B14 and B15. These seven objects are also part of the sample studied by Forbrich et al. (2009), who investigate the YSO population in B59 using only MIPS data at 24 at 70 μm. For all of them (except for B12 which is too close to the brighter B11) the classification is consistent with Brooke et al. (2007). No objects are found at the peak of NH_3 column density, but it is interesting to notice that B11 is located significantly close to the density enhancement in the northern part of the cloud described in Sec. 3.3.1.

Table 5.1: Identified young stellar objects in B59 region according to Brooke et al. (2007).

ID	2MASS name	R.A. [1]	Dec [1]	Class
B01	J17110392-2722551	$17^h11^m03.91^s$	$-27^\circ22'55.2''$	Flat
B02	J17110411-2722593	$17^h11^m04.12^s$	$-27^\circ22'59.3''$	II
B03	J17111182-2726547	$17^h11^m11.82^s$	$-27^\circ26'55.0''$	II
B04	J17111445-2726543	$17^h11^m14.45^s$	$-27^\circ26'54.4''$	II
B05	J17111626-2720287	$17^h11^m16.27^s$	$-27^\circ20'28.8''$	II
B06	J17111631-2725144	$17^h11^m16.32^s$	$-27^\circ25'14.6''$	II
B07	J171117261-2725081	$17^h11^m17.28^s$	$-27^\circ25'08.2''$	I
B08	J17111827-2725491	$17^h11^m18.13^s$	$-27^\circ25'49.3''$	I
B09	J17112153-27274171	$17^h11^m21.50^s$	$-27^\circ27'42.3''$	Flat
B10	-	$17^h11^m22.10^s$	$-27^\circ26'02.0''$	I
B11	J17112317-2724315	$17^h11^m23.18^s$	$-27^\circ24'31.5''$	0/I
B12	J17112508-2724425	$17^h11^m25.08^s$	$-27^\circ24'42.7''$	Flat
B13	J17112701-2723485	$17^h11^m26.95^s$	$-27^\circ23'48.4''$	II
B14	J171127291-2725283	$17^h11^m27.06^s$	$-27^\circ25'29.5''$	II
B15	J17112942-2725367	$17^h11^m29.31^s$	$-27^\circ25'36.3''$	II
B16	J17113036-2726292	$17^h11^m30.29^s$	$-27^\circ26'29.3''$	II
B17	J17114099-2718368	$17^h11^m40.99^s$	$-27^\circ18'03.0''$	II
B18	J17114182-2725477	$17^h11^m41.73^s$	$-27^\circ25'50.3''$	II
B19	J17114315-2730584	$17^h11^m43.16^s$	$-27^\circ30'58.6''$	II
B20	J17120020-2720180	$17^h12^m00.20^s$	$-27^\circ20'18.1''$	II

[1] Right Ascension and Declination in J2000.0 .

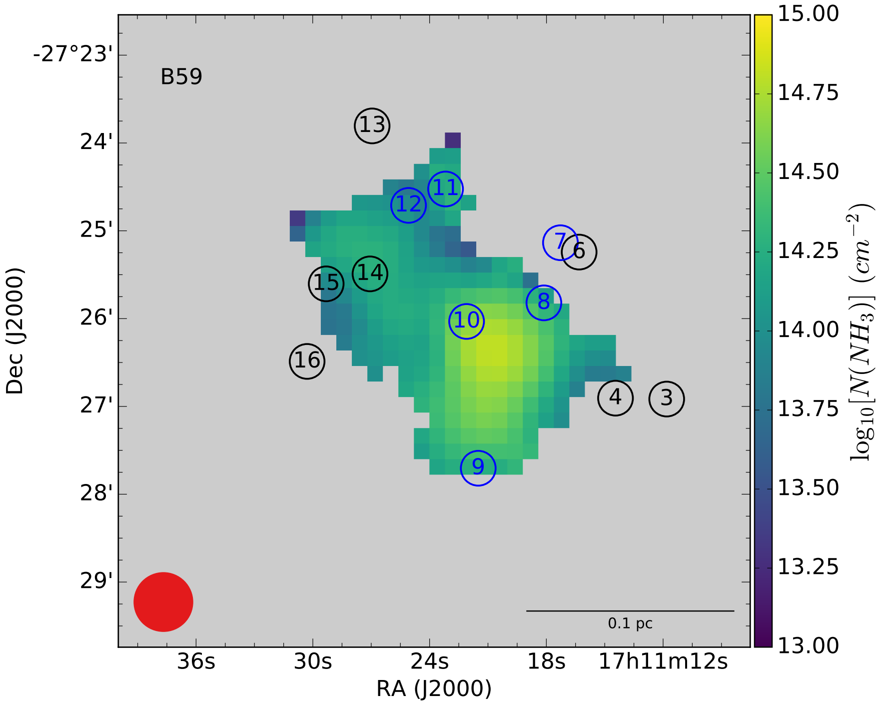

Figure 5.2: Positions of YSOs from Brooke et al. (2007) on top of N(NH_3) map. From this image on, different colours stand for different evolutionary stages: blue for young (class 0, I and flat) sources, while black for class II objects.

5.2 Feedback of the YSOs on the core

The first stages of star formation are a very active phase: energy is emitted through radiation and outflows, which also carry out angular momentum and mass. All this activity can affect the surrounding environment, for example heating the gas or producing non-thermal (turbulent) gas motions. These processes cause the increase of velocity dispersion around the source. Furthermore, if the YSO is not too deeply embedded (class higher than Class 0) and the optical depth is low enough that observations are not dominated by the cold envelope, temperature maps should present increasing values in the source proximity. Our data allow us to look for this kind of effects in Barnard 59.

Figure 5.3 shows the distribution of young stellar objects with respect to the T_K map. The increase of gas temperature towards north corresponds to positions of two very young sources, B11 and B12, the first of which is driving outflows, as previously noted. Figure 5.4 shows the velocity dispersion σ_V map with the YSOs distribution on top: the hottest part of the cloud present also broader line-width, especially around B11.

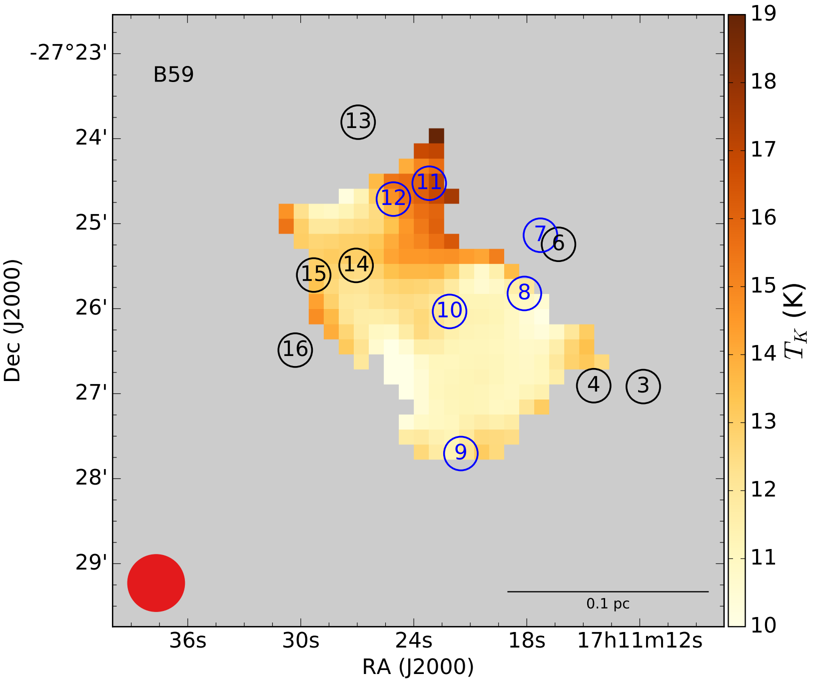

Figure 5.3: T_K map with YSOs positions shown.

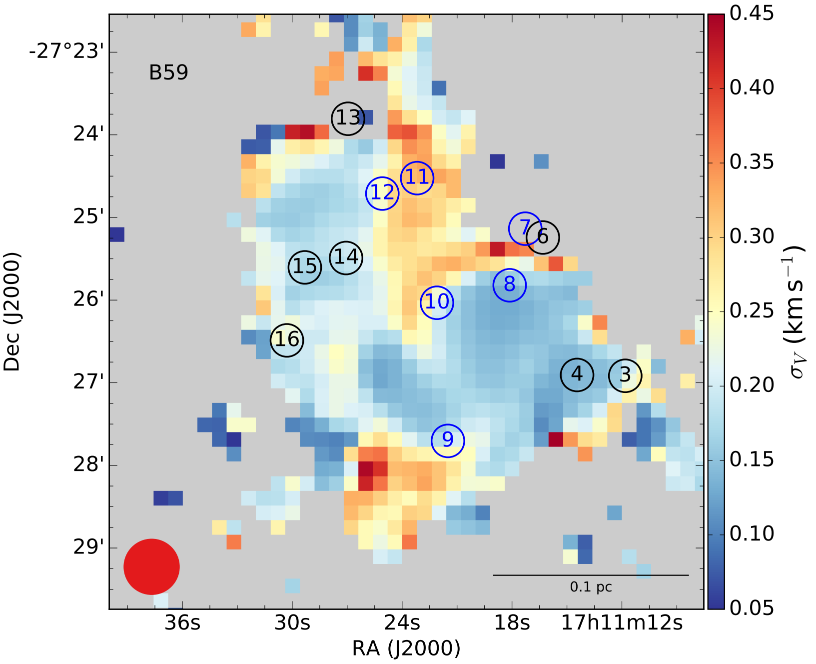

Figure 5.4: σ_V map with overlying YSOs positions.

5.2.1 Thermal and non-thermal motions

In order to further investigate potential protostellar feedback in the area, we compute the thermal σ_T and non-thermal velocity σ_{NT} dispersion components. The first one is defined by:

$$\sigma_T = \sqrt{\frac{k_B T_K}{\mu_{\mathrm{NH_3}} m_H}} \,, \tag{5.3}$$

where m_{H} is the hydrogen atom mass and $\mu_{\mathrm{NH_3}}$ is ammonia molecular weight in atomic units, equal to 17.03. Since these two quantities are independent of each other, they add in quadrature. One can obtain σ_{NT} following:

$$\sigma_V^2 = \sigma_T^2 + \sigma_{NT}^2 \qquad \rightarrow \qquad \sigma_{NT} = \sqrt{\sigma_V^2 - \sigma_T^2} \,. \tag{5.4}$$

σ_{NT} describes gas motions that are not due to thermal effects, such as turbulence. The resulting map is shown in Figure 5.5: in the coherent core, the most dense and cold part of the cloud, the non-thermal velocity dispersion is small, with a mean value $\overline{\sigma}_{NT} = 0.16\,\mathrm{km\,s^{-1}}$ for pixels with $\log_{10}(\mathrm{N(NH_3)}) > 14.4$. In addition, the

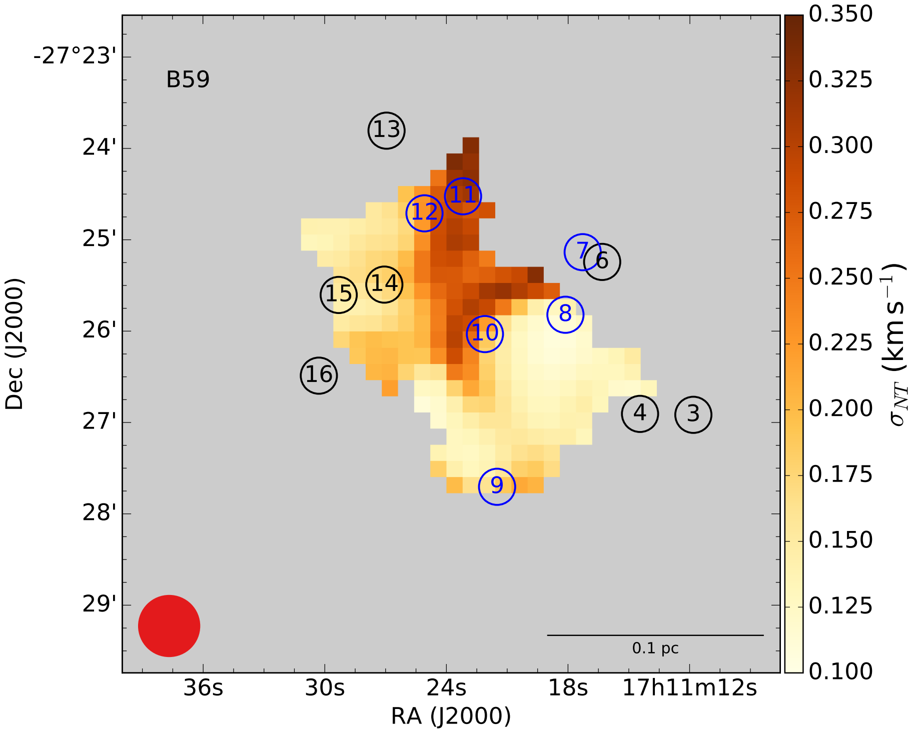

Figure 5.5: σ_{NT} map as computed through Eq. (5.4).

less dense north-eastern clump has a low σ_{NT}, even though a bit higher than in the coherent core: here $\overline{\sigma}_{NT} = 0.18\,\mathrm{km\,s^{-1}}$ for $\log_{10}(\mathrm{N(NH_3)}) > 14.1$. On the other hand, non-thermal motions tend to increase up to values of $0.25 - 0.35\,\mathrm{km\,s^{-1}}$ towards B11 and B12. It is important to understand whether the motions in the core are subsonic or supersonic, because it is known that while molecular clouds have supersonic velocity dispersion, dense cores generally appear subsonic environments (Caselli et al., 2002). From T_K we can compute the speed of sound pixel by pixel, using Eq. (3.21). From this we can derive the ratio σ_{NT}/C_S that discerns between the two regimes. Results are presented in Figure 5.6.

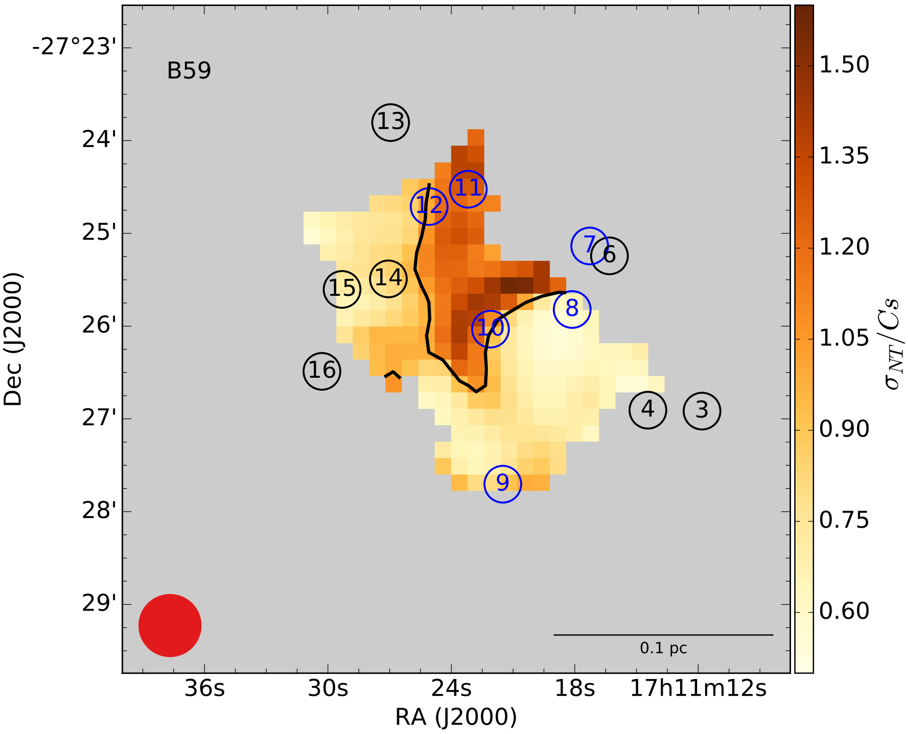

Figure 5.6: σ_{NT}/C_S across Barnard 59. The black line shows where ratio equals 1., i.e. the transition between subsonic and supersonic motions.

The obtained map has an interesting structure. The densest core and the north-eastern region are subsonic, with σ_{NT}/C_S down to 0.55. This justifies why we use the term coherent to describe the former. As found by other works (Foster et al. 2009, Pineda et al. 2010), the transition to supersonic motions appears quite sharp, and then the ratio increases reaching the peak value of 1.57. An interesting pattern is found: class II sources, at least in projection, appear to be associated with quiescent motions. On the other hand, less evolved objects seem to be located in regions of supersonic motions or on the transition edge. In Figure 5.4, since the determination of σ_V does not depend on the detection of the NH_3 (2,2) line, one can appreciate a larger scale structure. Here this trend is somehow confirmed: while B04, B14 and B15 are located in very quiescent areas, B08, B09, B10 and B12 are close to regions where σ_V is increasing. B11, besides, is completely surrounded by broad lines.

5.2.2 Scatter plots

So far we have just described qualitatively the maps: in order to quantify our arguments we produce scatter plots to inspect the correlation between the distinct quantities. The first one shows the velocity dispersion versus maximum main beam temperature T_{peak} at each pixel (Figure 5.7), where we also indicate the curve for $\sigma_V = C_S = 0.20\,\mathrm{km\,s^{-1}}$ for a temperature of $\approx 10\,K$, close to the mean value that our results show.

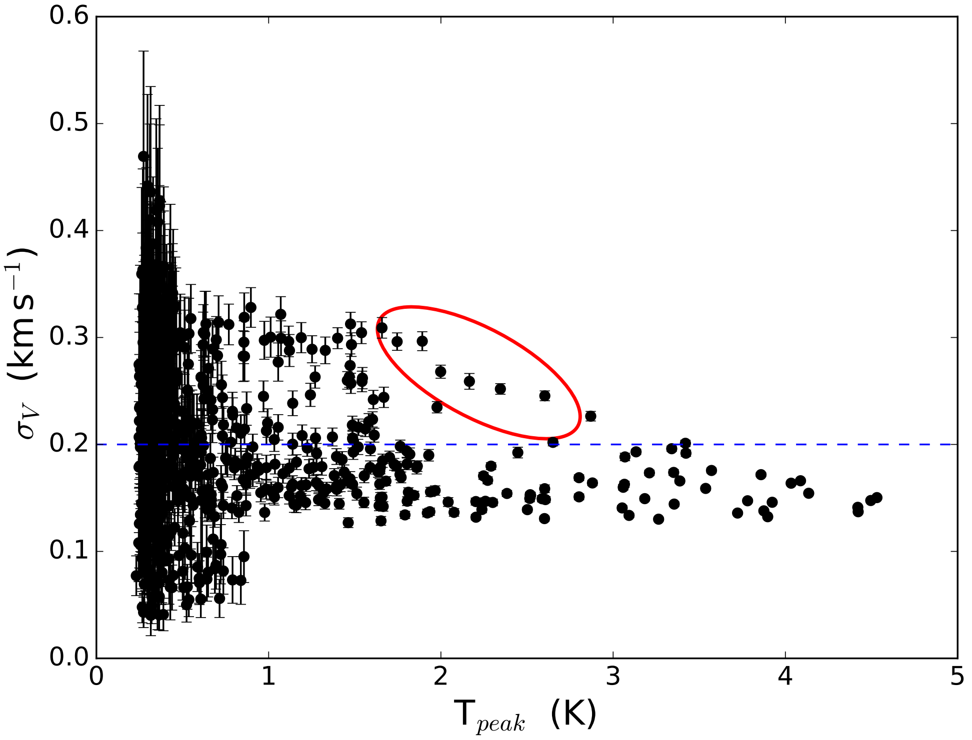

Figure 5.7: σ_V versus T_{peak} for the entire core. The blue dashed line represents the isothermal speed of sound at $\approx 10\,K$. See text for the red ellipse meaning.

The overall aspect indicates that pixels with the highest column density, characterized by high peak temperature, have low velocity dispersion, smaller than the average sound speed, confirming what we have already pointed out: the coherent core is also very quiescent. On the contrary, points with $\sigma_V > 0.25\mathrm{km\,s^{-1}}$ are found at low peak temperature, with typical values $T_{peak} < 2\,K$. Their spectra are noisier, and therefore error bars are larger. There are however some pixels (red circled in Figure 5.7) in an intermediate situation, with not so low signal ($T_{peak} \gtrsim 1.7\,K$) and at the same time high velocity dispersion ($\sigma_V \gtrsim 0.23\,\mathrm{km\,s^{-1}}$): their position is shown in Figure 5.8. These points represent the transition from subsonic to supersonic regime.

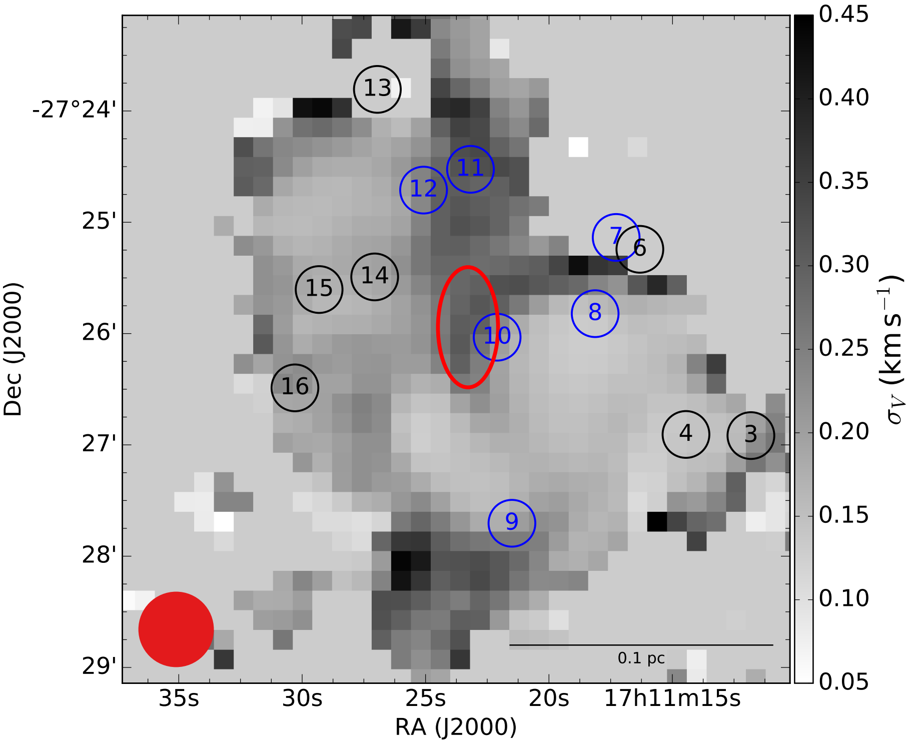

Figure 5.8: Close up view of σ_V map, highlighting with a red ellipse the position of pixels underlined in the previous figure, with both high T_{peak} and σ_V . Black and blue circles mark YSOs positions.

To further investigate the influence of YSOs, we present the same scatter plot for all YSOs, enhancing those points closer than 40″ to each one. Resulting graphs can be divided in three main categories that will be now described. For each one, we present just one scatter plot, showing the complete set in Appendix A.

Figure 5.9 presents results for B11. One can see that in its surroundings the velocity dispersion is the broadest of the entire cloud. The lowest value found is $\sigma_V = 0.20\,\mathrm{km\,s^{-1}}$, while the mean is $\overline{\sigma}_V = 0.30\,\mathrm{km\,s^{-1}}$. This is the only YSO that shows this kind of behaviour.

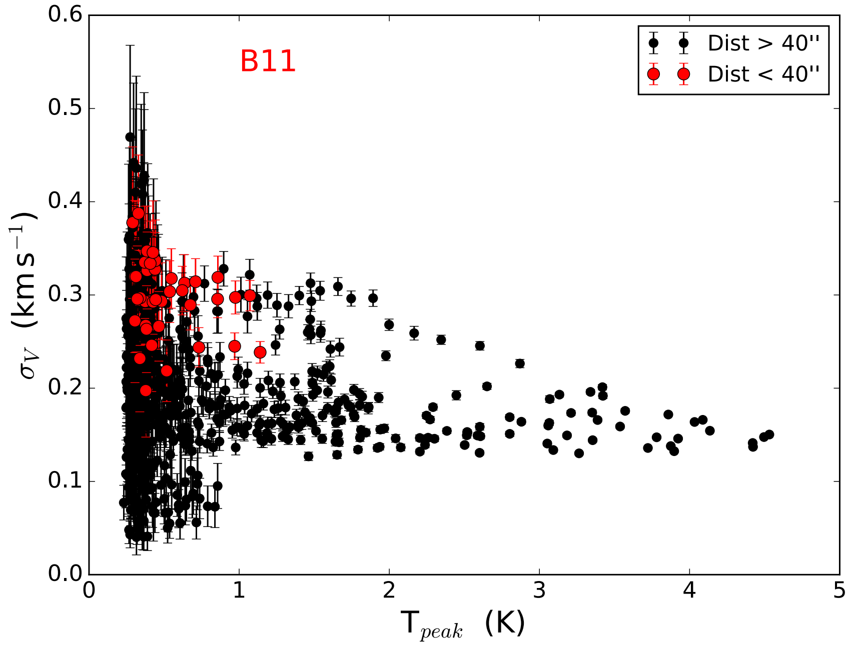

Figure 5.9: σ_V versus T_{peak} for B11. Red points are closer than 40″ to the source.

B04, B14 and B15 scatter plots are similar to the one shown in Figure 5.10.

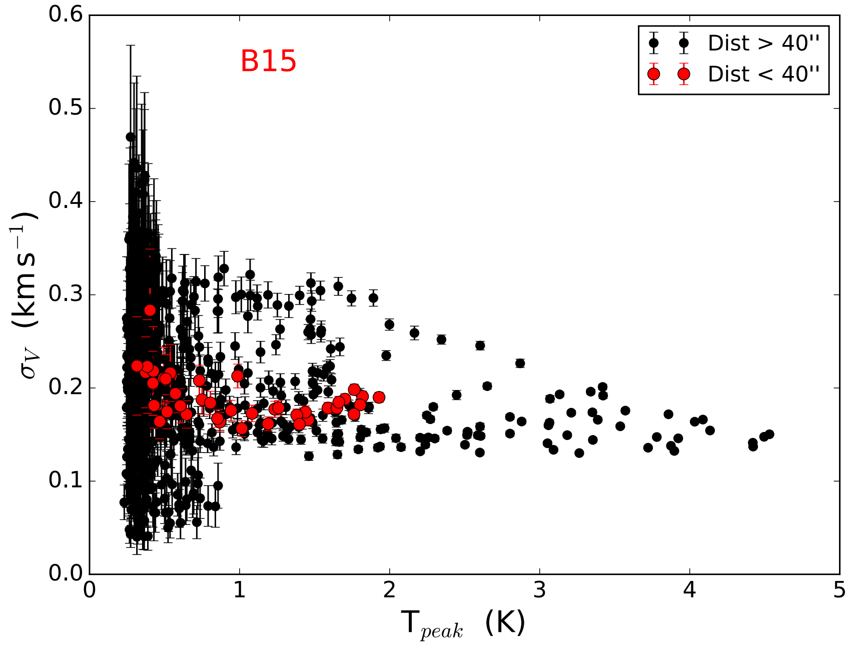

Figure 5.10: σ_V versus T_{peak} for B15. Red points are closer than 40″ to the source.

Close to these sources line are narrower, with mean values never exceeding 0.20 km s^{-1}, and with a small dispersion across the mean value. According to these features, we ascribe also B16 to this category. It is interesting to notice that all these sources are class II objects.

A number of sources exhibit a behaviour intermediate between the two distributions previously described. This is the case of B08, B09, B10 and B12: we show the scatter plot for the first one in Figure 5.11. The molecular line emission toward these objects have both broad lines at low T_{peak} values and narrow ones (below the C_S limit), at brighter pixels, leading to high dispersion of data. Except for B08, mean σ_V values within the selected distance are higher than 0.20 km s^{-1} . All objects belonging to this category are young sources, usually class I or at most I/II. In Table 5.2 we summarize the main features concerning velocity dispersion map nearby each YSO.

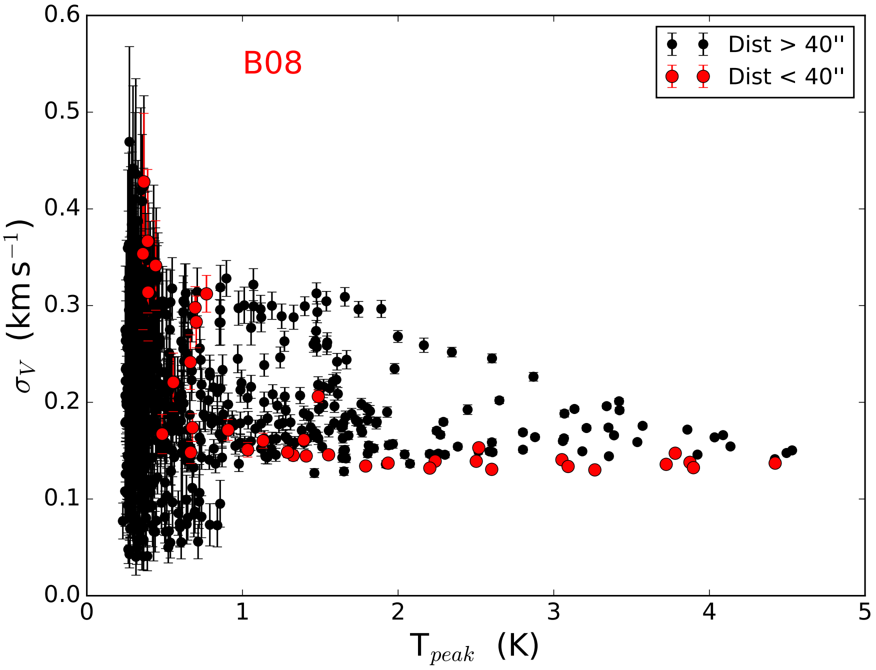

Figure 5.11: σ_V versus T_{peak} for B08. Red points are closer than 40″ to the source.

We next analyse our data substituting σ_V with the ratio σ_{NT}/C_S, which indicates whether gas motions are subsonic or supersonic. As one can see in Figure 5.6, sources B04 and B16 are not covered by this map because we do not have a reliable estimation of T_K at their positions. They are therefore excluded from the study. The remaining scatter plots confirm the trimodal picture previously described, as we are going to show.

Table 5.2: σ_V properties in a circular region of $40''$ in radius around each source. All data are expressed in km s^{-1} .

ID	Class	$\overline{\sigma}_V$	σ_V^{min}	σ_V^{max}	Dispersion[1]
B04	II	0.17	0.12	0.30	0.04
B08	I	0.19	0.13	0.43	0.08
B09	Flat	0.22	0.15	0.34	0.06
B10	I	0.23	0.14	0.33	0.06
B11	0/I	0.30	0.20	0.39	0.04
B12	Flat	0.24	0.16	0.33	0.06
B14	II	0.19	0.16	0.26	0.03
B15	II	0.19	0.16	0.28	0.02
B16	II	0.20	0.11	0.31	0.04

[1] Standard deviation of the data.

B11 plot is shown in Figure 5.12. Within error bars, all the pixels in its proximity are above the transition line between supersonic and subsonic motions.

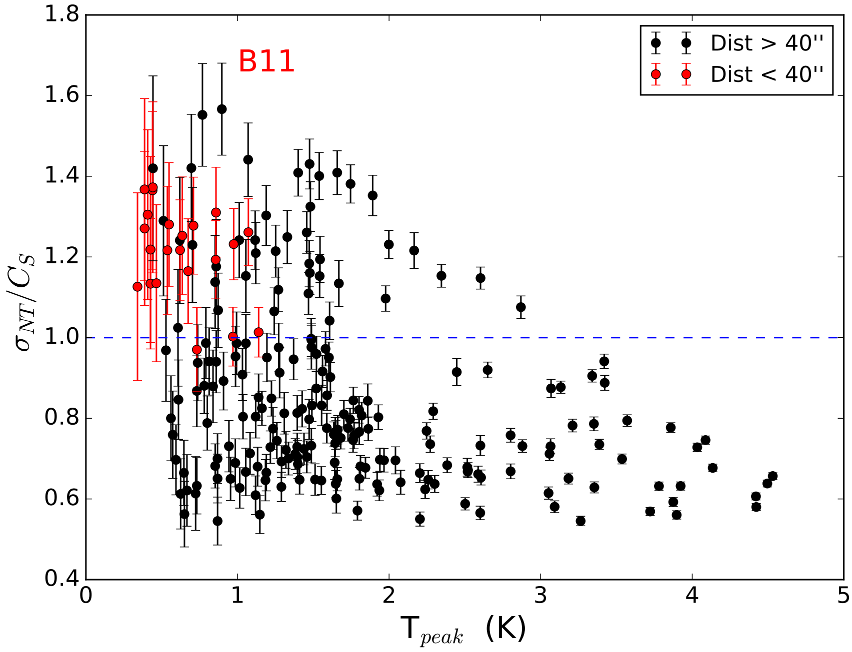

Figure 5.12: σ_{NT}/C_S versus T_{peak} for B11. Red points are closer than $40''$ to the source. Dashed blue lines marks transition between sub- and supersonic motions.

The mean value for the ratio computed over red points is $\langle \sigma_{NT}/C_S \rangle = 1.21$, with a peak value of 1.37. This source is located in the most turbulent part of the cloud.

Figure 5.13 is representative for sources B14 and B15. Gas motions are mainly (for B14) or even exclusively (for B15) subsonic. The average ratio is found far below 1.0 level (see also Table 5.3).

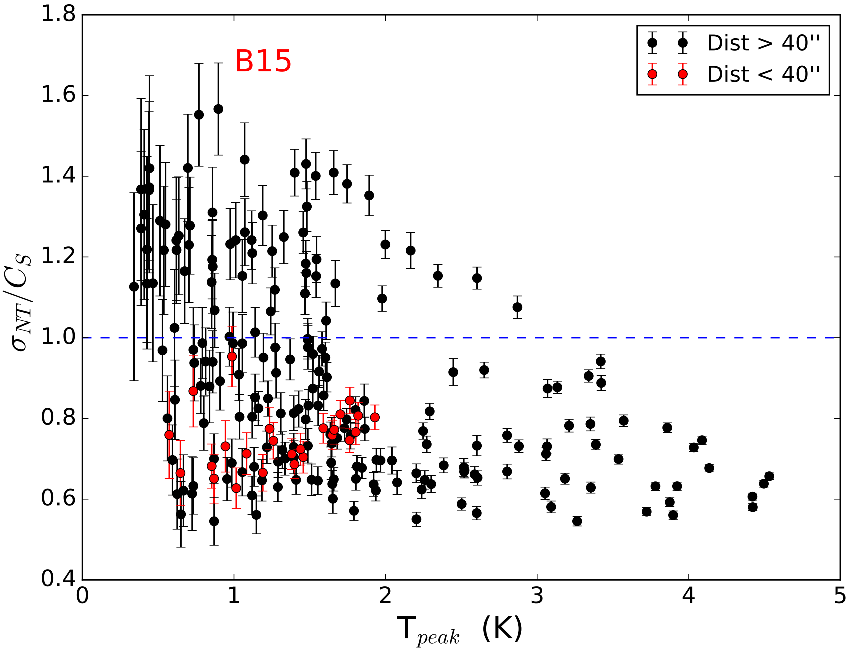

Figure 5.13: σ_{NT}/C_S versus T_{peak} for B15. Red points are closer than $40''$ to the source. Dashed blue lines marks transition between sub- and supersonic motions.

B10 and B12, as one can see from Figure 5.14, present an intermediate situation, as also the previous set of scatter plots showed. This is due to their position, which is close to the edge of subsonic core (see Figure 5.6). As a consequence, in their surroundings there are both subsonic and supersonic pixels, with a wide spread across the ratio mean value that however is > 1.0.

B08 and B09 seem to be peculiar cases. The first has the largest dispersion for the ratio, from very low values ($\sigma_{NT}/C_S|_{min} = 0.55$) to large ones ($\sigma_{NT}/C_S|_{max} = 1.55$). Most of the points, though, are characterized by subsonic motions. B09, on the other hand, seems to be located in a quiescent part of the cloud, totally subsonic. A warning must be raised concerning these two YSOs, though, due to their position: looking again at Figure 5.6, one can see that they are located on the edge of our map coverage. This means that averages are computed on a small number of points that, moreover, are not uniformly distributed around the sources. Taking into account these factors, we avoid drawing strong conclusions about them. Table 5.3 displays results from each scatter plot analysis.

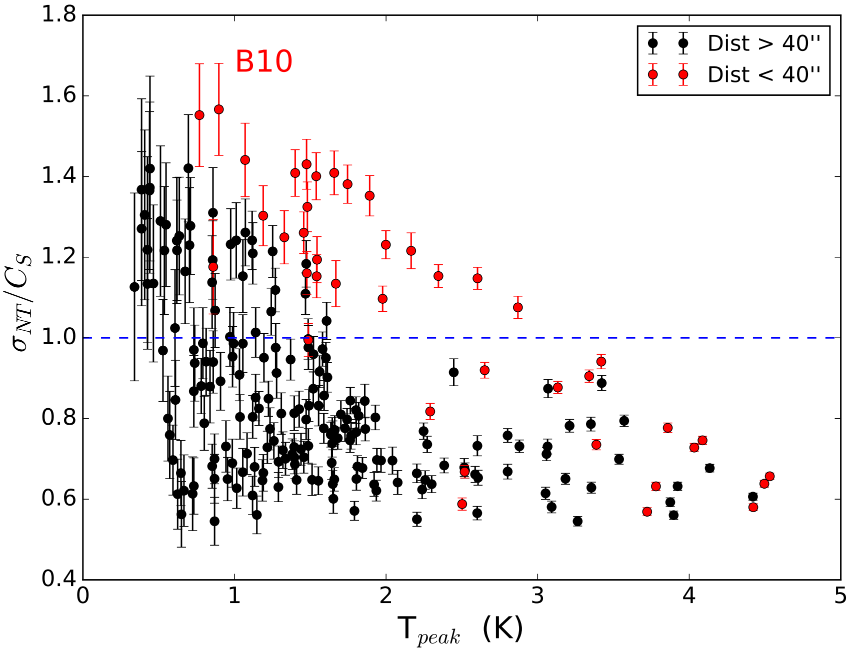

Figure 5.14: σ_{NT}/C_S versus T_{peak} for B10. Red points are closer than 40″ to the source. Dashed blue lines marks transition between sub- and supersonic motions.

Table 5.3: σ_{NT}/C_S features in a circular region of 40″ in radius around each source.

ID	Class	$\langle\sigma_{NT}/C_S\rangle$	$\sigma_{NT}/C_S\rvert_{min}$	$\sigma_{NT}/C_S\rvert_{max}$	Dispersion[1]
B08	I	0.75	0.55	1.55	0.30
B09	Flat	0.78	0.64	0.99	0.10
B10	I	1.06	0.57	1.57	0.30
B11	0/I	1.21	0.97	1.37	0.11
B12	Flat	1.06	0.76	1.37	0.20
B14	II	0.84	0.65	1.12	0.12
B15	II	0.75	0.65	0.95	0.07

[1] Standard deviation of the data.

5.2.3 Core dynamical state

In order to investigate the dynamical state of Barnard 59, we make use of the virial theorem, which briefly asserts that a gravitational system is in equilibrium if its kinetic energy K and potential energy U satisfy:

$$2T + U = 0 \; . \tag{5.5}$$

The *virial ratio* (Bertoldi & McKee, 1992), defined as:

$$\alpha_{vir} = \frac{2K}{|U|} \tag{5.6}$$

is therefore an indicator of the state of the system: if $\alpha_{vir} \gg 1$, the kinetic term is dominant and the structure, if not expanding, is confined by external pressure, while if $\alpha_{vir} \lesssim 1$ the system is said to be gravitationally bound. In this last case, however, one cannot conclude that the system is collapsing, since other energetic terms not included in Eq. (5.5) may become significant and balance the collapsing term. One example is the magnetic field.

Proceeding in the calculation requires an estimation for K and U. The former can be expressed through:

$$K = \frac{1}{2} M \widetilde{\sigma}^2 \; , \tag{5.7}$$

where M is the system mass and $\widetilde{\sigma}$ is its velocity dispersion. This is not σ_V we have used so far, since it involves just a minor component of the gas, ammonia. On the contrary, we are interested in the most abundant molecule in cold clouds, H_2. Its total line width can be derived from the knowledge of the gas temperature and the NH_3 total velocity dispersion σ_V . In fact, if we assume that the non-thermal component is the same for both lines, we have:

$$\sigma^2_{\mathrm{H_2}} - \sigma^2_{T,\mathrm{H_2}} = \sigma^2_{NT,\mathrm{H_2}} = \sigma^2_{NT,\mathrm{NH_3}} = \sigma^2_V - \sigma^2_{T,\mathrm{NH_3}} \; . \tag{5.8}$$

Then we can calculate pixel by pixel:

$$\sigma^2_{\mathrm{H_2}} = \sigma^2_V - \frac{k_B T_K}{\mu_{\mathrm{NH_3}} m_{\mathrm{H}}} + \frac{k_B T_K}{\mu_{\mathrm{H_2}} m_{\mathrm{H}}} \; . \tag{5.9}$$

Here $\mu_{\mathrm{NH_3}}$ has already been defined, while $\mu_{\mathrm{H_2}}$ is the H_2 molecular weight in atomic units, equal to 2.02. The resulting map is shown in Figure 5.15. The minimum value found in the source is $\sigma_{\mathrm{H_2}} = 0.22\,\mathrm{km\,s^{-1}}$, the maximum $\sigma_{\mathrm{H_2}} = 0.44\,\mathrm{km\,s^{-1}}$ and the mean one is $\overline{\sigma}_{\mathrm{H_2}} = 0.30\,\mathrm{km\,s^{-1}}$. We express the associated uncertainty as the standard deviation on the data. Our result is then $\overline{\sigma}_{\mathrm{H_2}} = (0.30 \pm 0.05)\,\mathrm{km\,s^{-1}}$. Eventually, taking into account that observed data give just one dimensional

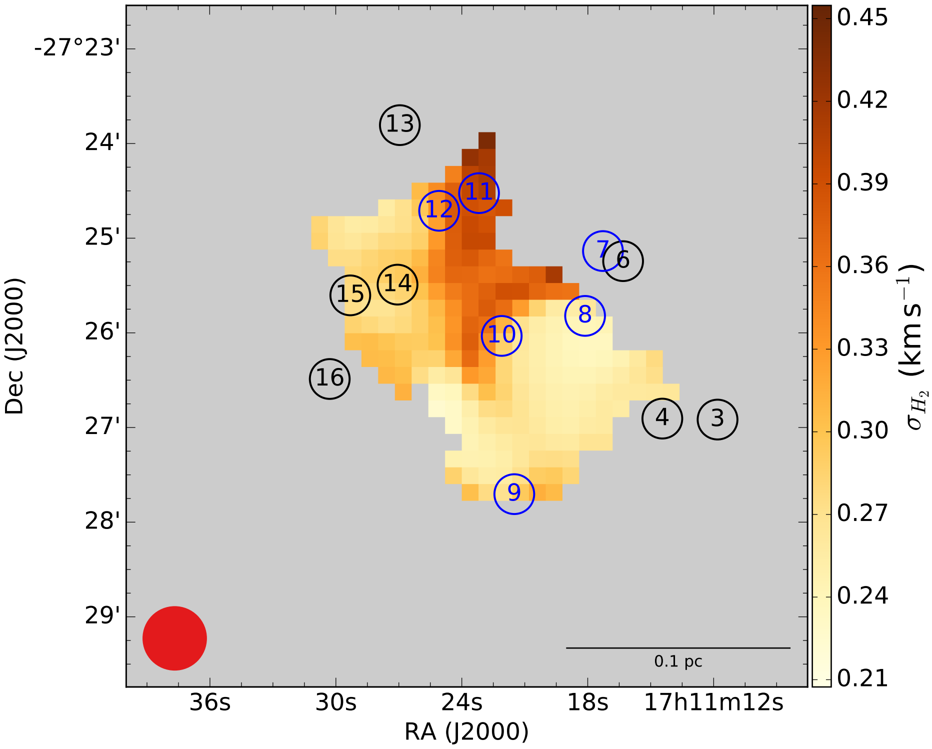

Figure 5.15: σ_{H_2} map in B59, with the YSOs positions shown.

velocity dispersion, while in Eq. (5.7) the 3D value is needed, we assume an isotropic distribution and find that $\widetilde{\sigma} = \sqrt{3}\,\sigma_{\mathrm{H}_2}$.

The gravitational term depends strongly on the system shape and density profile. Since we have no estimation for these parameters, we assume a simple uniform sphere with radius R and mass M as model. Then

$$U = -\frac{3}{5}\frac{GM^2}{R} \; . \tag{5.10}$$

We estimate the source mass from unpublished dust emission data at 870 μm observed with the APEX telescope, shown in Figure 5.16. The equation reads:

$$M_{dust} = \frac{D^2 S_\nu}{B_\nu(T_{dust})k_\nu} \; , \tag{5.11}$$

where:

- D is the source distance ($D = (145 \pm 16)$ pc from Alves & Franco (2007));
- S_ν is the total flux at 870 μm above 5σ level: $S_\nu = (128 \pm 13)\,Jy$. The uncertainty is calculated adding in quadrature two terms: the first one is

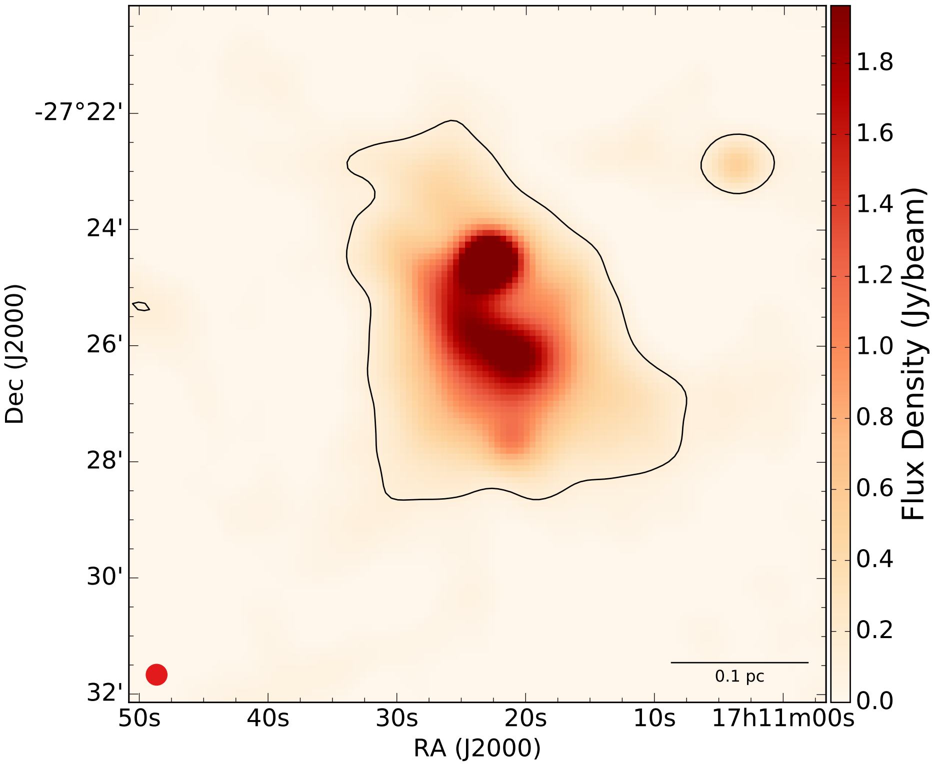

Figure 5.16: APEX/LABOCA map of B59, PI: Alvaro Hacar. The black contour shows the 5σ level used for the total flux computation.

$\sigma\sqrt{N_{tot}/\Omega_{pxl}}$, where σ is the rms level of the map, N_{tot} is the number of pixels involved in the integration and Ω_{pxl} is the beam size in pixels. The second term is the calibration uncertainty ($10\% S_\nu$);

- $B_\nu(T_{dust})$ is the planckian function at the dust temperature. We assume $T_{dust} = 15\,K$, which is the typical value for dense cores and it is consistent with the mean value found in our source with Herschel data;

- κ_ν is the dust opacity at the given frequency, that has been estimated thorough interpolation of tabulated values from Ossenkopf & Henning (1994) for thin icy mantles and gas density $n = 10^6\text{cm}^{-3}$. The obtained value is $\kappa_\nu = 1.89\,\text{cm}^2\,\text{g}^{-1}$.

We associate uncertainty with standard error propagation. Using a dust-to-gas ratio of 100, the total mass found is $M = (23 \pm 6)\,M_\odot$. This is quite in agreement with literature, which presents values of $20 - 30\,M_\odot$ (Duarte-Cabral et al. 2012, Román-Zúñiga et al. 2009, Rathborne et al. 2009).

The last quantity needed in Eq. (5.10) is the source linear size R: for this we calculate the radius of a circular region with the same area of that one used for the flux calculation in (5.11), using the distance D to transform the angular size into the physical one. The result is $R = (0.123 \pm 0.14)\,\mathrm{pc}$. Inserting Eq. (5.10) and (5.7) in (5.6), one gets:

$$\alpha_{vir} = \frac{5\widetilde{\sigma}^2 R}{3MG} = \frac{5\sigma_{\mathrm{H}_2}^2 R}{MG} = 0.56 \pm 0.24\ . \tag{5.12}$$

Since we know the H_2 velocity dispersion pixel by pixel, we can compute a map for this parameter, which is shown in Figure 5.17. It is interesting to notice that α_{vir} is < 1.0 almost in the entire core, except for a few points towards B11 position, due most likely to the outflows. Computing the average and the standard deviation on the map we obtain $\alpha_{vir} = 0.56 \pm 0.20$, perfectly in agreement with the previous result. Barnard 59 appears to be gravitationally bounded.

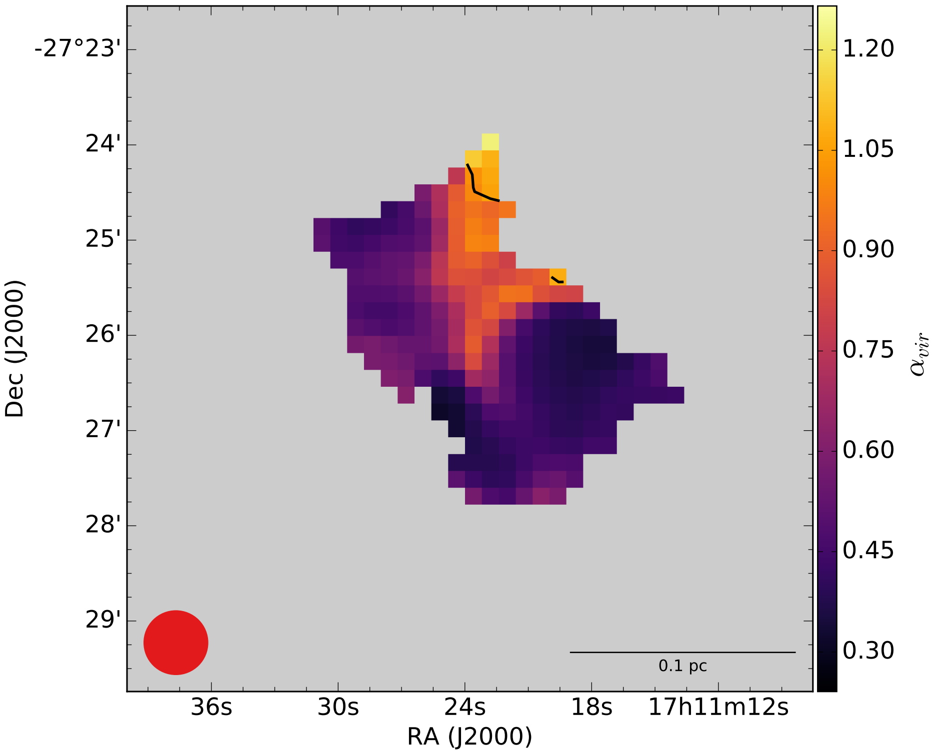

Figure 5.17: The map of α_{vir} in Barnard 59. The black curve marks where the parameter equals 1.

5.3 Results

The analysis carried out so far allows us to draw some conclusions about the effects of the protostellar cluster on Barnard 50 core. For B11 we find high temperature values and supersonic motions. Since this YSOs is known to power energetic outflows (Duarte-Cabral et al. 2012, Hara et al. 2013), we confirms that this source is actually embedded in the parent cloud and that it is heating and injecting turbulence in the gas. On the other hand, more evolved sources such as B04, B14 and B15 show no signs of influence on their surroundings: most probably they are foreground or background sources. We have a propensity for the first choice, based on Brooke et al. (2007): they compare extinction from background stars to the one obtained dereddening each source SED to the standard T Tauri model. Results show that A_V values from the former method are always larger than those from the latter, meaning that probably sources are in front of the cloud. Finally, it is hard to say something conclusive about the other sources. B10 and B12 present some hints of protostellar feedback on the gas, even though the latter is so close to B11 that higher spatial resolution is needed to disentangle their activity: the projected distance is $31''$, below the smoothed beam. B08, B09 and B16 are at the edges of our data coverage: a deeper mapping would allow to fully investigate also these sources.

Our study about α_{vir} indicates that even though protostellar activity is affecting the cloud, its feedback is merely local: the core is still gravitationally bound. On the other hand, we see no sign of further fragmentation or ongoing collapsing. Outflows injecting energy, as previously said, can sustain a turbulence level which prevent the core from collapse, but also other mechanisms could be involved, such as magnetic fields. New studies about polarization in the source will better clarify this point.

Chapter 6

Comparison between gas and dust

In this chapter I will make a comparison between gas and dust features as shown by the ammonia and Herschel data, respectively, using results obtained in Ch. 3 and 4. First I will focus on the relation between NH_3 and H_2 column density, in order to verify the common opinion according to which ammonia is a good tracer of the cold and dense gas. This study allows also to compute the ammonia fractional abundance, for which we will use a more refined method than just calculating the ratio between the two molecular densities. Then I will present a comparison between temperature maps, marking differences in their structure and values and trying to give an explanation for them.

6.1 NH_3 and H_2 column density

It is generally believed that ammonia is a tracer of cold gas (Ho & Townes, 1983). In order compare the gas and dust temperature distribution in Barnard 59, we show in Figure 6.1 the map obtained with Herschel data and $N(NH_3)$ contours.

Ammonia emission is less extended than continuum emission seen by Herschel, since the former trace cold and dense regions due to its critical density: $n_{cr} \approx 10^{3-4} \mathrm{cm}^{-3}$. However, at high column densities there seems to be a correlation between the two quantities. The area around B11 is interesting: here $N(H_2)$ values are quite high, with an average value of $\langle \log_{10}(N(H_2)) \rangle = 22.3$. In the coherent core, $N(NH_3)$ values corresponding to this level are higher than 14.4 in logarithmic scale. Around B11, instead, the highest value found is $\log_{10}(N(NH_3)) = 14.30$: ammonia is somehow depleted in this part of the cloud. We think this is due to chemical effects. It is known that at about $T_{dust} \approx 20\,K$ CO starts to evaporate from dust grain and its return to the gas phase affects heavily the nitrogen chemistry, halting the formation of NH_3 precursors(Charnley & Rodgers 2002, Rodgers & Charnley 2008). In the same region around B11, our maps present average values of $\overline{T}_K = 16.0\,K$ and $\overline{T}_{dust} = 20.0\,K$. We conclude that this can be the cause for the recorded lack of ammonia.

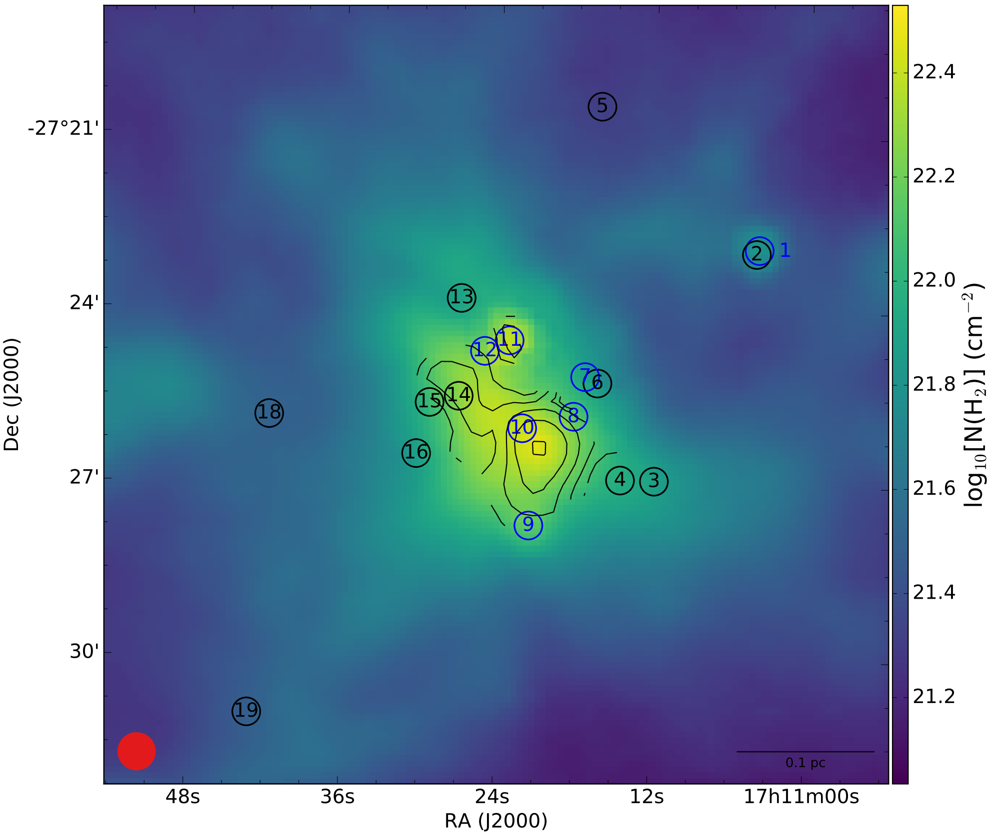

Figure 6.1: $N(H_2)$ map with overlying ammonia column density contours (levels: [14.0, 14.2, 14.4, 14.6, 14.8] in logarithmic scale). YSOs positions are shown as well.

In order to study the relation between the two column density tracers, we produce scatter plots as shown in Figure 6.2: on one axis we plot $N(NH_3)$ values and on the other $N(H_2)$ for all those positions where the former is available. Red points come from the coherent core only, selected through $\log_{10}(N(NH_3)) > 14.3$. A positive correlation between the two tracers is clear, especially for the points at high densities. A linear fit can better quantify this relation, and we will proceed with this approach.

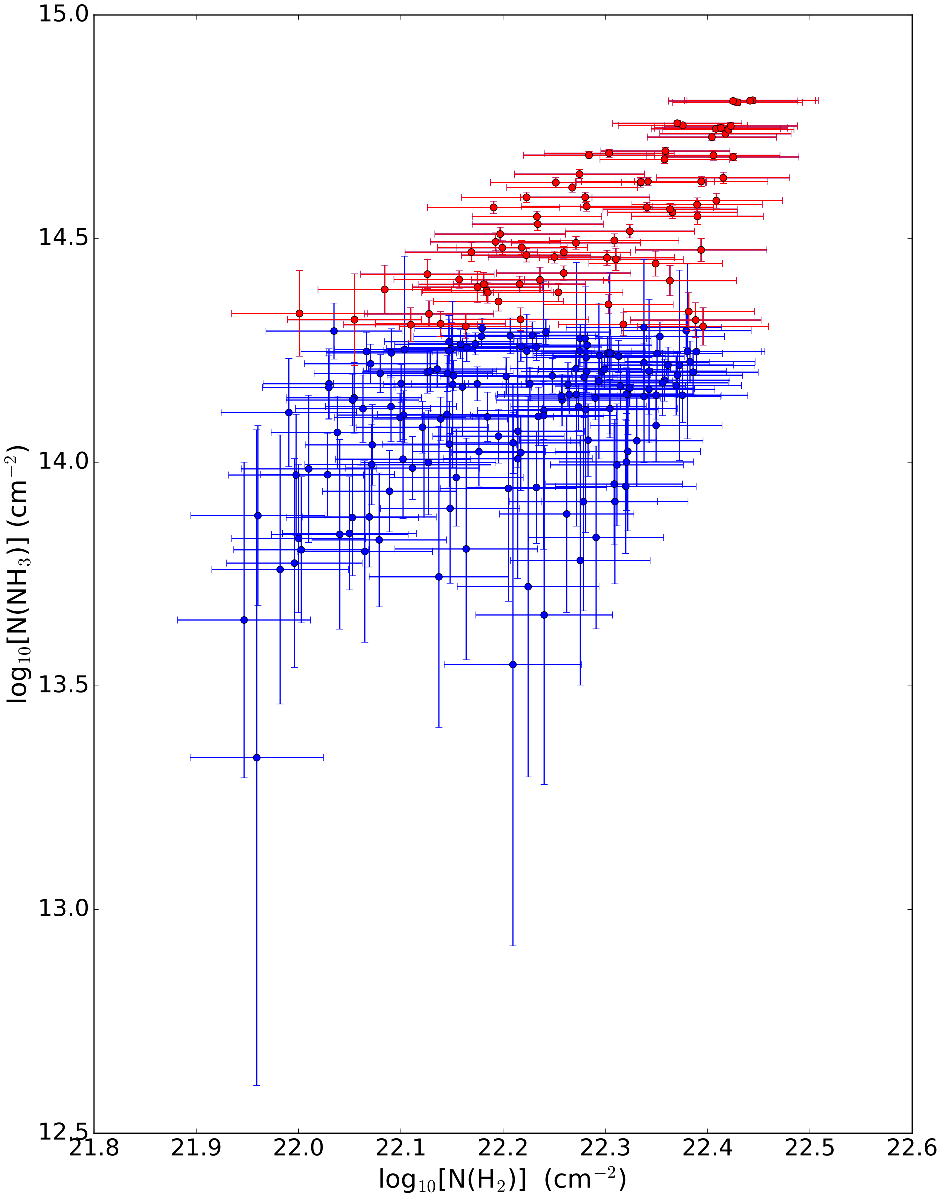

Figure 6.2: Scatter plot of NH_3 column density versus $N(H_2)$ in logarithmic scale. Red points are representative of the pixels in the coherent core.

The relation between ammonia and H_2 column density is not linear if the two variables are in logarithmic scale, due to the presence of an offset between them (see the approach shown in Pineda et al. (2008) and Goodman et al. (2009)):

$$\mathrm{N(NH_3)} = \mathrm{X(NH_3)} \cdot \mathrm{N(H_2)} + K \ , \tag{6.1}$$

where $\mathrm{X(NH_3)}$ is the ammonia abundance and K is a negative constant that concerns the fact that dust detection with Herschel can reach lower densities than ammonia, since it traces more extended emission. A linear fit therefore gives provides the NH_3 fractional abundance and the lower limit in $\mathrm{N(H_2)}$ at which we start seeing ammonia, also known as *zero point column density.* Since relative uncertainties are usually higher for Herschel data (especially in the dense core, see Figure 6.3), and the fitting procedure requires uncertainties on the y-axis, we invert Eq. (6.1), using therefore:

$$\mathrm{N(H_2)} = m \cdot \mathrm{N(NH_3)} + \mathrm{N(H_2)}_0 \ , \tag{6.2}$$

where $m = 1/\mathrm{X(NH_3)}$ and $\mathrm{N(H_2)}_0$ is the minimum value of $\mathrm{N(H_2)}$ at which ammonia is detected.

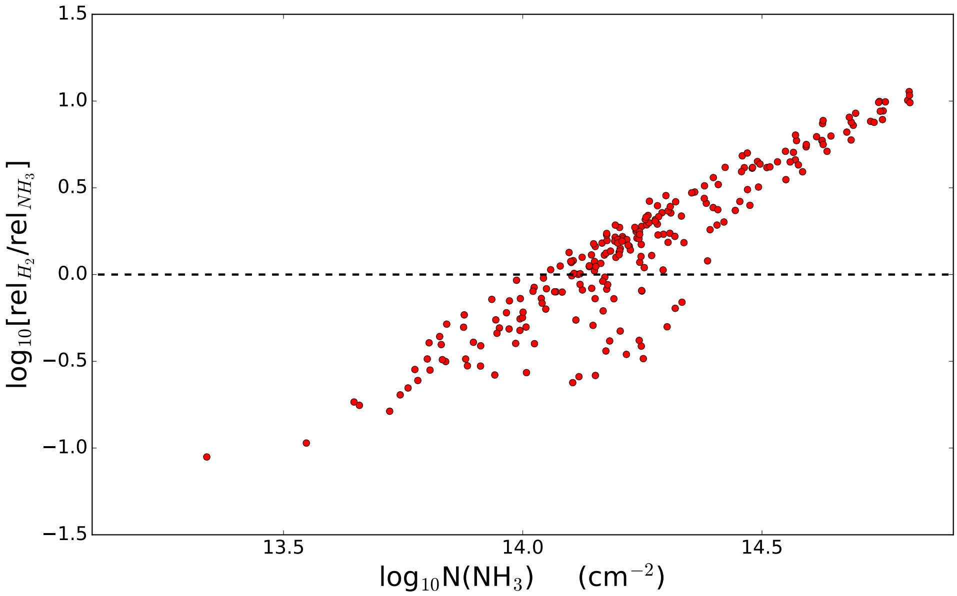

Figure 6.3: Scatter plot of the ratio between relative uncertainties on $\mathrm{N(NH_3)}$ and $\mathrm{N(H_2)}$ against ammonia column density. The dashed, black line marks where the ratio is equal to 1. Especially at high densities Herschel data are noisier.

Table 6.1 summarizes fit results. The best fit relations are plotted in Figure 6.4.

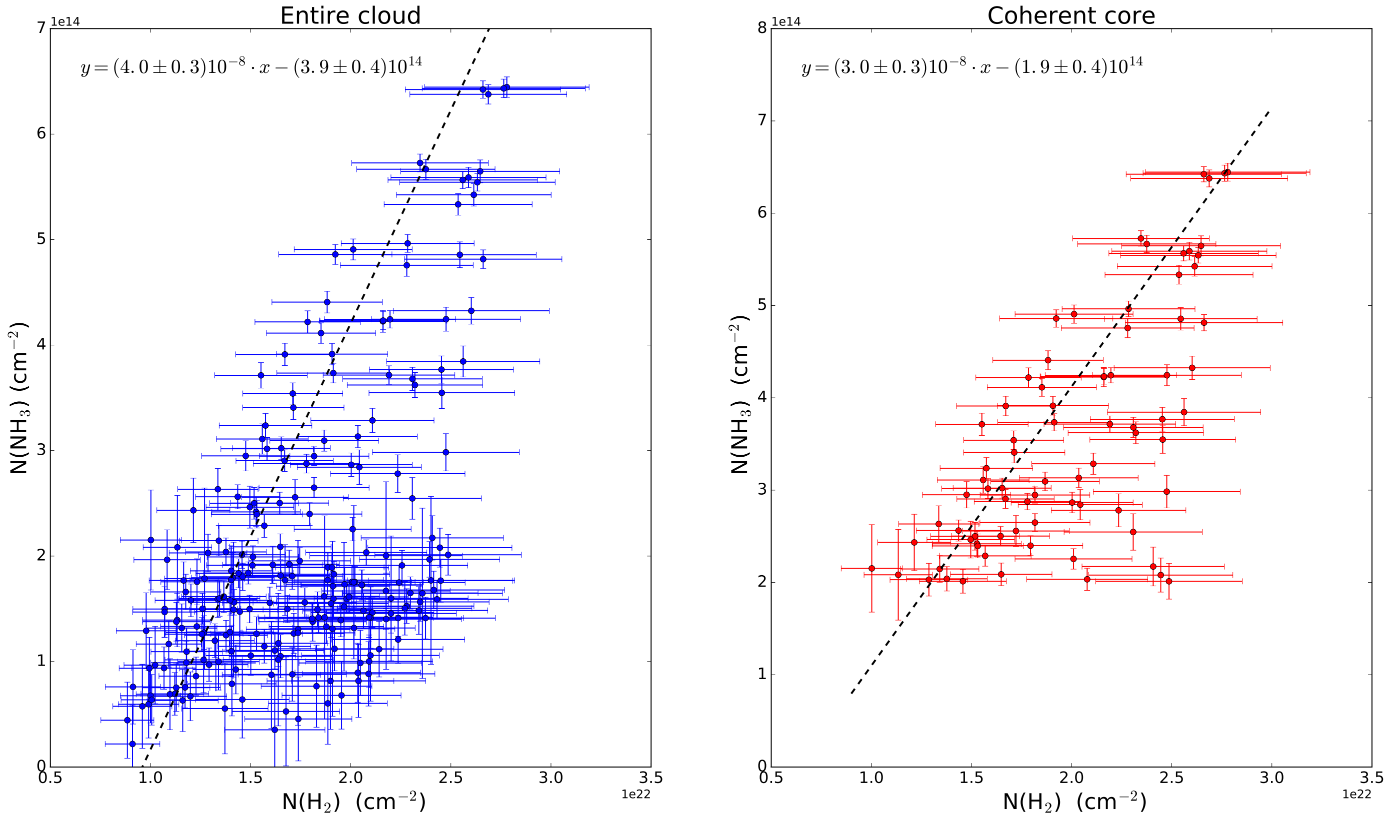

Figure 6.4: Same scatter plots as in Figure 6.2: in the left panel we show the data from the entire cloud, while in the right one from the coherent core only. Note that the scale is linear. In both panels we show the best fit regression (dash black line) and its equation.

Table 6.1: Summary of the best-fit parameters obtained on column densities data.

m (10^7)	$N(H_2)_0$ ($10^{21}cm^{-2}$)	r[1]	$X(NH_3)$ (10^{-8})	A_V[2]
		Entire cloud		
2.4 ± 0.2	9.6 ± 0.4	0.580	4.0 ± 0.3	10.2 ± 0.4
		Coherent core only		
3.3 ± 0.3	6.4 ± 1.0	0.702	3.0 ± 0.3	6.8 ± 1.1

[1] Linear correlation coefficient.

[2] Extinction calculated from $N(H_2)_0$, using the relation $N(H_2)= 0.94\,10^{21} A_V$ (Bohlin et al., 1978).

The correlation coefficient r is higher for the fit on the coherent core only, indicating that this linear relation holds better for the densest part of the cloud, where uncertainties are smaller. It is important to notice that the values obtained for $N(H_2)_0$ and $X(NH_3)$ are averages on the field in which they are computed.

The parameters obtained thorough the fitting procedure allow us to calculate a map for the ammonia fractional abundance in Barnard 59, which due to Eq. (6.1) is not simply the ratio between $N(NH_3)$ and $N(H_2)$ pixel by pixel, but is:

$$X(NH_3) = \frac{N(NH_3)}{N(H_2) - N(H_2)_0} \, . \tag{6.3}$$

We use the value for $N(H_2)_0$ obtained from the coherent core only, since data are more reliable due to the higher density and the linear relation seems stronger according to the correlation coefficient.

Figure6.5 shows the abundance map. The abundance ranges from the minimum value $X(NH_3)= 2.9\,10^{-9}$ to the maximum of $X(NH_3)= 5.9\,10^{-8}$, with an average of about $1.7\,10^{-8}$. These values are quite in agreement with other star forming regions, such as Ophiucus (Friesen et al., 2009) and Perseus (Foster et al., 2009). Highest values are found in the region of the coherent core and in the north-east part of the cloud. There is not a clear correlation with the YSOs positions. However, around B11, as expected from the depletion of ammonia previously discussed, the fractional abundance is lower than in the coherent core, even though it is still higher than in the surroundings from this source.

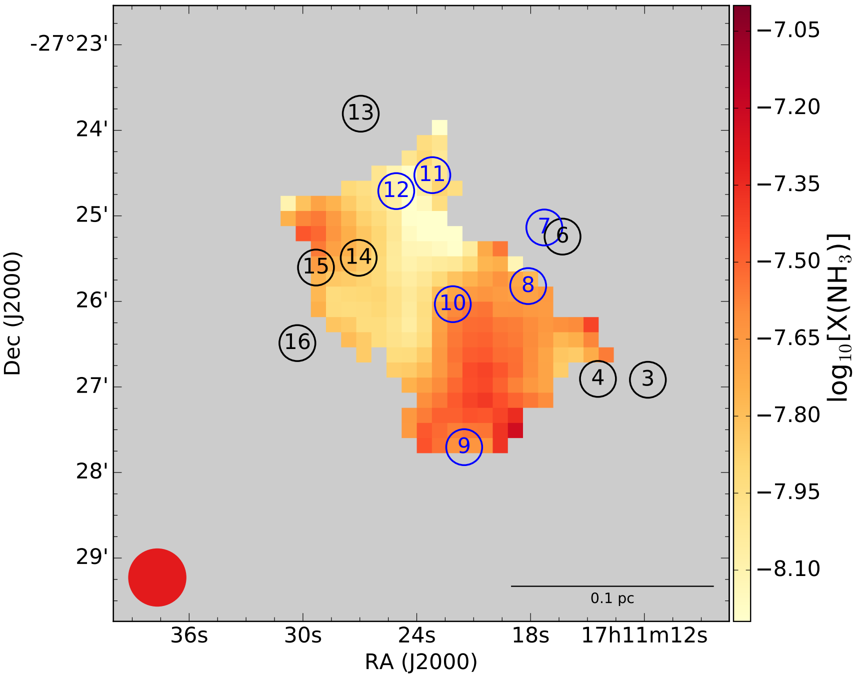

Figure 6.5: Ammonia fractional abundance map obtained using the correct equation (6.3).

6.2 Dust and Gas temperature

We now compare the dust temperature map obtained from Herschel data and the kinetic one from ammonia analysis: the scatter plot is shown in Figure 6.6. It is interesting that in both panels all the points are below the 1:1 line (dashed curve). This is due to the fact that temperatures obtained fitting the gray-body emission from dust grains are usually overestimated, since Herschel is sensitive to a more extended emission coming from the "warm" gas that surrounds cold cores, where NH_3 is not present or less abundant than toward the cold regions: the temperatures obtained from the fit are an average along the line of sight and as a consequence they result higher.

The left panel, containing data from the entire cloud, shows a positive correlation between the two variables: the correlation coefficient is $r = 0.670$. At the highest temperatures, though, some points move away from this trend. These data, marked in green, comes from source B11. This confirms that B11 is affecting the gas with its activity. Data from the right panel, where $\log_{10}(N(NH_3)) > 14.3$, show that the coherent core is essentially isothermal: for these points, in fact, the correlation coefficient is low ($r = 0.124$).

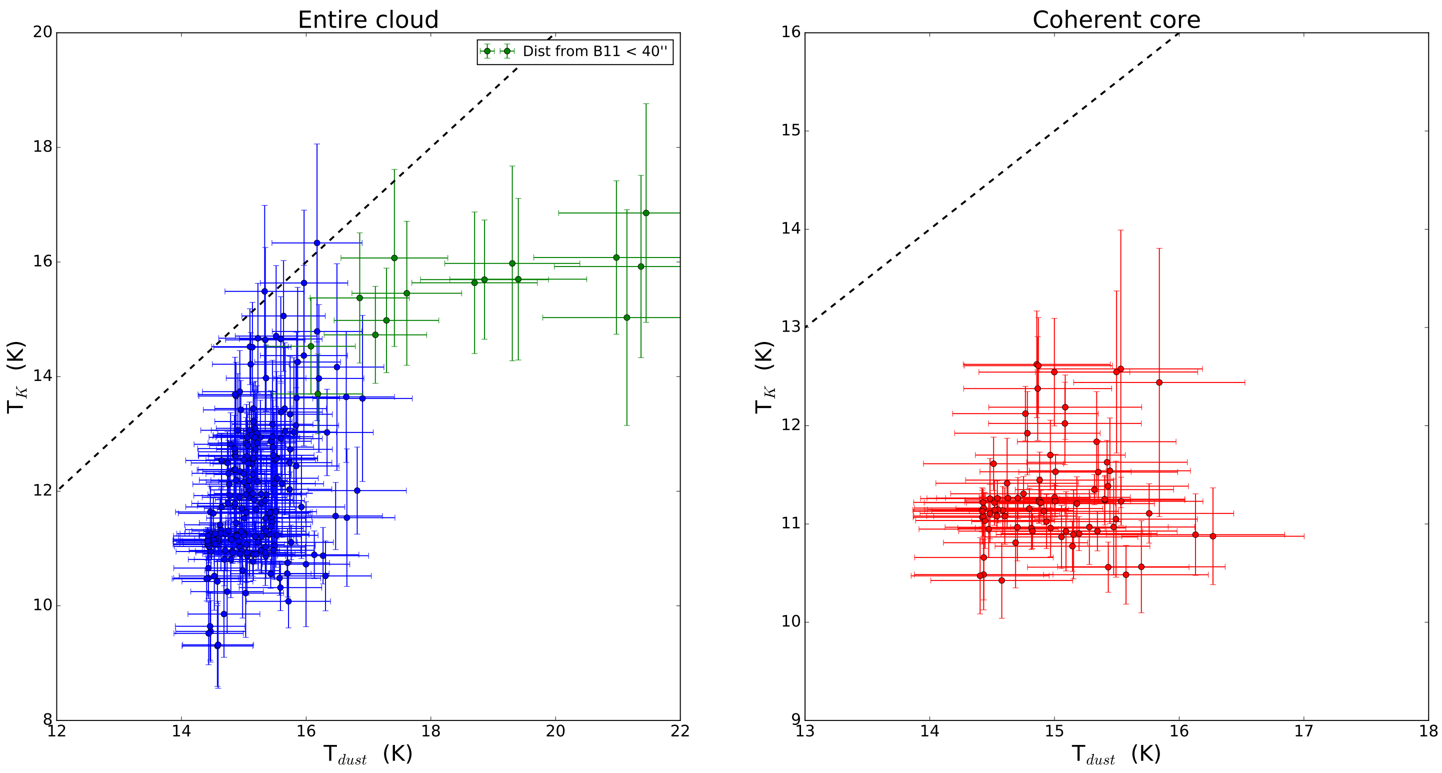

Figure 6.6: Scatter plots of kinetic temperature versus dust temperature for the entire cloud (left panel) and in the coherent core only (right panel). In the former, green points are closer than 40" to the source B11. The dashed curve represent the 1:1 line.

The data from the entire cloud shows another interesting behaviour: as temperature gets higher, the offset between T_K and T_{dust} tends to decrease. We think that the physical explanation is to be found in the gas heating source. In fact, the just mentioned trend of T_{dust} to overestimate T_K is true in case of an external heating due for example to the interstellar radiation field. In this case, since Herschel traces a larger scale than ammonia, it is sensitive to the warm envelope that surrounds the core, heated from outside in. On the other hand, if there is an internal source of heating (such as thermal heating from the protostar in B11 or mechanical heating from the protostellar outflows) also the internal part of the cloud is warmer, and ammonia is able to trace it: therefore T_K gets closer to T_{dust}. In Figure 6.7 we show the dust temperature maps and the young stellar objects positions. It is interesting to notice that all the hot condensations described is Sec. 4.4 correspond, within a beam size, to one or more young sources: we report in Table 6.2 the relative distances. B11 corresponds to the hottest of these structures. For the remaining ones, following the numeration of Table 4.4, we have: B06/B07

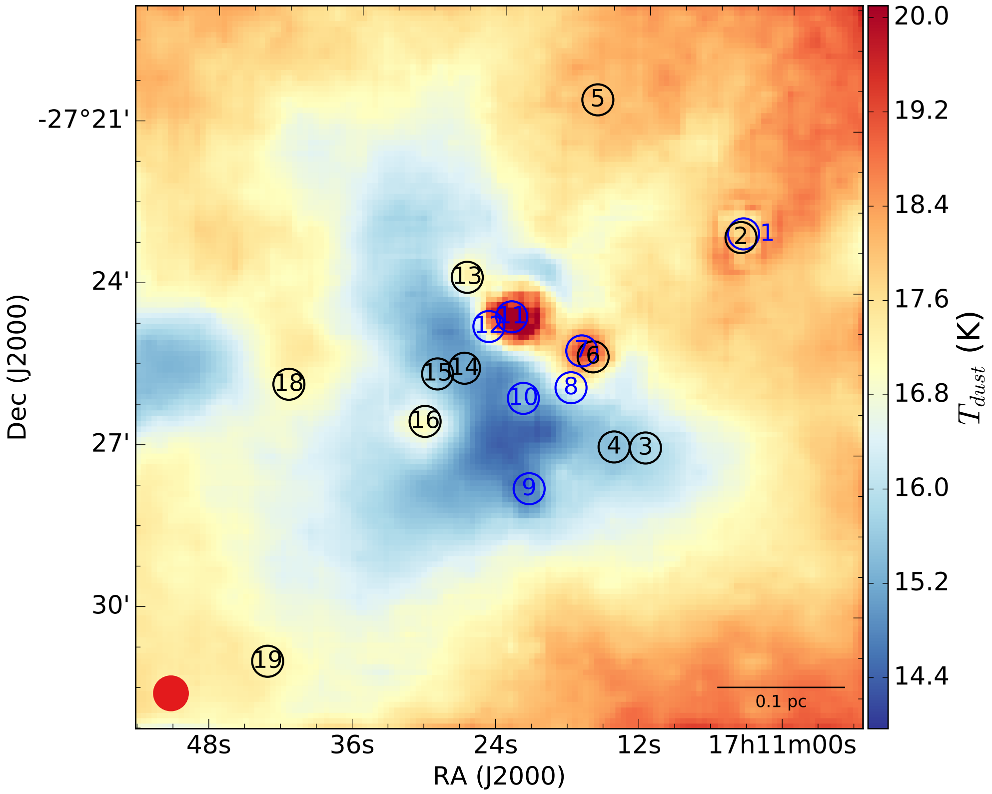

Figure 6.7: Ammonia fractional abundance map obtained using the correct equation (6.3).

corresponding to clump n.2 (our resolution does not allow us to disentangle these two sources), B13 to clump n.3 and B16 for the n.4. Interestingly, these YSOs differ for their evolutionary stage. Unfortunately, ammonia emission covers only B11 among these sources. Performing a deeper observation would allow us to extend our kinetic temperature map to the other objects, in order to investigate whether the temperature increase is detected also by molecular emission.

Table 6.2: Angular distances between the hot condensations temperature peaks and YSOs.

Condensation N.[1]	YSO	Distance
1	B11	15.9 arcsec
2	B06	13.7 arcsec
2	B07	5.05 arcsec
3	B13	5.00 arcsec
4	B16	2.41 arcsec

[1] Hot condensation number according to Figure 4.6.

Chapter 7

Conclusions

In this work we have studied a region of low-mass star formation in the Pipe nebula, a molecular cloud located in the direction of the galactic center. The Pipe hosts almost 200 of dense cores, but only one is interested by star formation activity: Barnard 59. Using molecular spectroscopy, we have investigated the kinematic of the latter and obtained crucial information on its physical properties.

The technical approach we have used consists in fitting the hyperfine emission of the ammonia transitions using a standard analytical method, but with an innovative implementation contained in the python library PYSPECKIT. We have also used Herschel data in order to observe dust continuum emission from the source. These two different data sets allowed us to study the core properties, and especially the influence of the young protocluster known to be hosted in the source. In particular, we have investigated how the protostellar feedback affects the temperature, the velocity dispersion and the dynamical state of the core.

I will now summarize the main conclusions:

- The ammonia data of B59 were collected as a part of the GBT Ammonia Survey, a large legacy survey led at the Green Bank Telescope. The observations of the (1,1) and (2,2) inversion transitions at the rest frequency of $\nu_{11} = 23694.4955\,\mathrm{MHz}$ and $\nu_{22} = 23722.6336\,\mathrm{MHz}$ respectively were carried out with the VEGAS spectrometer combined with the KFPA frontend. The resulting spectral resolution is $5.72\,\mathrm{KHz}$ ($0.07\,\mathrm{km\,s^{-1}}$), while the angular resolution is 31.8 arcsec, which at the Pipe distance corresponds to a spatial resolution of 0.02 pc. The noise level of the obtained map is $\approx 0.15\,K$, close to the target $100\,\mathrm{m}K$ level of the survey;

- We detected both (1,1) and (2,2) inversion transition lines of ammonia. As expected, the first one is brighter and its emission more extended than the second one, since the (2,2) state is usually less populated than the (1,1) in cold gas. The peak brightness temperature T_{MB} is $5.29\,K$ for the (1,1) and $1.66\,K$ for the (2,2) line;

- Fitting the two transitions pixel by pixel we obtain the molecular column density, kinetic temperature, excitation temperature, velocity dispersion and centroid velocity map;

- The (2,2) line is considerably weaker than the (1,1) and, for this reason, the molecular column density and kinetic temperature could not be properly determined across the whole NH_3 (1,1) map. In order to increase the (2,2) signal-to-noise ratio, we have tested two methods: the Gaussian smoothing of the data cubes and the Voronoi Binning. The latter performs an adaptive binning, keeping the angular resolution unchanged where the SNR is higher. However, this method is optimized for larger sources with an extended faint emission. Since the NH_3 emission in B59 is more compact than in cloud complexes, the binning was constrained to a very small portion of the core. In addition, averaging spectra as complex as ammonia ones (due to its hyperfine structure) can lead to unrealistic linewidths, if gradients in the local standard of rest velocity are present. We have therefore opted for smoothing the maps to 40 arcsec, which is about 25% lower than the native resolution;

- Our resulting parameter maps show the presence of a dense and cold core, as visible in Figure 3.9. This structure is predominantly quiescent: the velocity dispersion values are low, around $0.17\,\mathrm{km\,s^{-1}}$. We refer to it as the coherent core. At the northern part of the cloud, however, temperatures are higher ($T_K \gtrsim 18\,K$) and σ_V increases up to $0.40\,\mathrm{km\,s^{-1}}$. It is interesting to notice that the excitation temperature values are systematically lower than kinetic temperature ones, marking that in this source ammonia is sub-thermally excited: the number density must be lower than NH_3 critical density;

- We have analysed Herschel data by fitting the three photometric bands with a gray-body emission model. This method allows to compute the H_2 column density and dust temperature maps. Similarly to the NH_3 data, Barnard 59 reveals a cold, dense core, with a peak column density of $N(H_2) = (3.0 \pm 1.6)\,10^{22}\,\mathrm{cm^{-2}}$ and a minimum temperature of $T_{dust} = (14.3 \pm 0.5)\,K$. The dust temperature shows peaks of up to $\approx 22\,K$;

- There are about 20 young stellar objects in the source. Our data allow us to study their influence on the core. YSOs especially in their early stages launch outflows that, in turn, inject turbulence in the surrounding medium. As a consequence, the gas velocity dispersion tends to increase. Furthermore, from the kinetic temperature we are able to predict if the velocity dispersion is due purely to thermal motions of there is an extra component provided by turbulence. From these we are able to compare the non-thermal gas motions with the sonic speed in the observed gas. Most of the core, and in particular the densest and coldest parts, present subsonic gas motions. The transition to supersonic motions is sharp, and gas motions become more turbulent closer to the sources B11 and B12, the former being a known outflow-driving source. We can therefore conclude that these sources are affecting the surrounding gas, heating and injecting turbulence in it. Despite the protostellar feedback, the core seems to be dynamically stable. The virial parameter we compute is $\alpha_{vir} = 0.56 \pm 0.24$, which means that Barnard 59 is gravitationally bound and it could form other starts;

- The results derived from NH_3 spectroscopy and Herschel data allow us to make a comparison between gas and dust properties. The molecular densities $N(NH_3)$ and $N(H_2)$ (this one scaled from the dust column density) appear in a positive correlation. We derived the ammonia fractional abundance in the source. We find a mean value of $X(NH_3) = 1.7\,10^{-8}$, in agreement with previous estimations for other star forming regions. The kinetic temperature T_K and the dust temperature T_{dust} show a positive correlation as well, but the former is systematically lower than the latter. Herschel traces the extended dust emission from the clouds. It is therefore more sensitive to the external radiation field (especially UV radiation) than ammonia. The molecular emission is instead more sensitive to the stellar feedback. It is interesting to notice that the offset between the two variables tends to decrease as gas temperature itself increases close to the YSO locations, as one can see in Figure 7.1. This means that the YSOs are responsible for the internal heating of the cloud and that ammonia is a good tracer of this temperature increase.

In conclusion, Barnard 59 is a dense and cold core that harbours a young protocluster formed by objects at different evolutionary stages. Some of them, especially the youngest and less evolved ones such as B11, are affecting the surrounding medium with protostellar feedback, most probably thorough the outflows they are driving. Their activity, however, is not disturbing the overall dynamical state of the source, which still appears to be gravitationally bound. On the other hand, at the current resolution we do not see signs of collapse or contraction such as fragmentation. Since this was also proposed by previous authors, our interpretation is that the core is unlikely to form new stars. The older YSOs are not affecting the kinematics and thermal structure of B59, suggesting that they are not associated with the cold core.

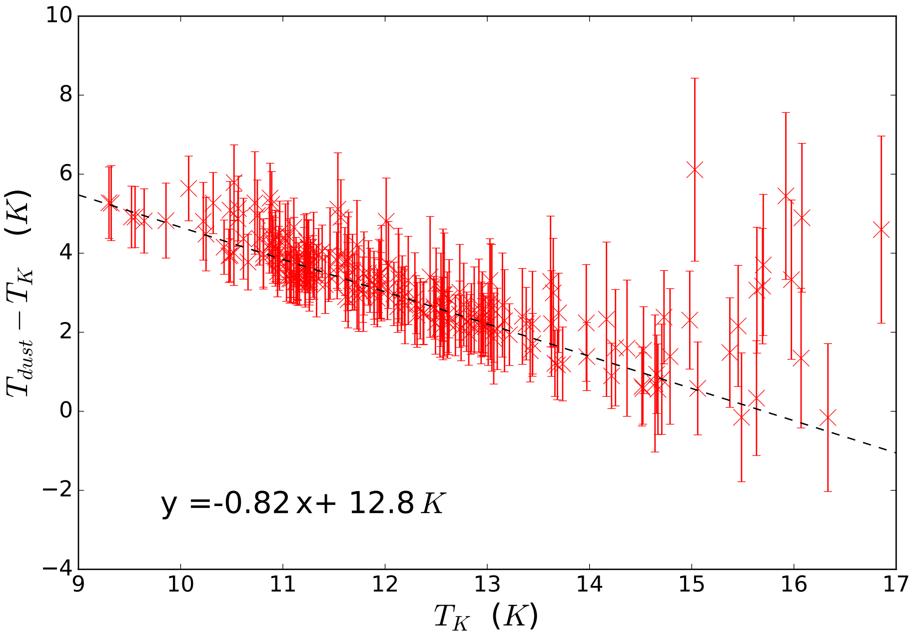

Figure 7.1: The difference between dust and kinetic temperature as a function of the latter. The dashed line is the best fit linear relation found.

7.1 Future perspectives

The analysis performed so far helps us to better understand the physical, dynamical and kinematic conditions of our source. In the future, we would like to obtain deeper observations in order to extend the region of ammonia detection towards the edge of B59. On one hand, we would be able to study the larger scale ammonia emission, extending our study on the subsonic and supersonic nature of gas motions. In fact, we already see a sharp transition to the quiescent and subsonic core, but only due to protostellar feedback. We would like to understand if the core is formed by turbulent dissipation by investigating the large scale kinematics of the gas surrounding the core. Furthermore, maps with a larger coverage would comprise other YSOs that for the moment we have excluded from our analysis, increasing our comprehension of protostellar feedback effects.

Another interesting project is to investigate the magnetic field in the core. It is known that magnetic fields play an important role in regulating core collapse. There are studies of the magnetic field morphology across the entire Pipe, but on a much larger scale. New infrared polarimetric data would allow us to determine the strength of the magnetic field and its direction. Our team has granted SOFIA polarimetric observations at 1.4 THz (250 μm) toward B59. At these bands, we trace the polarized thermal emission from dust at $T \approx 10 \sim 30\,K$. We plan to combine these data with optical and near-infrared polarimetric data in order to obtain a multi-scale view of the magnetic field in B59 and determine its importance on the core dynamics. Finally, we will compare the B-field morphology with the velocity field obtained from the NH_3 data and show if the gas motions are affected by the magnetic field.

Finally, another interesting facet concerns the technical aspects of how our analysis has been performed. The Voronoi binning technique seems to have great potential also in the field of molecular spectroscopy. In order to examine this point, we need to run further tests in order to improve the method. This is the first time that this technique is applied to local star formation. This requires a more significant statistics. We should compare more extended and deeper maps of B59 with the binned ones, in order to verify whether the Voronoi method returns correct values for the parameters. Furthermore, performing the same analysis on other sources will further improve the applicability of this technique in the astrochemistry field.

Appendix A

YSOs scatter plots

We present here the scatter plots of σ_V and σ_{NTh}/C_S versus T_{peak} for the sources not shown in Ch. 5.

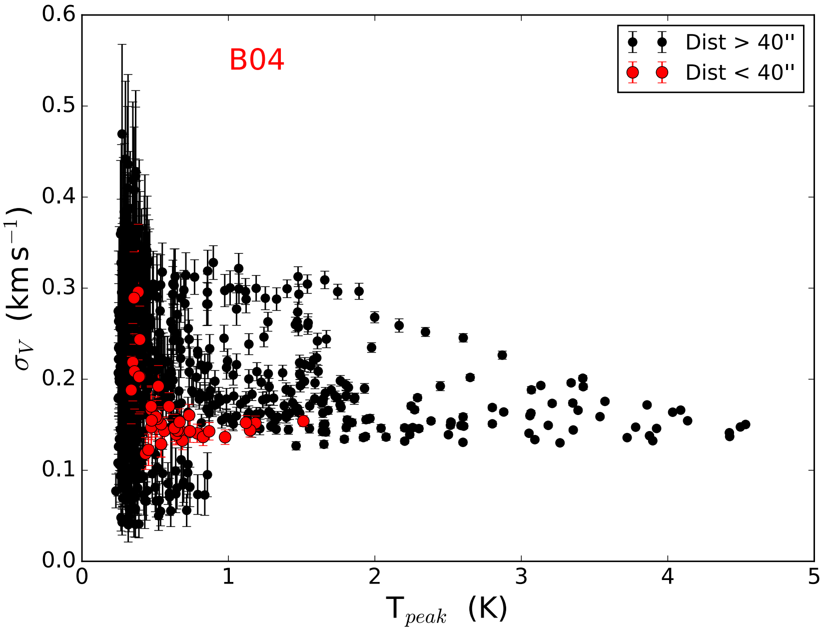

Figure A.1: σ_V versus T_{peak} for B04 (Class II). Red points are closer than 40″ to the source.

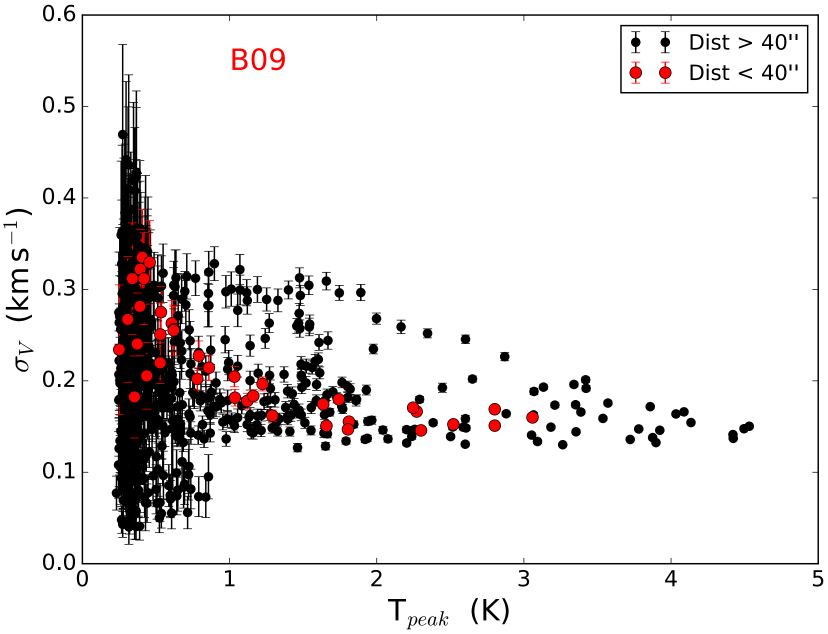

Figure A.2: σ_V versus T_{peak} for B09 (Class I/II). Red points are closer than 40″ to the source.

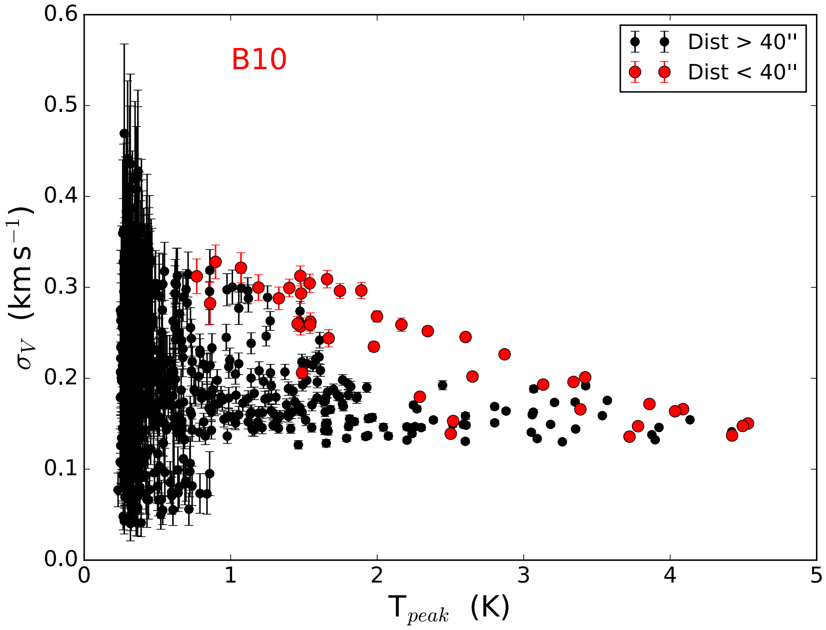

Figure A.3: σ_V versus T_{peak} for B10 (Class I). Red points are closer than 40″ to the source.

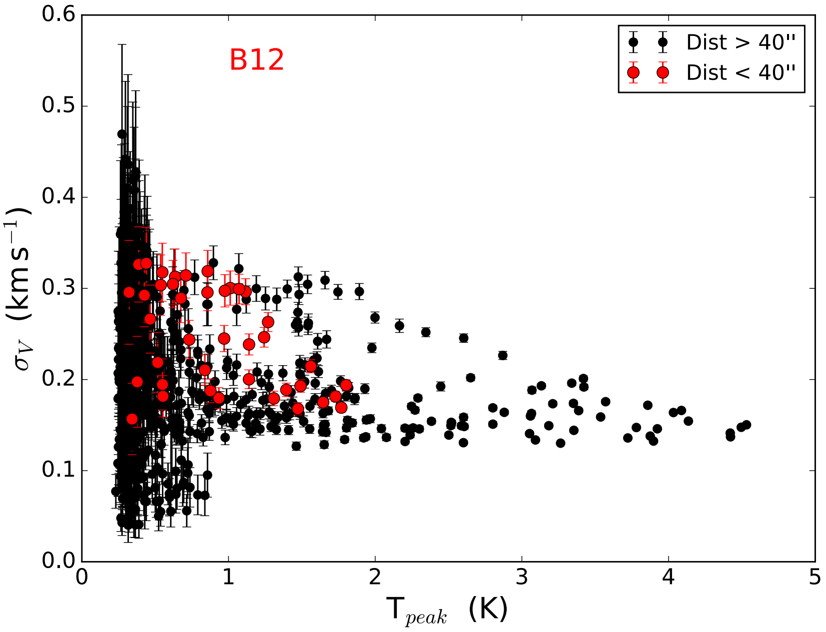

Figure A.4: σ_V versus T_{peak} for B12 (Class I/II). Red points are closer than 40″ to the source.

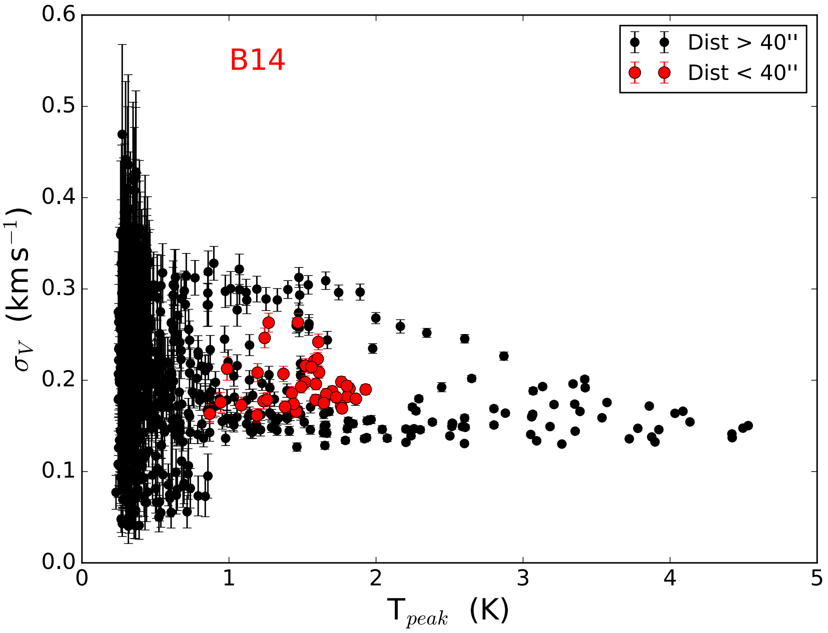

Figure A.5: σ_V versus T_{peak} for B14 (Class II). Red points are closer than 40″ to the source.

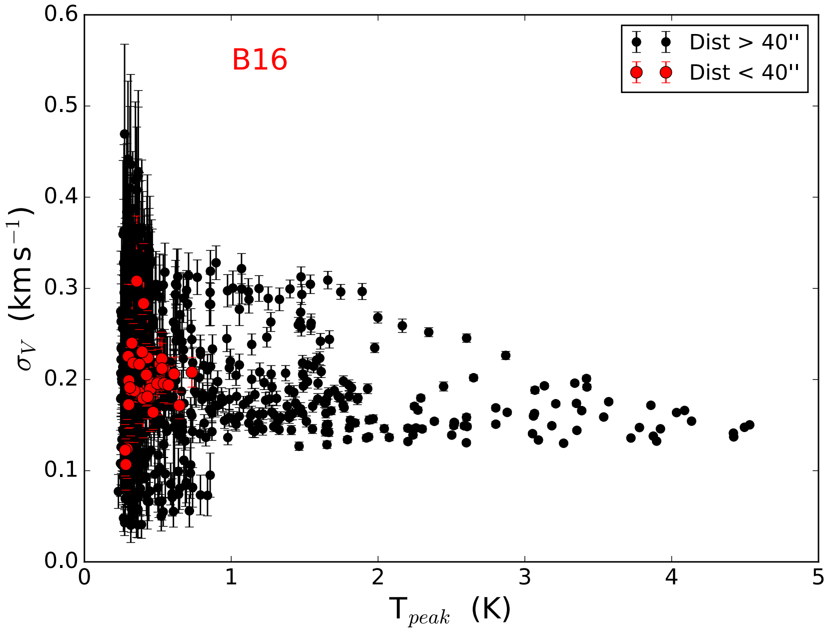

Figure A.6: σ_V versus T_{peak} for B16 (Class II). Red points are closer than 40″ to the source.

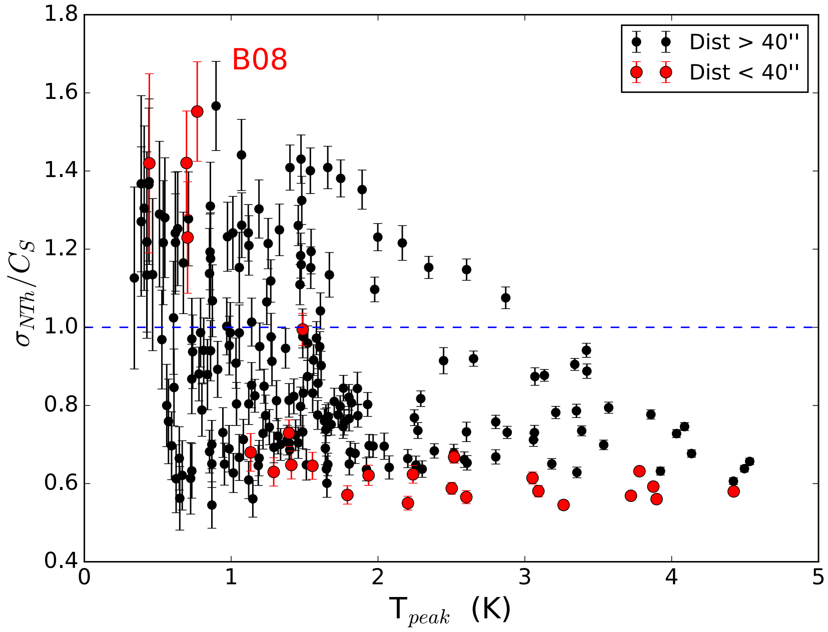

Figure A.7: σ_{NTh}/C_S versus T_{peak} for B08 (Class I). Red points are closer than 40″ to the source. Dashed blue lines marks transition between sub- and supersonic motions.

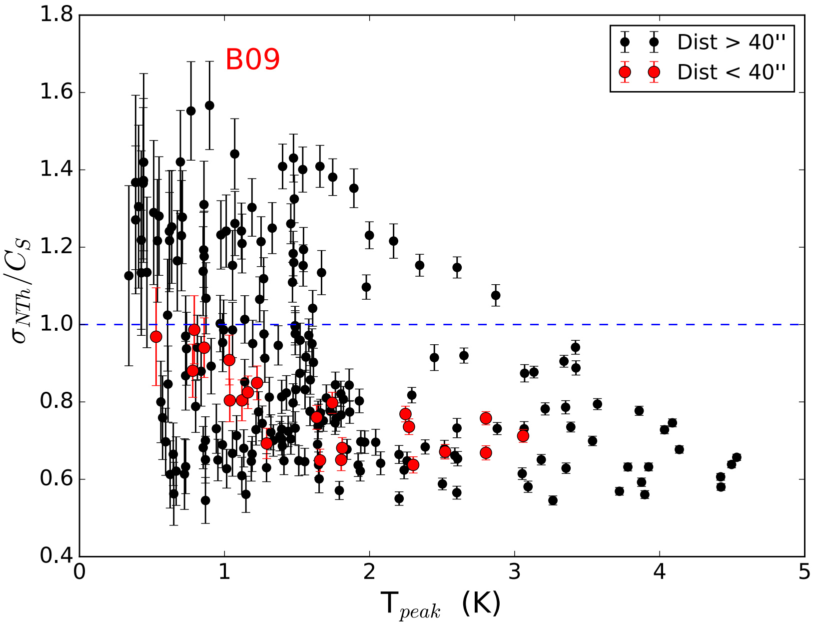

Figure A.8: σ_{NTh}/C_S versus T_{peak} for B09 (Class I/II). Red points are closer than 40″ to the source. Dashed blue lines marks transition between sub- and supersonic motions.

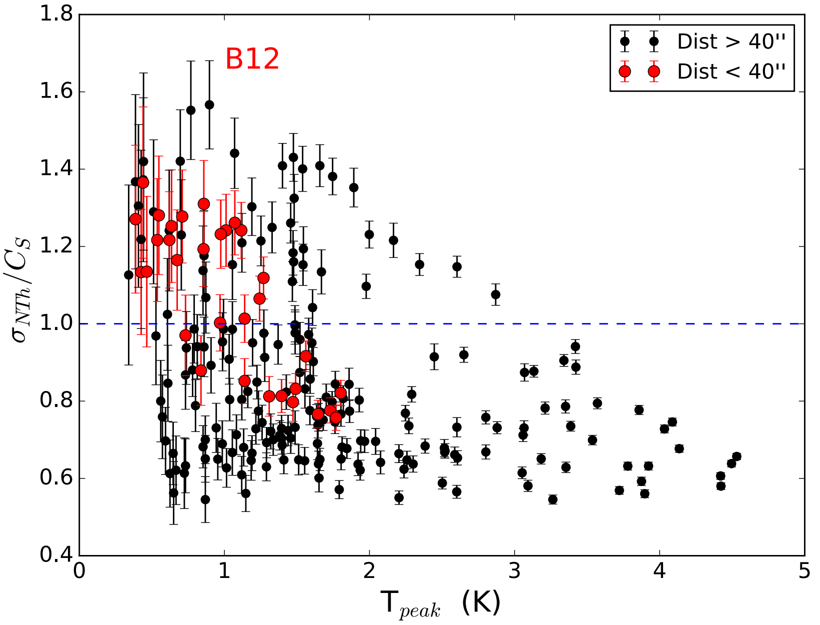

Figure A.9: σ_{NTh}/C_S versus T_{peak} for B12 (Class I/II). Red points are closer than 40″ to the source. Dashed blue lines marks transition between sub- and supersonic motions.

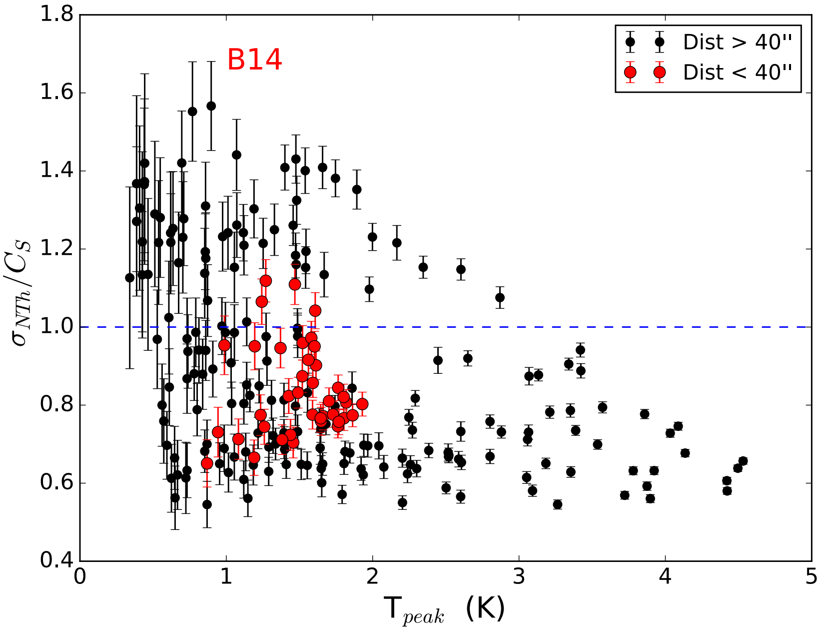

Figure A.10: σ_{NTh}/C_S versus T_{peak} for B14 (Class II). Red points are closer than 40″ to the source. Dashed blue lines marks transition between sub- and supersonic motions.

Bibliography

Alves, F. O., & Franco, G. A. P. 2007, A&A, 470, 597

Alves, F. O., Franco, G. A. P., & Girart, J. M. 2008, A&A, 486, L13

Alves, J., Lombardi, M., & Lada, C. J. 2007, A&A, 462, L17

Andre, P., Ward-Thompson, D., & Barsony, M. 2000, Protostars and Planets IV, 59

Beckwith, S. V. W., Sargent, A. I., Chini, R. S., & Guesten, R. 1990, AJ, 99, 924

Bertoldi, F., & McKee, C. F. 1992, ApJ, 395, 140

Bohlin, R. C., Savage, B. D., & Drake, J. F. 1978, ApJ, 224, 132

Brooke, T. Y., Huard, T. L., Bourke, T. L., et al. 2007, ApJ, 655, 364

Cappellari, M., & Copin, Y. 2003, MNRAS, 342, 345

Caselli, P., Benson, P. J., Myers, P. C., & Tafalla, M. 2002, ApJ, 572, 238

Caselli, P., & Ceccarelli, C. 2012, A&A Rev., 20, 56

Charnley, S. B., & Rodgers, S. D. 2002, ApJ, 569, L133

Covey, K. R., Lada, C. J., Román-Zúñiga, C., et al. 2010, ApJ, 722, 971

de Zeeuw, P. T., Hoogerwerf, R., de Bruijne, J. H. J., Brown, A. G. A., & Blaauw, A. 1999, AJ, 117, 354

Diehl, S., & Statler, T. S. 2006, MNRAS, 368, 497

Duarte-Cabral, A., Chrysostomou, A., Peretto, N., et al. 2012, A&A, 543, A140

Faure, A., Hily-Blant, P., Le Gal, R., Rist, C., & Pineau des Forêts, G. 2013, ApJ, 770, L2

Forbrich, J., Lada, C. J., Muench, A. A., Alves, J., & Lombardi, M. 2009, ApJ, 704, 292

Foster, J. B., Rosolowsky, E. W., Kauffmann, J., et al. 2009, ApJ, 696, 298

Franco, G. A. P., Alves, F. O., & Girart, J. M. 2010, ApJ, 723, 146

Frau, P., Girart, J. M., & Beltrán, M. T. 2012a, A&A, 537, L9

Frau, P., Girart, J. M., Beltrán, M. T., et al. 2010, ApJ, 723, 1665

—. 2012b, ApJ, 759, 3

Friesen, R. K., Di Francesco, J., Shirley, Y. L., & Myers, P. C. 2009, ApJ, 697, 1457

GBT Scientific Staff. 2015, Observing with the Green Bank Telescope, `https://science.nrao.edu/facilities/gbt/observing/GBTog.pdf`, online; accessed in September 2016.

GBT Support Staff. 2016, Green Bank Observatory Proposer's Guide for the Green Bank Telescope, `https://science.nrao.edu/facilities/gbt/proposing/GBTpg.pdf`, online; accessed in September 2016.

Gersho, A. 1979, IEEE transaction on information theory, 25, 373

Goodman, A. A., Barranco, J. A., Wilner, D. J., & Heyer, M. H. 1998, ApJ, 504, 223

Goodman, A. A., Pineda, J. E., & Schnee, S. L. 2009, ApJ, 692, 91

Hara, C., Shimajiri, Y., Tsukagoshi, T., et al. 2013, ApJ, 771, 128

Hardegree-Ullman, E., Harju, J., Juvela, M., et al. 2013, ApJ, 763, 45

Hasegawa, T. I., Herbst, E., & Leung, C. M. 1992, ApJS, 82, 167

Hildebrand, R. H. 1983, QJRAS, 24, 267

Ho, P. T. P., & Townes, C. H. 1983, ARA&A, 21, 239

Lada, C. J., Muench, A. A., Rathborne, J., Alves, J. F., & Lombardi, M. 2008, ApJ, 672, 410

Li, A. 2008, ArXiv e-prints, arXiv:0808.4117

Lombardi, M., Alves, J., & Lada, C. J. 2006, A&A, 454, 781

Mangum, J. G., Emerson, D. T., & Greisen, E. W. 2007, A&A, 474, 679

Mangum, J. G., & Shirley, Y. L. 2015, PASP, 127, 266

McMullin, J. P., Waters, B., Schiebel, D., Young, W., & Golap, K. 2007, in Astronomical Society of the Pacific Conference Series, Vol. 376, Astronomical Data Analysis Software and Systems XVI, ed. R. A. Shaw, F. Hill, & D. J. Bell, 127

Mezger, P. G., Zylka, R., & Wink, J. E. 1990, A&A, 228, 95

Muench, A. A., Lada, C. J., Rathborne, J. M., Alves, J. F., & Lombardi, M. 2007, ApJ, 671, 1820

Onishi, T., Kawamura, A., Abe, R., et al. 1999, PASJ, 51, 871

Ossenkopf, V., & Henning, T. 1994, A&A, 291, 943

Peretto, N., André, P., Könyves, V., et al. 2012, A&A, 541, A63

Pickett, H. M., Poynter, R. L., Cohen, E. A., et al. 1998, J. Quant. Spec. Radiat. Transf., 60, 883

Pineda, J. E., Caselli, P., & Goodman, A. A. 2008, ApJ, 679, 481

Pineda, J. E., Goodman, A. A., Arce, H. G., et al. 2010, ApJ, 712, L116

Rathborne, J. M., Lada, C. J., Muench, A. A., et al. 2009, ApJ, 699, 742

Riaz, B., Martín, E. L., Bouy, H., & Tata, R. 2009, ApJ, 700, 1541

Robitaille, T. P., Whitney, B. A., Indebetouw, R., Wood, K., & Denzmore, P. 2006, ApJS, 167, 256

Rodgers, S. D., & Charnley, S. B. 2008, ApJ, 689, 1448

Román-Zúñiga, C. G., Frau, P., Girart, J. M., & Alves, J. F. 2012, ApJ, 747, 149

Román-Zúñiga, C. G., Lada, C. J., & Alves, J. F. 2009, ApJ, 704, 183

Scott, G. B. I., Freeman, C. G., & McEwan, M. J. 1997, MNRAS, 290, 636

Stahler, S. W., & Palla, F. 2005, The Formation of Stars, 865

Swift, J. J., Welch, W. J., & Di Francesco, J. 2005, ApJ, 620, 823

Taylor, S. D., Morata, O., & Williams, D. A. 1998, A&A, 336, 309

Townes, C. H. 2006, in Astronomical Society of the Pacific Conference Series, Vol. 356, Revealing the Molecular Universe: One Antenna is Never Enough, ed. D. C. Backer, J. M. Moran, & J. L. Turner, 81

Ungerechts, H., Winnewisser, G., & Walmsley, C. M. 1986, A&A, 157, 207

Valtchanov, I. 2015, The Spectral and Photometric Imaging Receiver (SPIRE) Handbook V, `http://herschel.esac.esa.int/Docs/SPIRE/html/spire_om.html`, online; accessed in Maj 2016.

Walker, C. K., Adams, F. C., & Lada, C. J. 1990, ApJ, 349, 515

Walmsley, C. M., & Ungerechts, H. 1983, A&A, 122, 164

Wilson, T. L., Rohlfs, K., & Hüttemeister, S. 2009, Tools of Radio Astronomy, 5th edn. (Heidelberg: Springer)

Young, C. H., Jørgensen, J. K., Shirley, Y. L., et al. 2004, ApJS, 154, 396

Acknowledgments

At the end of this work I would like to thank all my supervisors and co-supervisors: Prof. Andrea Cimatti, who has helped me in many ways since my first master year; Prof. Paola Caselli, who has carefully supervised my work at the Max Planck Institute. Finally, I would like to thank Dr. Felipe Alves, whose office door has always been open for me through all these months. Thank you for all the advice you patiently gave me and for everything you taught me.

I also would like to thank all the members of the GAS survey that kindly provided me data and methods fundamental for this thesis. In particular I would like to mention Dr. Jaime Pineda, who has always answered each of my questions.

Finally, I am glad to thank Dr. Jorma Harju for being so patient and kind in helping me with my first steps in Herschel data handling, and for sharing with me his code.

Time for taking stock

This work somehow marks the end of a journey that I can definitely describe as one of the most wonderful of my life. It started more than five years ago, and it has been full of great and unforgettable moments, but also of dark and difficult ones, and I am definitely proud of myself seeing that I've been able to get through both. I may sound immodest, but I don't really care: I gave so much and struggled pretty hard to reach this point, and I am aware of it. Nevertheless, something else has to be said. When I enrolled at the university, naive and a bit impudent, I proudly thought that I could do all by myself. During these five and long years I (luckily) realized that I couldn't be more wrong and I (even more luckily) found many people that helped me, people without whom it would have been definitely more difficult and maybe impossible to reach my goals. In conclusion, today I am certainly proud of myself, but I'd also like to say many thanks.

First of all, I want to thank my family that has supported me not just in these last years but since my very first steps in this world: my mum, who taught me the worth of discipline and hard work; my dad, who once told me that "everything is worth being known"; my aunt zia Lele and my granny nonna Anna, my biggest fans. I also would like to thank my friends-for-a-lifetime Paola and Francesca: Meredith had her person, but I am so lucky that I've been given two.

Thanks to my "physics gang", who has been my second family since I moved in Bologna. In particular, I'd like to mention Laura, for all the laughing, the dancing and the crying that we have had since we met, and the other girls Azzurra and Ilaria; Enrico that has always had a special place in my heart; all my schoolmates that shared with me lessons, exams, hours in the study room and hours in the corridor outside the study room (Pietro, you know I'm talking of you). At the same time, I can't help remembering my master-mates that have made these last two years full of fun and good time, and in particular Giovanni, for all those times that you brought me back on earth when I was literally freaking out.

Thanks to my flatmates Flavia, Luisa and Michelangelo (and here we are all laughing), because you made my last months in Bologna incredible, and gave me the actual feeling of being home at the 5th floor of via Barozzi 6. Thanks to the entire Taekwon-Do group for making me part of a team I'll never forget, and in particular to my *maestro* Ricky and my friends Paola, Frank, Ema and Roby.

I have many thanks to say also to my friends and colleagues of the CAS group at MPE: when I arrived there I was really afraid and disoriented, but you all encouraged me and made me feel less "out of my place". Thanks to the entire Italian group: Michela for being almost a mum, Giulia for being such a good friend, Matteo and Alessandro for all the breaks, lunches, nights, discussions; Valerio and Luca for the irony and sarcasm (keeping saying that Munich is an horrible place actually made it easier to find some good in it) and Silvia for her neverending smile. Thanks to the student group: Domenico, Carolina, Anna and Ana. A special mention to Vlas: without you and your patience in answering the tons of questions I asked you I would have been really in trouble with my work. And thanks to Felipe, again, because you have been more than a supervisor: you made me grow as a person and a scientist.

Thanks to my boyfriend's family, Angela, Patrizio and Matilde, because you have always kept your door open for me during the months I spent far from the city and the people I love.

And finally, I'd like to thank Matteo. There are a million of reasons I could tell, but I will mention only a few: thanks for holding my hand when I needed support, thanks for pushing me when I was afraid to take a further step, and thanks for shaking me when I was totally wrong. You made my last year more fun, easier and deeper, and I will never forget it.

If this journey is coming to an end, a new one is starting: thanks to all of you for making me ready for it.